

GDSA Repository Systems Analysis FY19 Update

Fuel Cycle Research & Development

***Prepared for the
U.S. Department of Energy
Spent Fuel and Waste Science and
Technology Campaign***

***S. David Sevougian,
Emily R. Stein, Tara LaForce,
Frank V. Perry, Michael Nole,
and Kyung W. Chang***

***Sandia National Laboratories
September 27, 2019***

**M3SF-19SN010304052
SAND2019-11942R**



DISCLAIMER

This information was prepared as an account of work sponsored by an agency of the U.S. Government. Neither the U.S. Government nor any agency thereof, nor any of their employees, makes any warranty, expressed or implied, or assumes any legal liability or responsibility for the accuracy, completeness, or usefulness, of any information, apparatus, product, or process disclosed, or represents that its use would not infringe privately owned rights. References herein to any specific commercial product, process, or service by trade name, trade mark, manufacturer, or otherwise, does not necessarily constitute or imply its endorsement, recommendation, or favoring by the U.S. Government or any agency thereof. The views and opinions of authors expressed herein do not necessarily state or reflect those of the U.S. Government or any agency thereof.

DISCLAIMER

This is a technical report that does not take into account contractual limitations or obligations under the Standard Contract for Disposal of Spent Nuclear Fuel and/or High-Level Radioactive Waste (Standard Contract) (10 CFR Part 961). For example, under the provisions of the Standard Contract, spent nuclear fuel in multi-assembly canisters is not an acceptable waste form, absent a mutually agreed to contract amendment. To the extent discussions or recommendations in this report conflict with the provisions of the Standard Contract, the Standard Contract governs the obligations of the parties, and this report in no manner supersedes, overrides, or amends the Standard Contract. This report reflects technical work which could support future decision making by DOE. No inferences should be drawn from this report regarding future actions by DOE, which are limited both by the terms of the Standard Contract and a lack of Congressional appropriations for the Department to fulfill its obligations under the Nuclear Waste Policy Act including licensing and construction of a spent nuclear fuel repository.



Sandia National Laboratories is a multi-mission laboratory managed and operated by National Technology and Engineering Solutions of Sandia, LLC., a wholly owned subsidiary of Honeywell International, Inc., for the U.S. Department of Energy's National Nuclear Security Administration under contract DE-NA-0003525.

APPENDIX E NTRD DOCUMENT COVER SHEET¹

Name/Title of Deliverable/ Milestone/Revision No.	<i>GDSA Repository Systems Analysis FY19 Update, M3SF-19SN010304052</i>
Work Package Title & Number	<i>GDSA – Repository Systems Analysis – SNL, SF-19SN01030405</i>
Work Package WBS Number	<i>1.08.01.03.04</i>
Responsible Work Package Manager	<i>S. David Sevougian</i> 
	(Name/Signature)
Date Submitted	<i>September 27, 2019</i>

Quality Rigor Level for Deliverable/Milestone ²	<input type="checkbox"/> QRL-1 <input type="checkbox"/> Nuclear Data	<input type="checkbox"/> QRL-2	<input checked="" type="checkbox"/> QRL-3	<input type="checkbox"/> QRL-4 Lab QA Program ³
---	---	--------------------------------	---	---

This deliverable was prepared in accordance with Sandia National Laboratories
(Participant/National Laboratory Name)

QA program which meets the requirements of
 DOE Order 414.1 NQA-1 Other

This Deliverable was subjected to:

<input checked="" type="checkbox"/> Technical Review Technical Review (TR) Review Documentation Provided <input type="checkbox"/> Signed TR Report or, <input type="checkbox"/> Signed TR Concurrence Sheet or, <input checked="" type="checkbox"/> Signature of TR Reviewer(s) below	<input type="checkbox"/> Peer Review Peer Review (PR) Review Documentation Provided <input type="checkbox"/> Signed PR Report or, <input type="checkbox"/> Signed PR Concurrence Sheet or, <input type="checkbox"/> Signature of PR Reviewer(s) below
--	--

Name and Signature of Reviewers
 Patrick V. Brady



NOTE 1: Appendix E should be filled out and submitted with the deliverable. Or, if the PICS:NE system permits, completely enter all applicable information in the PICS:NE Deliverable Form. The requirement is to ensure that all applicable information is entered either in the PICS:NE system or by using the NTRD Document Cover Sheet.

- In some cases there may be a milestone where an item is being fabricated, maintenance is being performed on a facility, or a document is being issued through a formal document control process where it specifically calls out a formal review of the document. In these cases, documentation (e.g., inspection report, maintenance request, work planning package documentation or the documented review of the issued document through the document control process) of the completion of the activity, along with the Document Cover Sheet, is sufficient to demonstrate achieving the milestone.

NOTE 2: If QRL 1, 2, or 3 is not assigned, then the QRL 4 box must be checked, and the work is understood to be performed using laboratory QA requirements. This includes any deliverable developed in conformance with the respective National Laboratory / Participant, DOE or NNSA-approved QA Program.

NOTE 3: If the lab has an NQA-1 program and the work to be conducted requires an NQA-1 program, then the QRL-1 box must be checked in the work Package and on the Appendix E cover sheet and the work must be performed in accordance with the Lab's NQA-1 program. The QRL-4 box should not be checked.

ACKNOWLEDGEMENTS

This work was supported by the US Department of Energy (DOE) Office of Nuclear Energy, through the Office of Spent Fuel and Waste Science and Technology (SFWST), within the Office of Spent Fuel and Waste Disposition (DOE NE-8).

Thanks go to our DOE customer for their support of this work. Thank you to Glenn Hammond and Heeho Park for their contributions to PFLOTRAN capability in support of the unsaturated zone reference case, to Kris Kuhlman for assisting the salt reference case, and to LianGe Zheng and Jonny Rutqvist of Lawrence Berkeley National Laboratory for their input to the shale geomechanical analysis. Finally, thanks to our technical reviewer, Pat Brady, for comments and suggestions that improved the report.

EXECUTIVE SUMMARY

The Spent Fuel and Waste Science and Technology (SFWST) Campaign of the U.S. Department of Energy Office of Nuclear Energy, Office of Spent Fuel and Waste Disposition (SFWD), has been conducting research and development on generic deep geologic disposal systems (i.e., geologic repositories). This report describes specific activities in the second half of Fiscal Year (FY) 2019 associated with the Geologic Disposal Safety Assessment (GDSA) Repository Systems Analysis (RSA) work package within the SFWST Campaign. The overall objective of the GDSA RSA work package is to develop generic deep geologic repository concepts and system performance assessment (PA) models in several host-rock environments, and to simulate and analyze these generic repository concepts and models using the *GDSA Framework* toolkit, and other tools as needed. The specific objectives in FY2019 are to

- Develop and/or augment generic repository reference cases for liquid-saturated host rock environments, particularly in argillaceous (e.g., typical shale or clay) host rocks; and a host rock environment in the unsaturated zone (UZ), such as alluvial valley fill.
- Ensure that reference cases include repository concepts and layouts for the disposal of DPC-canisterized pressurized water reactor (PWR) assemblies, including 37-PWR and 24-PWR waste packages.
- Perform PA simulations (deterministic and probabilistic) with *GDSA Framework* for the foregoing reference case concepts and models. Analyze and plot the PA simulation results, including uncertainty and sensitivity analyses.

This report describes specific GDSA RSA accomplishments in the second half of FY2019 and builds upon the work reported in M2SF-19SN010304051, *GDSA Repository Systems Analysis Progress Report* (Sevougian et al. 2019b).

Section 1 of this deliverable is a brief introduction. Section 2 discusses the relationship of reference case models to the overall generic safety case(s). Section 3 discusses two improvements to the numerical solvers in PFLOTTRAN, needed for modeling the high heat output from dual purpose canister (DPC) waste packages, particularly during two-phase flow, such as might occur in an unsaturated host-rock environment. Multiphase (liquid and gas) flow and transport capabilities in PFLOTTRAN (under the “GENERAL” flow mode) have been augmented to more efficiently simulate physically complex processes that could occur in unsaturated repositories and/or under conditions of extreme waste package heat production (as could be the case with a 37-PWR configuration). The most significant of these changes involved refactoring of convergence criteria used during each iteration of the Newton-Raphson nonlinear solution search algorithm. Many of these improvements are reported in Sevougian et al. (2019b, Sec. 3.1) and in the recent work described Mariner et al. (2019, Sec. 2.3.1.5).

Section 3 also discusses some significant progress in interfacing the Sandia VoroCrust meshing software with PFLOTTRAN. VoroCrust is a software tool that generates Voronoi meshes of arbitrary volumes (Abdelkader et al. 2018). The long-term goal is to develop a meshing software tool that is open-source, flexible, and well-suited for meshing geologic and engineered features. In FY2019, the project focused on converting VoroCrust output to the grid format required by PFLOTTRAN, generating meshes of simple test cases representative of common geologic features (see also Gross et al. 2019), and benchmarking simulations on VoroCrust meshes against other unstructured and structured grids representing the same geometry. In the past six months,

substantial progress has been made. Meshes for five example problems have been created and solutions obtained on them have been verified against solutions obtained on other meshes.

Section 4 presents simulations of a reference case repository located in unsaturated alluvial sediments (Mariner et al. 2018), building on the simulations presented in Sevougian et al. (2019b). The primary development for this reference case in FY2019 is related to the inclusion of DPC waste packages and their representative higher heat output per package, which results in more severe coupled process effects at early times after repository closure and associated slow convergence of the numerical algorithm. The initial task in Section 3 was to test a new potentially faster converging parallel solver called the Newton trust region (TR) algorithm. In all five models benchmarked here this solver gave the same results as the default Newton line search (LS) solver. The TR method was also much faster.

Finally, Section 4 points to FY2019 work detailed in Gross et al. (2019) that is intended to interface with the GDSA UZ alluvium reference case. In particular, Gross et al. (2019) describe the development of a new geologic framework model (GFM) for alluvial basins. In that work development of a stratigraphic and hydrological model of the Mimbres Basin from available seismic and well data is detailed. A GFM must capture the geologic elements that impact the siting and dynamic behavior of a potential repository, including basin geometry, alluvium stratigraphy, lithofacies and geologic structures. The first step, and the focus of Gross et al. (2019), is to establish the geologic elements that define the boundaries of the alluvial sub-basin, such as depth to bedrock, basin-bounding and intra-basin faults, and the geometry of the bed rock on which the alluvial basin-fill sediments were deposited. Eventually, the generic basin-scale GFM (whether in alluvium or some other host rock) will interface with the GDSA repository-scale generic reference case.

Section 5 is an update to the generic shale reference case (Mariner et al. 2017). Section 5.1 describes an update to the Geologic Framework Model (GFM) for a representative shale environment and describes the geologic and hydrogeologic features represented in the GFM. The methodology used to develop the shale GFM is documented in detail in Sevougian et al. (2019b). In this current deliverable, updates to the features of the shale GFM first shown in Sevougian et al. (2019b) are presented and analytical methods are used to document the relationships between features represented in the GFM. Also updated are features and processes specific to the region of the shale GFM. The shale GFM was developed using RockWorks17® software (Rockware Inc., www.rockware.com) and ArcGIS 10.6 (ESRI, www.esri.com). The GFM was gridded at a horizontal resolution of 250 meters and a vertical resolution of 10 meters resulting in a grid array of 277 by 333 by 201. New features include a synthetic fault that offsets the stratigraphy of the GFM and inclusion of the water table in this region. A series of analyses are conducted using the GIS and GFM software to document the relationships between the reference repository horizon, the host formation, and hydrologic features represented in the GFM. Although these analyses are applied to a relatively simple geologic environment, they demonstrate how the analytical tools available in GIS and GFM software can be used to evaluate areas where a repository could be located using basic criteria such as depth and thickness of the potential host formation. One of the goals in developing the shale GFM is to demonstrate a workflow that uses the features of the GFM to create a mesh for simulation modeling. This is accomplished by exporting the geologic surfaces (formation tops) for input into the meshing software. Generating a simulation mesh from the geologic surfaces generated by Rockworks required a multistep process using Python, CUBIT and SCULPT software.

Section 5.2 documents some near-field simulations with a highly discretized grid in the shale reference case, as a precursor to coupling more detailed process models into *GDSA Framework*. The objective of this study is to investigate the near-field thermal-hydrologic-mechanical (THM) behavior in a typical bentonite back-filled shale repository with the goal of representing the effect of stresses due to bentonite swelling, thermal expansion, and pore pressure changes on the permeability of the disturbed rock zone (DRZ) in a performance assessment model of the entire repository system. To model these phenomena a combination of empirical and theoretical relationships derived from coupled THM simulations can be represented as functions of PFLOTRAN TH state variables.

Finally, Section 5.3 describes a site-scale shale-host-rock reference case that models the potential performance of a geologic repository based on direct disposal of DPC waste packages. This section presents the FY2019 update to the GDSA Shale Reference Case described in Section 4 of Mariner et. al (2017). The primary new tasks undertaken in FY2019 were

- (1) Inclusion of 24-PWR and 37-PWR DPC waste packages in the reference case simulations.
- (2) An update to the stratigraphic model for a representative shale domain (Perry et al. 2014; Perry and Kelley 2017)—see description of Section 5.1 above.
- (3) An update to the numerical model grids and formation properties to incorporate changes to stratigraphy and repository design needed for DPC waste packages.

This report fulfills the FY2019 GDSA Repository Systems Analysis work package (SF-18SN01030405) Level 3 milestone entitled *GDSA Repository Systems Analysis FY19 Update* (M3SF-19SN010304052).

This page intentionally left blank.

CONTENTS

ACKNOWLEDGEMENTS.....	iv
EXECUTIVE SUMMARY	v
CONTENTS.....	ix
FIGURES.....	xi
TABLES	xvii
ACRONYMS.....	xviii
1 INTRODUCTION.....	1
2 SAFETY CASE AND REFERENCE CASE METHODOLOGY	3
3 PFLOTRAN UPDATES	6
3.1 PFLOTRAN Updates.....	6
3.2 VoroCrust/PFLOTRAN Collaboration.....	6
3.2.1 Meshing in VoroCrust.....	6
3.2.2 Unit Cube Examples (Test Case 0).....	7
3.2.3 Test Problems with Heterogeneity.....	9
3.2.4 Conclusions and Future Work.....	19
4 GENERIC UNSATURATED ZONE REFERENCE CASE.....	21
4.1 Post-Closure Repository Modelling.....	21
4.1.1 Code Development.....	21
4.2 Site-scale Models	22
4.2.1 A Question of Solvers.....	24
4.2.2 Site-Scale Model Comparison Across Grid Refinement.....	25
4.2.3 Single WP Model.....	31
4.2.4 Comparison Across Model Scales	34
4.3 Conclusions and Considerations for Future PA Modelling	35
4.4 Geologic Framework Model	36
5 GENERIC SHALE REFERENCE CASE.....	37
5.1 Geologic Model for the Shale Reference Case	37
5.1.1 Update of the Shale GFM for the Argillite Reference Case	37
5.1.2 Update of the Shale Conceptual Model for the Region of the GFM.....	47
5.2 Reduced Order Modeling and Geomechanical Analysis	51
5.2.1 Geomechanical Analysis.....	52
5.2.2 Model Setting.....	54
5.2.3 Preliminary Results.....	55
5.2.4 Considerations for Future Work	64
5.3 Updated Shale Reference Case PA Model and Simulations	65
5.3.1 Engineered Barriers.....	67
5.3.2 Geosphere/Natural Barriers.....	72

5.3.3 Post-Closure Performance Assessment..... 75

6 SUMMARY AND CONCLUSIONS 87

7 REFERENCES 90

FIGURES

Figure 2-1. Typical components of a deep geologic repository safety case.	3
Figure 2-2. Evolution and iteration of the technical bases and performance assessment via RD&D through multiple stages of repository development (after Sevougian et al. 2018).	4
Figure 2-3. Information flow and the role of performance assessment for RD&D prioritization during a single stage of repository development (after Sevougian and MacKinnon 2017).	5
Figure 3-1. VoroCrust meshes with 101, 697 and 2860 cells for the unit cube example.	8
Figure 3-2. Steady state distribution of pressure (left) and temperature (right) on the unit cube. This hexahedral mesh is used as a benchmark.	8
Figure 3-3. Temperature and pressure at an observation point near the center of the domain. All simulations have exactly the same observation point.	9
Figure 3-4. Temperature and pressure at an observation point near the center of the domain. Some of the difference in the profiles is due to the observation point moving slightly between the meshes.	9
Figure 3-5. Simulation meshes for Test Case 1. Top: Voronoi mesh with 11,005 grid cells. Bottom: Hexahedral benchmark mesh with 10,000 grid cells showing Material ID assignments.	10
Figure 3-6. Temperature (left) and liquid saturation (right) for Test Case 1 after 0.1 years of simulation.	11
Figure 3-7. Profiles of temperature (left) and liquid saturation (right) for three observation points in Test Case 1. Two simulations on hexahedral meshes are shown along with the simulation on the Voronoi mesh. M1 is in Material 1, M3 is in Material 3 and M4 is in Material 4.	12
Figure 3-8. Coarse hexahedral (left) and Voronoi (right) meshes for Test Case 2 which has Material 2 pinching out in the interior of the domain.	12
Figure 3-9. Simulated liquid saturation (left) and temperature (right) on the coarse hexahedral mesh on Test Case 2 at 1 hour.	14
Figure 3-10. Simulated temperature (left) and saturation (right) versus time at three observation points for Test Case 2. M1 is centrally located in Material 1. M2a is centrally located in Material 2 and M3 is centrally located in Material 3.	14
Figure 3-11. Voronoi surface mesh for Test Case 3. This mesh has approximately 22,000 elements.	15
Figure 3-12. Hexahedral mesh of Test Case 3. Top left: XZ slice through the center of the domain to show the interior lens. Top right: the surface mesh of this model is all orthogonal hexahedral elements. Bottom: XY slice through the lens. This mesh has over half a million elements.	15
Figure 3-13. Simulated pressure (left) and saturation (right) profiles at the four observation points for Test Case 3. Observation points are all in the plane of the lens at a depth of $z = -4\text{m}$	16
Figure 3-14. Hexahedral (left) and Voronoi (right) meshes for Test Case 4 which has an offset fault through the interior of the domain.	17

Figure 3-15. Simulated liquid saturation (left) and temperature (right) on hexahedral mesh on Test Cast 4 after 10 years. 18

Figure 3-16. Simulated temperature (left) and saturation (right) versus time at four observation points for Test Case 4. M1 is centrally located in Material 1. M2 LT is in Material 2 to the left of the fault, M2 RT is in Material 2 to the right of the fault, and M3 is centrally located in Material 3. Simulations for a coarse and refined hexahedral mesh are shown as well as the results on the Voronoi mesh. 18

Figure 3-17. Voronoi mesh of a highly anisotropic geologic model with seven layers of varying thickness. The detail section shows that the mesh is able to capture thin layers exactly, but at the cost of very small grid cells..... 20

Figure 4-1. Plan view (*XY* slice) of the northeast corner of the repository in the four meshes of varying grid resolution..... 23

Figure 4-2. Vertical cross-section (*XZ* slice) through the repository including the repository area and full model depth. All grids preserve stratigraphic features. Four meshes of varying grid resolution are shown. 23

Figure 4-3. Vertical cross-section (*XZ* slice) through the repository including only the area around the three drifts on the eastern edge of the repository. The four meshes of varying grid resolution are shown..... 24

Figure 4-4. Comparison of simulated gas saturation (left) and temperature (right) as a function of the log of time for the TR and LS algorithm for three of the meshes. TR simulations are shown as lines while LS simulations are shown as symbols. 26

Figure 4-5. Temperature and gas saturation as a function of time for the model that resolves the waste packages but not the DRZ (Mesh 2). Temperature (top left) and gas saturation (top right) in the centermost waste package, between two waste packages in the drift and in the alluvium at the midpoint between four waste packages. Temperature (bottom left) and gas saturation (bottom right) in the formation that contains the repository (ubf 3 over and ubf 3 below—observation points in the upper basin fill just above and beneath the repository horizon) and in the confining beds above (confining 2) and below (confining 3) the repository. 27

Figure 4-6. Plan view (*XY* slice) of saturation in the north east corner of the repository at time $t = 20$ yr. This is near time of the maximum temperature in the waste packages for the refined simulations. Top left (Mesh 1): fully resolved simulation. Top right (Mesh 2): simulation that resolves waste packages but not the DRZ. Bottom left (Mesh 3): simulation that resolves drifts but not waste packages. Bottom right (Mesh 4): Simulation that does not resolve the repository and has backfill throughout the repository area. 28

Figure 4-7. Plan view (*XY* slice) of saturation in the north east corner of the repository at time $t = 80$ yr. This is the final snapshot of the simulation on the fully-resolved mesh. Top left (Mesh 1): fully resolved simulation. Top right (Mesh 2): simulation that resolves waste packages but not the DRZ. Bottom left (Mesh 3): simulation that resolves drifts but not waste packages. Bottom right (Mesh 4): Simulation that does not resolve the repository and has backfill throughout the repository area. 28

Figure 4-8. Plan view (*XY* slice) of saturation in the north east corner of the repository at time $t = 500$ yr. This is near time of the maximum dry out between the drifts for the refined simulations. Top left (Mesh 1): fully resolved simulation is not shown because it did not progress to this time. Top right (Mesh 2): simulation that resolves waste

packages but not the DRZ. Bottom left (Mesh 3): simulation that resolves drifts but not waste packages. Bottom right (Mesh 4): Simulation that does not resolve the repository and has backfill throughout the repository area.....	29
Figure 4-9. Gas saturation (left) and temperature (right) in the waste package for all 5 simulations.....	29
Figure 4-10. Gas saturation (left) and temperature (right) between two central drifts for all 5 simulation models.....	30
Figure 4-11. Gas saturation (left) and temperature (right) in the confining zone below the repository for all 5 simulation models.....	30
Figure 4-12. Section of the site-scale domain represented by the single waste package model is shown in the black square.....	31
Figure 4-13. Left: Materials in the center section of the single waste package model. Waste package is Material 8, drift is Material 5, DRZ is Material 6 low permeability alluvium is Material 3 and high permeability alluvium is Material 4. Right: Gas saturation is lower in material 4 (high permeability) than material 3 (low permeability), like in full model. Simulation mesh is also shown. The full thickness of the model in the z direction is not shown.....	32
Figure 4-14. Top Left: simulated liquid saturation (left) and temperature (right) for 24-PWR waste package at 10 yrs, the time of peak temperature in the waste package. Top right: simulated liquid saturation (left) and temperature (right) at 50 years. Bottom left: simulated liquid saturation (left) and temperature (right) at 250 years. Bottom right: simulated liquid saturation (left) and temperature (right) at 1000 years, the time of maximum dry out.....	33
Figure 4-15. Temperature and gas saturation as a function of time for the ¼ waste package model. Temperature (top left) and gas saturation (top right) in the center of the waste package (in WP), in the drift halfway to the next waste package (in drift), and the midpoint between two drifts (equidistant 4 WP). Temperature (bottom left) and gas saturation (bottom right) in the formation that contains the repository (ubf 3 over and ubf 3 below—observation points in the upper basin fill just above and beneath the repository horizon) and in the confining beds above (confining 2) and below (confining 3) the repository.....	34
Figure 4-16. Saturation (left) and temperature (right) in and between the waste packages for the ¼ waste package model and the two site-scale models that resolve the waste packages.....	35
Figure 5-1. Location of the shale GFM and boreholes used as data inputs. The surface geology shown within the boundary of the GFM region is from Martin et al. (2004). Thickness contours for the Pierre Shale are from Perry et al. (2014). Note that the Pierre Shale is thinned by erosion where it ramps onto the Black Hills uplift.....	38
Figure 5-2. Block diagram of the stratigraphy represented in the GFM. View is from the northeast at 10x vertical resolution. Vertical scale is elevation relative to sea level. The Fox Hills Formation and parts of the Pierre Shale are at the modern erosional surface. The base of the GFM is the bottom of the Madison Group. The Precambrian surface (McCormick 2010) below the base of the Madison Group is shown for reference but is not part of the GFM.....	39
Figure 5-3. Synthetic fault (red surface) offsetting the upper four stratigraphic units in the Shale GFM. View is from the northeast at 10x vertical exaggeration. The fault is vertical and offsets each of the stratigraphic units by 250 meters.....	41

Figure 5-4. Depth (left) and elevation (right) of the water table in the GFM. 42

Figure 5-5. 3-D view of the relationship between the top of the Pierre Shale (gray surface) and the water table (blue surface). View is from the northeast with a vertical exaggeration of 10x. In much of the area, the water table lies above the top of the Pierre Shale within the Fox Hills Formation. The water table surface is the equivalent of the map view of elevation in Figure 5-4. Vertical scale is in meters relative to sea level. 43

Figure 5-6. 2-D and 3-D representations of the relationships between a reference repository depth of 400 meters and the top and bottom of the Pierre Shale. In the 3-D view (bottom panel) the repository depth is the red surface and the semi-transparent gray volume is the Pierre Shale. The base of the Pierre shale is shown in yellow. View is from the southwest at a vertical exaggeration of 10x. Shown for scale is the shale reference repository footprint (black) that is pinned to the repository depth surface (front left of bottom panel)..... 44

Figure 5-7. Distance of the water table from 400-m depth repository horizon. The distance represents the thickness of the saturated zone above the repository horizon..... 45

Figure 5-8. Depth (distance) of the Inyan Kara aquifer below the 400-m depth repository horizon..... 46

Figure 5-9. View of the GFM from the northwest showing the relationships between the water table and Inyan Kara aquifer (blue surfaces), the Pierre Shale (semi-transparent gray, base is yellow) and the reference repository depth (red surface). The base of the Fox Hills aquifer is approximately coincident with the top of the Pierre Shale. 46

Figure 5-10. Surfaces (formation tops) used as the basis for meshing the features of the GFM. 47

Figure 5-11. Results of the meshing process represented as formation volumes (left) and a hexahedral mesh (right). View is from the northeast at 30x vertical exaggeration. 48

Figure 5-12. E-W cross-section through the eastern margin of the Black Hills uplift (Driscoll et al. 2002). Major regional aquifers are the Madison (MDme), the Minnelusa (PPm), and the Inyan Kara (Kik). The Pierre Shale and underlying Cretaceous shales are the upper confining unit (Kps)..... 49

Figure 5-13. View to the west of the Black Hills uplift and outcrop area of the Inyan Kara Group (yellow pattern) relative to the boundary of the GFM. The southwest corner of the GFM boundary is 35 kilometers from the closest Inyan Kara outcrop. The outer margins of the Inyan Kara outcrops mark the outer boundary of artesian springs in the Black Hills region. The blue arrow indicates the general direction of groundwater flow within aquifers that are recharged in the Black Hills. The green arrow indicates the general direction of groundwater flow within the Fox Hills aquifer. 50

Figure 5-14. Formations of the Pierre Shale Group. Western (left) column are formations recognized in western South Dakota/North Dakota and Eastern Wyoming including the region around the Black Hills uplift. Central/Eastern (right) column refers to formations recognized in the central South Dakota and in eastern South Dakota/North Dakota (Martin et al., 2007; Fahrenbach et al., 2007) The lower Pierre Shale Group includes the formations below the top of the Red Bird Silty Formation. Figure modified from Korn and Pagnac (2017)..... 51

Figure 5-15. Near-field model domain used in PFLOTRAN simulation..... 52

Figure 5-16. Schematic description of the geomechanical analysis of a cylindrical drift in 2D. The repository is assumed to be parallel to the direction of $S_{H,max}$ 53

Figure 5-17. Decay heat source terms used as the basis for the near-field simulation $\frac{1}{4}$ waste package for 12-PWR 100 years OOR (Mariner et al. 2017); 24-PWR 100 years OOR, and 37-PWR (150 years OOR) waste packages (see Section 5.3.1.2). 55

Figure 5-18. Spatio-temporal distribution of gas saturation (S_g) for a 12-PWR heat source. 56

Figure 5-19. Spatio-temporal distribution of liquid pressure (MPa) for a 12-PWR heat source. 57

Figure 5-20. Spatio-temporal distribution of temperature (C) for a 12-PWR heat source..... 58

Figure 5-21. Temporal distribution of swelling stress ($\sigma_{swelling}$), poroelastic stress driven by pore pressure change ($\sigma_{h,p}$) and thermal stress due to temperature change ($\sigma_{h,T}$) at the far-field edge of the domain. 59

Figure 5-22. Evolution of DRZ permeability over time. 60

Figure 5-23. Temperature profile and gas saturation at the center of the simulated waste package..... 61

Figure 5-24. Simulation temperature over 1000 years using a 24-PWR heat source. 62

Figure 5-25. Simulated gas saturation throughout the domain over 1000 years for a 24-PWR heat source..... 63

Figure 5-26. Temperature and gas pressure as a function of time at the center of the waste package (edge of the simulation domain) for a 24-PWR waste package..... 63

Figure 5-27. Simulated gas pressure profiles over 1000 years for a 24-PWR heat source. 64

Figure 5-28. Locations of areally extensive shale formations in the U.S. Shale formations of an appropriate depth are the darker shades of blue (Perry et al. 2014; Mariner et.al. 2017, Figure 4-1). 66

Figure 5-29. Waste package heat source terms for the shale reference case. 70

Figure 5-30. Schematic cross-section of a single-layer buffer in a 24- or 37-PWR disposal drift of a generic shale repository. 72

Figure 5-31. Generic stratigraphic column for shale reference case simulations. 73

Figure 5-32. Transparent view of the 24- and 37-PWR model domain colored by material. The repository (red) is 500 m from the west (left) face of the domain and 405 m below the top face of the domain. 40-m long hallways connect the disposal panel to the south (front) face of the domain, which is a reflection boundary. Shades of blue correspond to the stratigraphic column in Figure 5-31. 77

Figure 5-33. XY slice through the repository colored by material: blue, host rock; orange, DRZ; shades of red, buffer and waste packages, which cannot be distinguished from each other at this scale. The base of the figure is the south face of the model domain, which is a reflection boundary. A vertical shaft is gridded at either end of the southern-most hall, which is approximately 1685 m long. 78

Figure 5-34. In-drift temperature (TH mode) and temperature, liquid saturation, and gas pressure (GENERAL mode) at interior 24-PWR and 37-PWR waste packages. Dashed lines (blue, turquoise and green) are 24-PWR waste package, buffer, and DRZ. Solid lines (red, orange, and yellow) are 37-PWR waste package, buffer, and DRZ. Gas pressure is zero where liquid saturation is one. 81

Figure 5-35. Cumulative number of waste packages breached versus time in TH mode (left) and GENERAL mode (right) simulations. 82

Figure 5-36. ¹²⁹ I concentration at 1000 yr in the GENERAL mode simulation plotted in a horizontal slice through the model domain at the elevation of the repository.	83
Figure 5-37. ¹²⁹ I concentration at 10,000 yr in the GENERAL mode simulation plotted in a horizontal slice through the model domain at the elevation of the repository.	84
Figure 5-38. ¹²⁹ I concentration at 100,000 yr in the GENERAL mode simulation plotted in a vertical slice through the model domain at the Y-midpoint of the repository.	84
Figure 5-39. ¹²⁹ I concentration at 1,000,000 yr in the GENERAL mode simulation plotted in a vertical slice through the model domain at the Y-midpoint of the repository.	84
Figure 5-40. Locations of upper sandstone aquifer observation points.	85
Figure 5-41. ¹²⁹ I concentration versus time at each of the three upper sandstone aquifer observation points in TH mode (left) and GENERAL mode (right) simulations.	85
Figure 5-42. ³⁶ Cl concentration at 1,000,000 yr in the GENERAL mode simulation plotted in a vertical slice through the model domain at the Y-midpoint of the repository.	86
Figure 5-43. ²³⁷ Np concentration at 1,000,000 yr in the GENERAL mode simulation plotted in a vertical slice through the model domain at the Y-midpoint of the repository.	86

TABLES

Table 3-1. Material properties for Test Case 1. Material IDs are assigned as shown in Figure 3-5.	11
Table 3-2. Initial and boundary conditions for Test Case 1.	11
Table 3-3. Material properties for Test Case 2. Material IDs are assigned as shown in Figure 3-8.	13
Table 3-4. Initial and boundary conditions for Test Case 2.	13
Table 3-5. Material properties for Test Case 4. Material IDs are assigned as shown in Figure 3-14.	17
Table 3-6. Initial and boundary conditions for Test Case 4.	17
Table 4-1. Simulation time for all four meshes with both the experimental Newton TR and default Newton LS solvers. All simulations are run with identical input options and time stepping routine. Maximum wall clock time was set to 48 hours.	25
Table 5-1. Stratigraphic and hydrologic properties of formations represented in the GFM.	40
Table 5-2. Rock and fluid properties for hydrological characteristics of the near-field model.	54
Table 5-3. Parameter values used in the preliminary analysis of geomechanical stability of the nuclear waste repository (Rutqvist et al. 2011; Zoback 2007).	59
Table 5-4. Comparison of current (2019) GDSA simulations to 2017 shale reference case GDSA simulations. Inventory count (MTHM and number of waste packages) includes <i>the virtual inventory beyond the reflection boundary condition</i>	67
Table 5-5. Dimensions and counts for the 24- and 37-PWR repository layout compared to the 12-PWR repository layout (Mariner et al. 2017).	68
Table 5-6. 24-PWR SNF inventory (40 GWd/MTHM burnup, 100-year OoR) of selected radionuclides for the shale reference case.	69
Table 5-7. 37-PWR SNF inventory (60 GWd/MTHM burn-up, 150-year OoR) of selected radionuclides for the shale reference case.	70
Table 5-8. Element solubility limits for clay reference case (Clayton et al. 2011, Table 3.3-23).	75
Table 5-9. Linear distribution coefficients (K_d) for clay reference case elements.	76
Table 5-10. Conceptual representation of key components in PA.	76
Table 5-11. Isotope instant release fractions recommended by Sassani et al. (2012) for PWR with 60 GWd/MTHM burn-up.	79
Table 5-12. SNF dissolution rates; log triangular distribution from cited SKB (2006) in Sassani et al. (2016, Section 3.2.1)	79
Table 5-13. Parameter values used in deterministic simulations.	80
Table 5-14. Time to reach maximum waste package temperature.	82

ACRONYMS

CD	Critical Decision
CSNF	Commercial Spent Nuclear Fuel
DOE	U.S. Department of Energy
DPC	Dual Purpose Canister
DRZ	Disturbed Rock Zone
EBS	Engineered Barrier System
FEP	Feature, Event, and Process
FY	Fiscal Year
GDSA	Geologic Disposal Safety Assessment
GFM	Geologic Framework Model
HLW	High-Level Radioactive Waste
IAEA	International Atomic Energy Agency
IRF	Instant Release Fraction
MTHM	Metric Tons Heavy Metal
NBS	Natural Barrier System
OoR	Out-of-Reactor
PA	Performance Assessment
PWR	Pressurized Water Reactor
R&D	Research and Development
RD&D	Research, Development, and Demonstration
SFWST	Spent Fuel and Waste Science and Technology
SNF	Spent Nuclear Fuel
TH	Thermal-Hydrologic
THM	Thermal-Hydrologic-Mechanical
UZ	Unsaturated Zone
WF	Waste Form
WP	Waste Package

1 INTRODUCTION

The Spent Fuel and Waste Science and Technology (SFWST) Campaign of the U.S. Department of Energy (DOE) Office of Nuclear Energy, Office of Spent Fuel and Waste Disposition (SFWD), is conducting research and development (R&D) on geologic disposal of spent nuclear fuel (SNF) and high-level nuclear waste (HLW). Two of the highest priorities for SFWST disposal R&D are design concept development and disposal system performance assessment (PA) modeling (DOE 2012, Table 6). Generic design (or reference-case) concepts being considered for SNF and HLW disposal since 2010 include mined repository concepts in bedded salt, argillite (shale), and crystalline rock. An additional option begun last fiscal year is a potential mined repository in unsaturated alluvium. The PA R&D since 2012 has mostly focused on disposal of commercial spent nuclear fuel (CSNF) inventory packaged in smaller waste packages, such as 4-PWR and/or 12-PWR waste packages. However, a greater emphasis is given this year to simulating direct disposal of much higher decay-heat waste packages containing dual purpose canisters (DPCs) with 37 pressurized water reactor (PWR) assemblies or 24 PWR assemblies, which now represent a significant fraction of the spent fuel inventory currently being stored at U.S. reactor sites.

This report describes accomplishments for the second half of Fiscal Year (FY) 2019 in the development of generic repository reference cases and PA modeling and analysis. Prior development and accomplishments are summarized at a high-level in Mariner et al. (2019), with much more detail provided in Mariner et al. (2018), Mariner et al. (2017), Mariner et al. (2016), Mariner et al. (2015), Sevougian et al. (2016), Sevougian et al. (2014), Sevougian et al. (2013), Sevougian et al. (2012), Freeze et al. (2013a), and Vaughn et al. (2013), as well as previous work in the first half of FY2019, described in Sevougian et al. (2019b).

The overall objective of the GDSA Repository Systems Analysis work package is to develop generic deep geologic repository concepts and system Performance Assessment (PA) models in several host-rock environments, and to simulate and analyze these generic repository concepts and models using the *GDSA Framework* toolkit (Mariner et al. 2019), and other tools as needed. The goals in FY19 are to

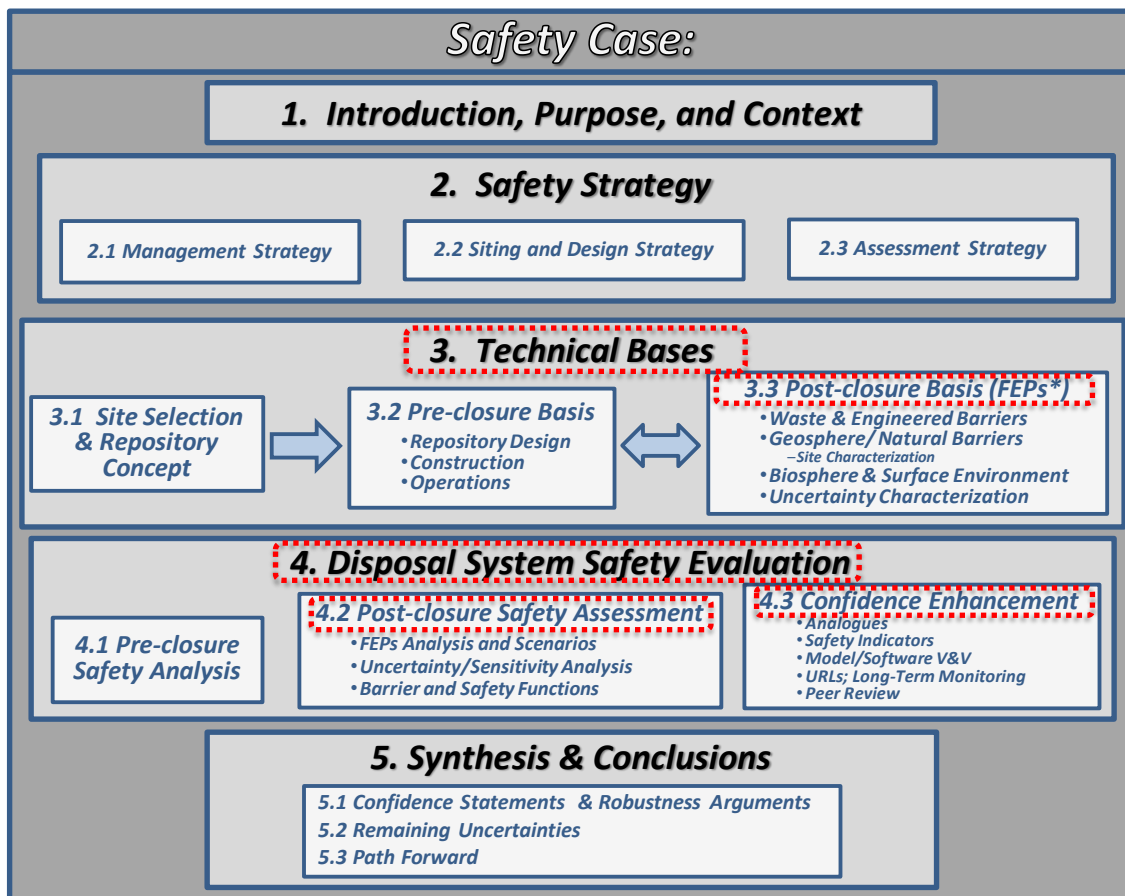
- Develop and/or augment generic repository reference cases for liquid-saturated host rock environments, particularly in argillaceous (e.g., typical shale or clay) host rocks; and a host rock environment in the unsaturated zone (UZ), such as alluvial valley fill.
- Ensure that reference cases include repository concepts and layouts for the disposal of DPC-canisterized PWR assemblies, including 37-PWR and 24-PWR waste packages, which have a higher decay heat output in comparison to prior-year PA cases.
- Perform and analyze PA simulations with *GDSA Framework* for the foregoing reference case concepts and models.

Section 2 of this report sets the context for this generic PA design concept and analysis work within the overall context of the safety case and with respect to a multi-decade project. Section 3 discusses improvements to the numerical solvers in PFLOTRAN, needed for modeling the high heat output from DPC waste packages, as well as some new work on numerical gridding that will improve solution accuracy. Section 4 describes simulations of a reference case repository located in unsaturated alluvial sediments, first introduced in Mariner et al. (2018), including initial simulations at smaller scales and coarser gridding that point to methods for eventually simulating multi-phase flow with heat on a fine-scale grid and a large domain. Section 5 is an update to the

generic shale reference case presented in Mariner et al. (2017). Section 5.1 documents new work on developing geologic framework models (GFMs) for the various reference cases, beginning with the shale reference case. Section 5.2 documents some near-field simulations with a highly discretized grid in the shale reference case, as a precursor to coupling more detailed thermal-hydrologic-mechanical process models into the PA system model *GDSA Framework*. Finally, Section 5.3 describes an update to the shale host rock reference case to include the effects of DPC disposal.

2 SAFETY CASE AND REFERENCE CASE METHODOLOGY

During the development of a deep geologic repository, the post-closure Performance Assessment or Safety Assessment is a primary component of the post-closure Safety Case (see IAEA 2012, Sec. 4.4), along with the underlying Technical Bases (engineering and scientific knowledge). Figure 2-1 is an illustration of the main components of a safety (or licensing) case (Freeze et al. 2013b). The red-dash boxes highlight the current generic program’s emphasis on R&D activities related to the post-closure technical bases (FEPs) and the safety assessment (Sevougian et al. 2019a; DOE 2012).



*FEP = Feature, Event, or Process

Figure 2-1. Typical components of a deep geologic repository safety case.

Figure 2-2 is a schematic illustration of the progression of these main components of a safety case (the PA and the technical bases) from a generic evaluation phase to a site-specific phase during the typical stages of any geologic disposal project. The maturation of the safety case through these various stages is driven by research, development and demonstration (RD&D) decisions made at key decision points (e.g., Critical Decision (CD) points, as described in DOE 2010), via a formal decision-making process involving major project stakeholders (e.g., see Sevougian and MacKinnon 2017). As of this writing, the U.S. program is at the indicated location on the timeline in Figure 2-2, which corresponds to generic (non-site-specific) RD&D only.

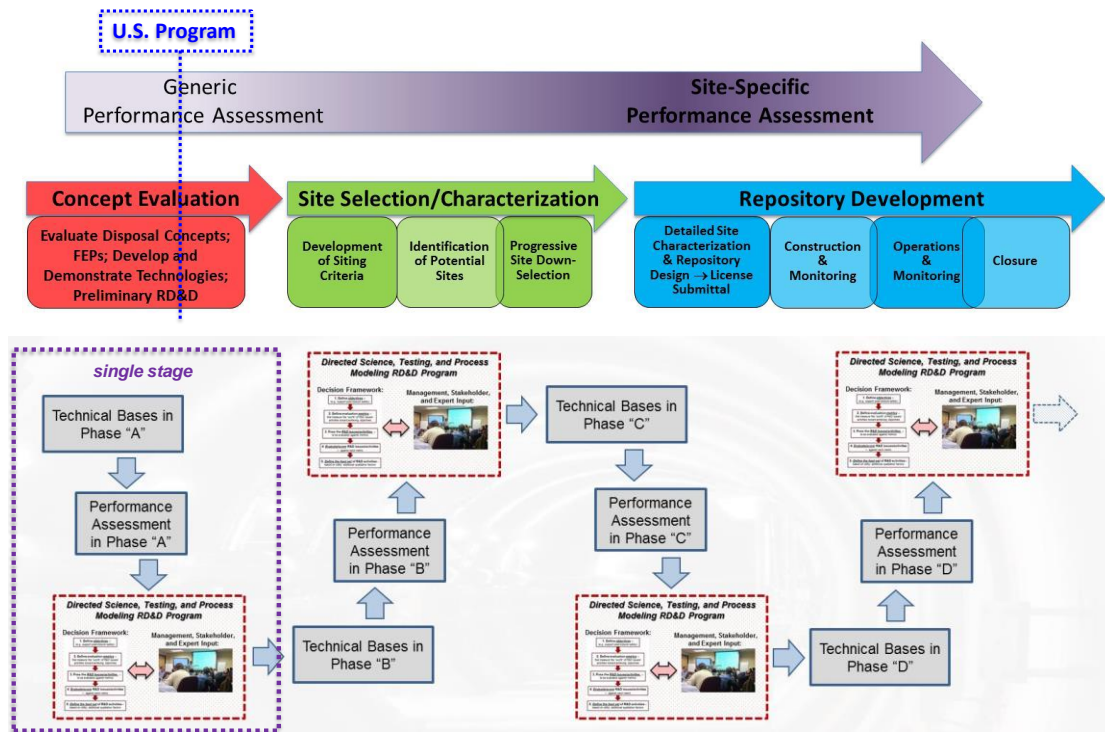


Figure 2-2. Evolution and iteration of the technical bases and performance assessment via RD&D through multiple stages of repository development (after Sevougian et al. 2018).

Figure 2-3 shows the information flow during a single stage of a repository program and how the generic PA model, *GDSA Framework*, is intended to fill a key role in guiding the directed RD&D program. The generic reference cases for potential host-rock geologic environments—argillite, crystalline, bedded salt, and unsaturated alluvium for the current work in the DOE SFWST Campaign—address the key elements of Figure 2-3 outlined by the blue dotted lines. This deliverable discusses progress in Fiscal Year 2019 in developing and simulating generic reference case repositories with *GDSA Framework*, updated for direct disposal of DPC inventory and waste packages. The specific reference cases updated here are the argillite (shale) and unsaturated alluvium reference cases (Mariner et al. 2017; Mariner et al. 2018).

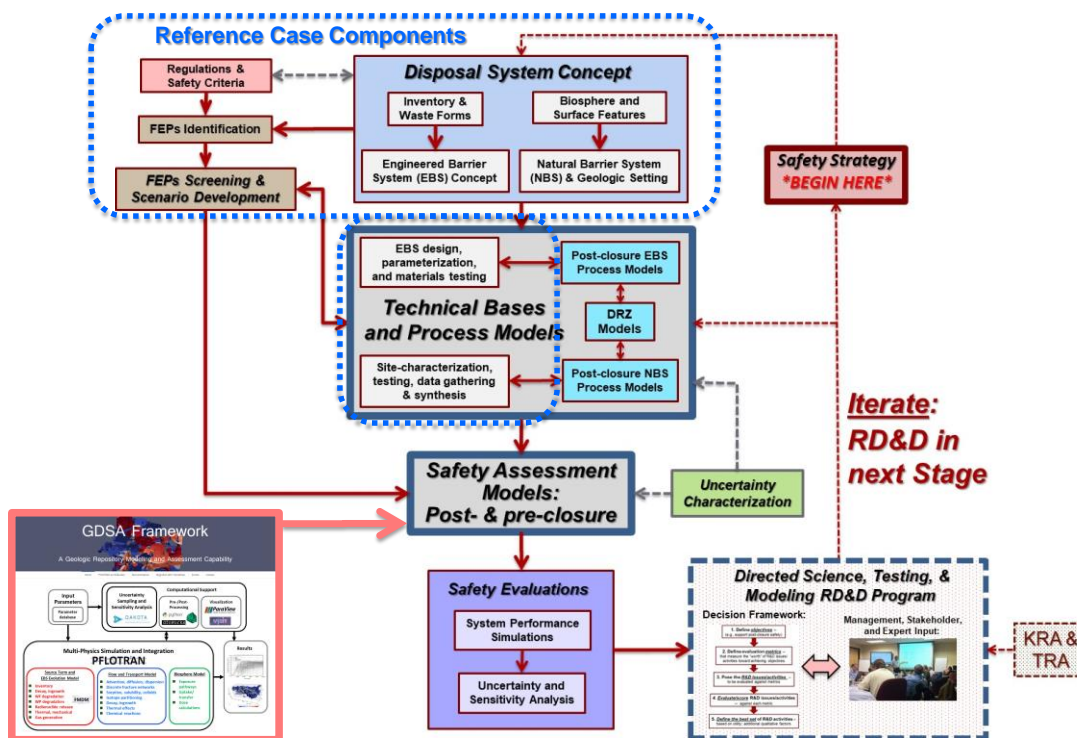


Figure 2-3. Information flow and the role of performance assessment for RD&D prioritization during a single stage of repository development (after Sevougian and MacKinnon 2017).

3 PFLOTRAN UPDATES

3.1 PFLOTRAN Updates

As described in Sevougian et al. (2019b), multiple improvements were made to the PFLOTRAN multi-physics source code to improve numerical convergence for the case of the nonlinear equations involved in multiphase fluid flow and energy transport. Since that time, some additional improvements have been made, including the “trust region” numerical algorithm described by Mariner et al. (2019, Sec. 2.3.1.5), as well as the following two options for convergence of the PFLOTRAN GENERAL Mode solver:

GAS_PHASE_AIR_MASS_DOF WATER_MOL_FRAC changes the second primary variable in gas state grid cells from the default of air partial pressure to mole fraction of water in the gas phase.

CHECK_MAX_DPL_LIQ_STATE_ONLY imposes a pressure limiter only on liquid pressure when simulation grid blocks are in the liquid state. This can be useful in situations where in 2-phase state grid blocks gas saturations get very high and capillary pressure correspondingly gets high.

To get started with using these new options and to see examples of how they work, users can now find a guide for troubleshooting multiphase flow problems in GENERAL mode in the FAQ section of the PFLOTRAN online documentation.

3.2 VoroCrust/PFLOTRAN Collaboration

A new project has been initiated to test the viability of using the VoroCrust meshing software (Abdelkader et al. 2018) to generate meshes for use in PFLOTRAN simulations. The long-term goal is to develop a meshing software tool that is open-source, flexible, and well-suited for meshing complex geologic and engineered features. In FY2019, the project focused on converting VoroCrust output to the grid format required by PFLOTRAN, generating meshes of simple test cases representative of common geologic features (see also Gross et al. 2019), and benchmarking simulations on VoroCrust meshes against other unstructured and structured grids representing the same geometry. In the past six months, substantial progress has been made. Meshes for five example problems have been created and tested.

3.2.1 Meshing in VoroCrust

VoroCrust is an automated tool that generates Voronoi polyhedral meshes that conform to complex geometries. A Voronoi mesh is a partition of the space using a set points (seeds). Each seed forms a convex cell around it by the union of the domain points that are closer to that seed compared to any other seed. A Voronoi cell has many desired features; it is convex and bounded by planar convex faces. More importantly each Voronoi face is naturally orthogonal to the line connecting the two seeds of the two Voronoi Cells defining that face. This orthogonality condition is advantageous for flow and transport codes like PFLOTRAN and FEHM (Zyvoloski et al. 2012) that utilize the finite volume method and a two-point flux approximation, since it can better approximate gradients, thereby reducing numerical dispersion for fluid fluxes that are non-orthogonal to grid-cell faces.

Voronoi partitions are uniquely defined by the locations of the seeds, and hence the VoroCrust software originally output only a list of those seeds, which were not a suitable output to use as a mesh in PFLOTRAN. In order to address this issue, an explicit Voronoi meshing method was

designed, implemented, tested. This tool is used now to produce a PFLOTRAN mesh file that contains the volume of each cell and the connectivity and the areas of the associated faces. The method relies on shooting random rays from the cell seeds to identify points on the associated Voronoi face then another set of rays are thrown from each face point to identify the Voronoi Cells that bound that face. The collected neighbors are then sorted counterclockwise direction in the plane of that face and the polygon defining that face is constructed by calculating the intersection point of four cells; the two defining that face and two successive neighbors in the sorted list. Finally, the calculated vertex is verified to be a true Voronoi vertex by closest neighbor search. If it does not pass the test, a new neighbor is added to the sorted list. Efficient intersection of random rays was achieved via a new design for a k -d tree.¹ We demonstrated the robustness of this meshing algorithm using a wide range of examples. Once the boundaries of each cell are calculated, estimating the area of each face and the volume of each cell is trivial

Orthogonal polyhedral Voronoi meshes are well-suited for meshing complex geometries for PFLOTRAN simulations. There is no constraint on cell shape, so any volume can easily be meshed. Hexahedral meshes can be flexed to capture features within the simulation domain, but generally require significantly more volume elements to achieve the same accuracy on complex geometric shapes. Thus, Voronoi meshes can be expected to significantly reduce computational times compared to hexahedral meshes (Sosnowski et al. 2017).

3.2.2 Unit Cube Examples (Test Case 0)

As a first test of the VoroCrust/PFLOTRAN simulation workflow, a series of VoroCrust meshes on a $1\text{m} \times 1\text{m} \times 1\text{m}$ unit cube with increasing number of grid cells are generated. The coarsest mesh has 16 elements while the finest has 2860. Three of the Voronoi meshes are shown in Figure 3-1.

Simulations on the Voronoi meshes are benchmarked against a simulation on a regular hexahedral mesh in which every element is cubic. In each case, the model domain has a left boundary with high pressure (111325 Pa) and low temperature (15°C) and a right boundary with lower pressure (101325 Pa) and higher temperature (25°C). The quasi-steady state pressure and temperature distributions are both nearly linear gradients in the x -direction and are shown on the hexahedral benchmark mesh in Figure 3-2.

Figure 3-3 shows the temperature and pressure profile at an observation point near the center of the domain as a function of time. All except the 16-cell mesh have extremely similar temperature profiles, while the pressure profiles for the 26- and 101-cell meshes overshoot the change in pressure at short time. Results obtained on the 2860- and 697-cell meshes are nearly identical to each other. All Voronoi mesh simulations result in nearly the same temperature and pressure profiles at quasi-steady state. It is surprising that this result is achieved on the 16- and 101-cell meshes. The 16-cell mesh has 15 of the cells connected to either the left or right boundary and only one interior cell while the 101-cell mesh has 41 boundary elements and only 60 interior nodes.

¹ A k -d tree is a data structure that utilizes a set of input points to form a partition of the underlying space. The tree is organized so that each node is associated with a hyperplane aligned with the main axis. Each node has two pointers to the two subspaces formed by that hyperplane. The hyperplane alternates directions as one traverses the tree from one node to another and the implicit partition can be utilized in fast nearest neighbor queries. One key advantage of this data structure is its low memory imprint. For n points the tree will have maximum of $2n$ pointers. The VoroCrust implementation has developed smart k -d trees, which automatically balances as more points are added.

An unstructured tetrahedral mesh and an unstructured hexahedral mesh, each with approximately 2000 elements, were developed for comparison with the Voronoi mesh. The first has 2060 tetrahedral elements and the second has 2100 hexahedral elements that were deliberately distorted to create non-orthogonal connections. Figure 3-4 shows the results of these simulations. In comparison to the benchmark mesh (regular hexahedral mesh), the tetrahedral mesh and the 2860-cell Voronoi mesh capture the evolution of temperature as steady-state is approached, but the hexahedral mesh with non-orthogonal connections performs poorly. Pressure versus time on the Voronoi mesh is superior to the other two, particularly at early time. It is likely that the slight difference in pressure between the benchmark mesh and the Voronoi mesh at quasi-steady state is due to the observation point location not being identical between the meshes.

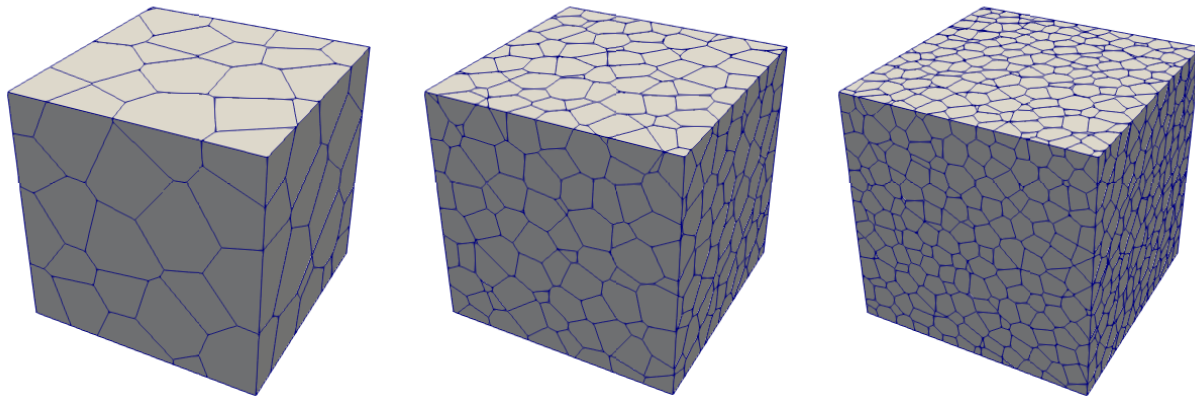


Figure 3-1. VoroCrust meshes with 101, 697 and 2860 cells for the unit cube example.

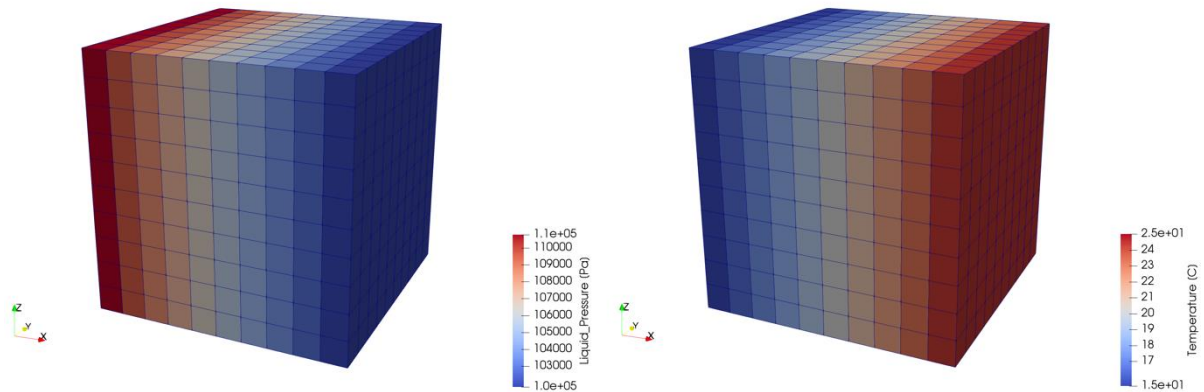


Figure 3-2. Steady state distribution of pressure (left) and temperature (right) on the unit cube. This hexahedral mesh is used as a benchmark.

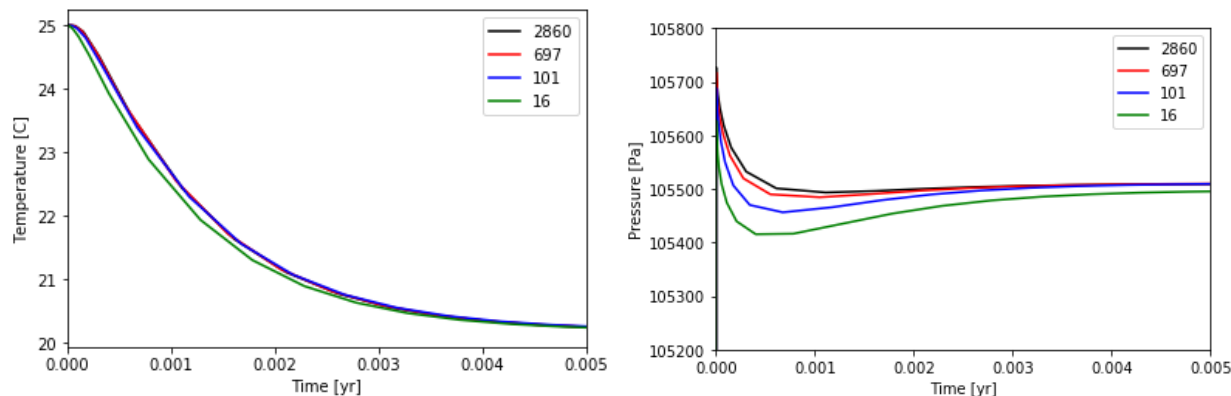


Figure 3-3. Temperature and pressure at an observation point near the center of the domain. All simulations have exactly the same observation point.

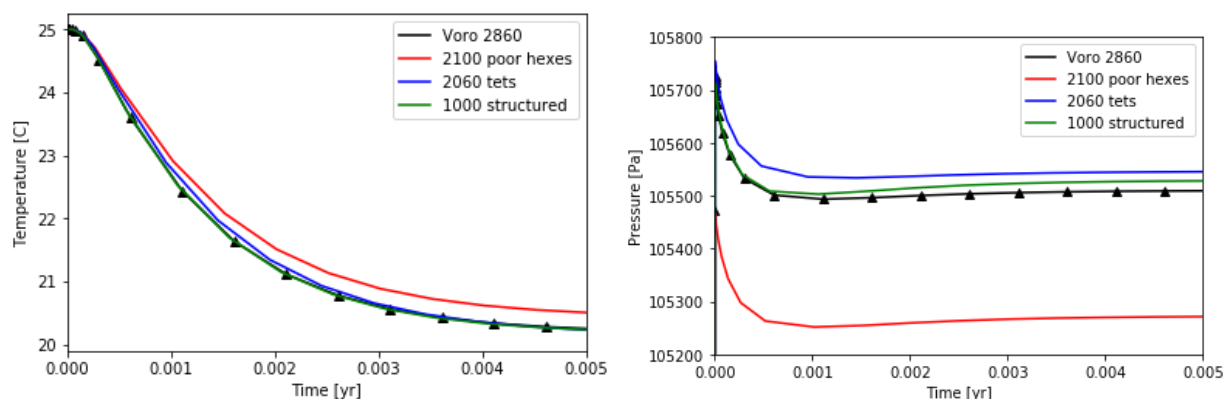


Figure 3-4. Temperature and pressure at an observation point near the center of the domain. Some of the difference in the profiles is due to the observation point moving slightly between the meshes.

3.2.3 Test Problems with Heterogeneity

Gross et al. (2019) proposed a series of four simple test cases of increasing complexity to compare the meshing capability of Vorocrust with that of other meshing software such as LaGriT (Los Alamos Grid Toolbox, Los Alamos National Laboratory, <https://lagrit.lanl.gov>) and Cubit (Owen et al, 2019a, Owen et al, 2019b). Each test case represents a common geologic feature; layered units, a pinch-out, offset units, and a lens. For this work, the four test cases are meshed with unstructured hexahedral meshes generated using Cubit and Vorocrust-generated Voronoi meshes. PFLOTRAN simulations are run on the Voronoi meshes for all four cases, and the hexahedral meshes for three cases.

In parallel work, Gross et al. (2019) generated Voronoi meshes for each of the four test cases using LaGrit. Because LaGrit uses a different method (Delaunay triangulation) to create Voronoi cells than Vorocrust, the two generate dissimilar grids. The meshes generated with LaGrit were used for simulations in PFLOTRAN and FEHM.

3.2.3.1 Test Case 1: Layered System

The first test problem is a simple layered model with four layers. There is a contrast in material properties between the layers, but each layer is homogeneous internally. Side views of the simulation meshes are shown in Figure 3-5. The material properties are in Table 3-1 and the initial

and boundary conditions are shown in Table 3-2. PFLOTRAN's TH mode is used to simulate variably-saturated single-phase flow (using Richards equation) coupled with heat transport on one Voronoi cell mesh and two regular hexahedral meshes, one with 10,000 cubic elements, and one with 90,000 cubic elements.

The simulated temperature and liquid saturation on the 10,000-cell hexahedral mesh after 0.1 years of simulation time are shown in Figure 3-6; the current workflow does not generate the output necessary to make 3D figures of simulation results on VoroCrust meshes. The temperature and saturation profiles at three interior observation points are shown in Figure 3-7. Simulations on the Voronoi mesh and two hexahedral meshes are shown. All connections in the hexahedral meshes are orthogonal for this test case, so simulations on the hexahedral meshes will converge to accurate temperature and saturation profiles with sufficient grid refinement. The 90,000-cell hexahedral mesh simulation is used as a benchmark.

At observation points M1 and M4, the Voronoi mesh simulation results are in better agreement with the 90,000-cell benchmark simulation results than the 10,000-cell mesh, as can be seen in Figure 3-7. All meshes have identical results for the diffusive temperature profile at M1 and M4, while the liquid saturation is always slightly underestimated in the coarser meshes.

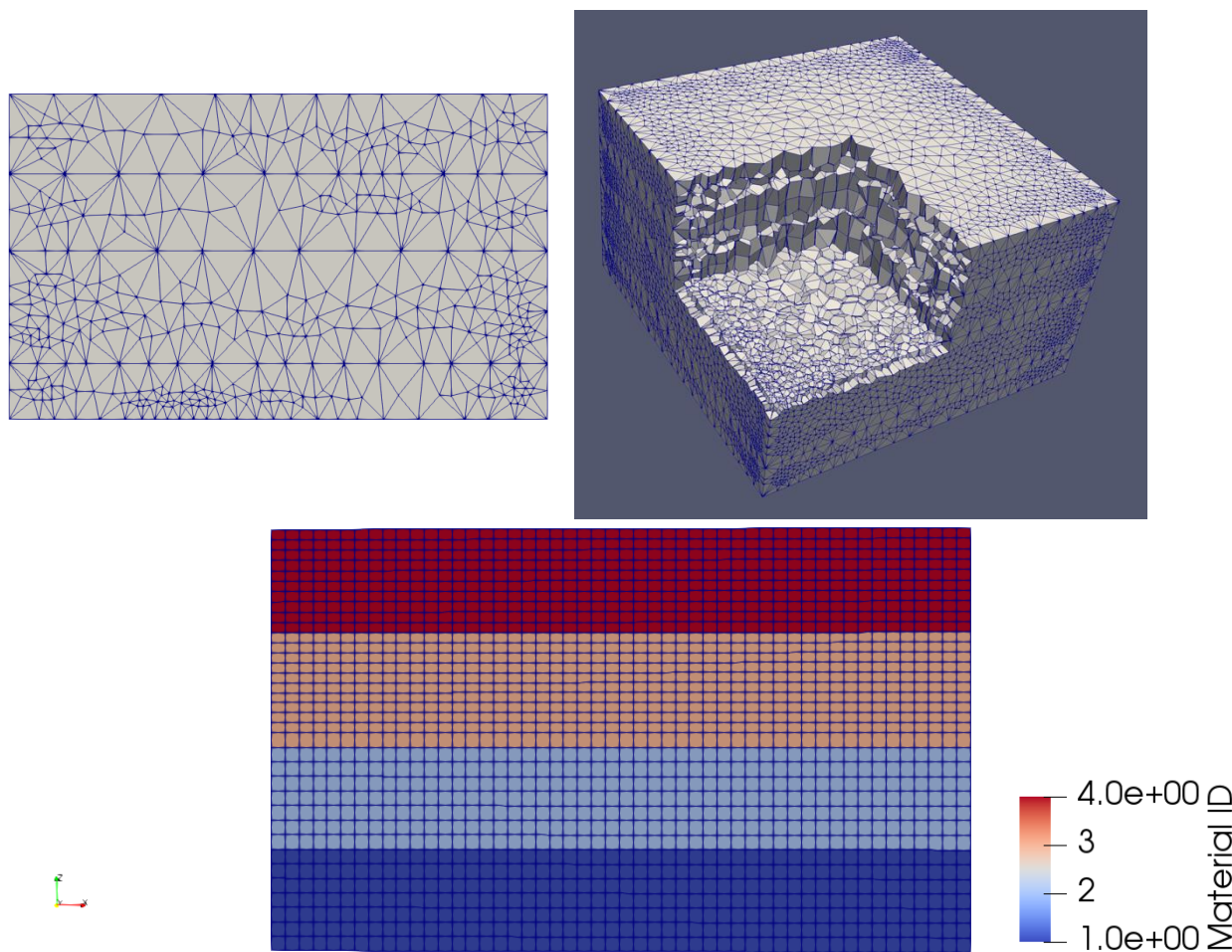


Figure 3-5. Simulation meshes for Test Case 1. Top: Voronoi mesh with 11,005 grid cells. Bottom: Hexahedral benchmark mesh with 10,000 grid cells showing Material ID assignments.

Table 3-1. Material properties for Test Case 1. Material IDs are assigned as shown in Figure 3-5.

	Layer 1	Layer 2	Layer 3	Layer 4
Porosity (ϕ)	0.01	0.02	0.03	0.04
Tortuosity	1.0	1.0	1.0	1.0
Rock Density (kg/m ³)	2800	2900	3000	3100
Specific Heat (J/Kg·K)	1.0	1.5	2.0	2.5
Thermal Conductivity (W/K·m)	0.1	3.0	0.05	6.0
Permeability (In all directions) (m ²)	1×10^{-9}	1×10^{-14}	1×10^{-11}	1×10^{-14}

The Voronoi mesh result at observation point M3 has consistently lower temperature and pressure than the benchmark. The temperature profile is not as close to the benchmark simulation as the hexahedral mesh with 10,000 grid cells, while the pressure profile is the same as the 10,000-cell simulation at short time and then gets very close to the 90,000-cell benchmark. The error is small, and it is not clear if part of the problem is the challenge of choosing observation points that are the same across all the meshes. Running simulations on a more refined Voronoi mesh for additional validation is recommended.

Table 3-2. Initial and boundary conditions for Test Case 1.

	Initial	Recharge	Release
Region Assigned	All	West Face (small x boundary)	East Face (large x boundary)
Temperature (C)	5.0	90.0	1.0
Pressure (Pa)	100300	100300	1000
Liquid Flux (cm/min)	N/A	1.0	N/A

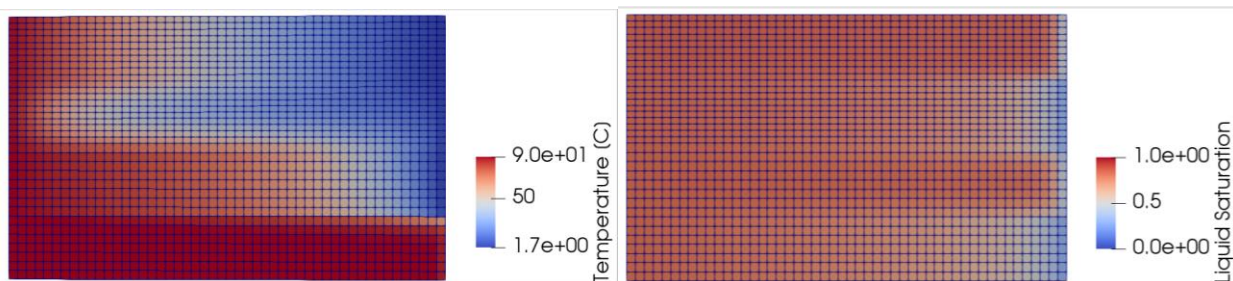


Figure 3-6. Temperature (left) and liquid saturation (right) for Test Case 1 after 0.1 years of simulation.

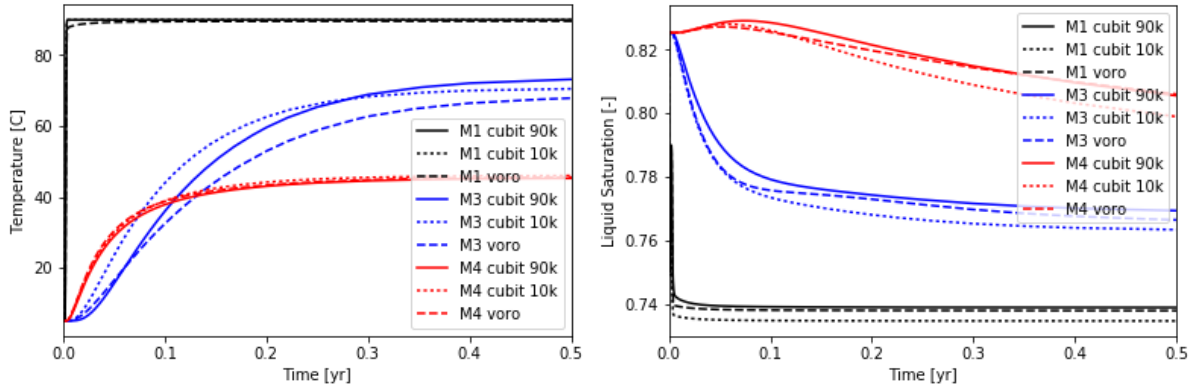


Figure 3-7. Profiles of temperature (left) and liquid saturation (right) for three observation points in Test Case 1. Two simulations on hexahedral meshes are shown along with the simulation on the Voronoi mesh. M1 is in Material 1, M3 is in Material 3 and M4 is in Material 4.

3.2.3.2 Test Case 2: Pinch Out

The second test case contains three materials which intersect at a point where Material 2 pinches out. The simulation meshes and material domains are shown in Figure 3-8, the material properties are in Table 3-3, while the initial and boundary conditions are in Table 3-4. The Voronoi mesh has 8,541 cells, while the coarse and fine hexahedral meshes have 8,600 cells and 78,000 cells, respectively.

In this test case the hexahedral mesh is flexed to the boundary between the materials, it is no longer orthogonal and not a rigorous benchmark simulation. However, as the mesh is highly refined and most of the flow is around (not through) the highly flexed cells near the pinch-out of Material 2, the 78,000-cell simulation still serves as a good comparative simulation for the Voronoi mesh.

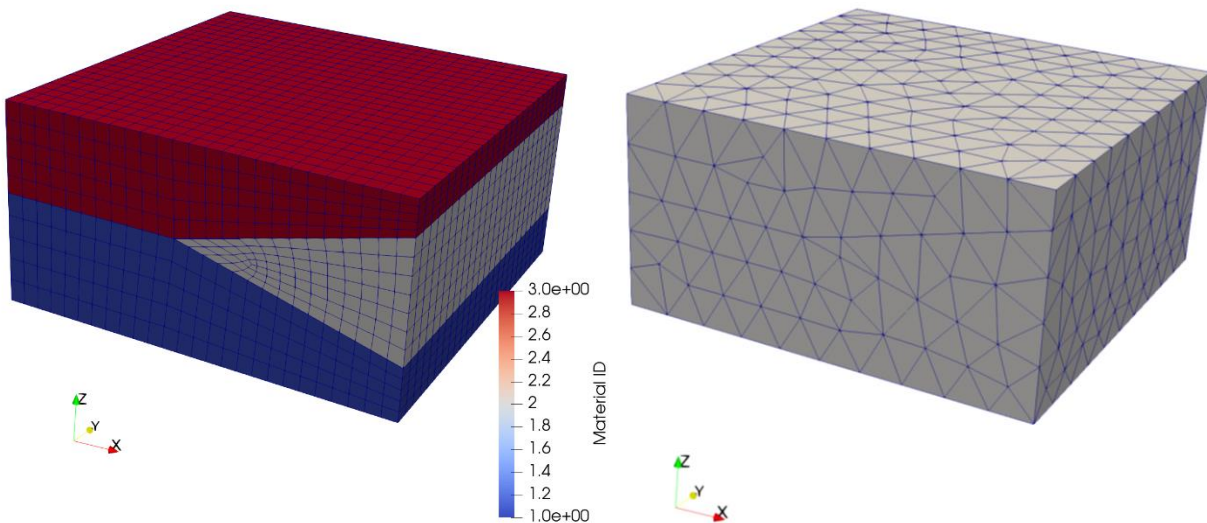


Figure 3-8. Coarse hexahedral (left) and Voronoi (right) meshes for Test Case 2 which has Material 2 pinching out in the interior of the domain.

Table 3-3. Material properties for Test Case 2. Material IDs are assigned as shown in Figure 3-8.

	Material 1	Material 2	Material 3
Porosity (ϕ)	0.01	0.01	0.01
Tortuosity	1.0	1.0	1.0
Rock Density (kg/m ³)	2800	2800	2800
Specific Heat (J/Kg-K)	1.0	1.0	1.0
Thermal Conductivity (W/K-m)	1.0	0.01	50
Permeability (In all directions) (m ²)	1×10^{-7}	1×10^{-11}	1×10^{-9}

Table 3-4. Initial and boundary conditions for Test Case 2.

	Initial	Infiltration	Release
Pressure (Pa)	100000	100000	5000
Temperature (°C)	5.0	90.0	10.0
Liquid Flux (cm/min)	N/A	1.0	N/A
Region Assigned	All	Top Face	Bottom Face

Figure 3-9 shows the simulated temperature and pressure on the coarser hexahedral mesh after one hour of simulated time. The thermal conductivity and permeability of Material 2 have deliberately been chosen to be very low (see Table 3-4) forcing both the fluid and thermal front to travel between Materials 1 and 3 around the wedge-shaped region. Though unrealistic, this serves as a challenging simulation for this test case.

A comparison of the saturation and temperature profiles at observation points in each of the materials is shown in Figure 3-10. The Voronoi mesh results are very similar to the refined hexahedral mesh at points M2a and M3, while at M1 both profiles are quite different. This is likely because the observation point in the Voronoi mesh is closer to the interface between Materials 1 and 3, and saturation decreases and temperature increases earlier at this location.

Finding suitable interior observation points between meshes is not always a simple task when comparing across unstructured meshes. In the present work, all observation points are chosen to be the seed of a cell in the Voronoi mesh near the center of a material domain, so observation points are captured exactly in the Voronoi mesh simulations. The coordinates of these points are input to PFLOTTRAN simulations on the other meshes. PFLOTTRAN chooses the cell center within the same cell as the input coordinates as the observation point; a difference in solution corresponding to the difference in location is expected. For example, at point M2a it was not possible to get a good match to the Voronoi cell seed on the 8,600-cell hexahedral mesh. In Figure 3-10 temperature and liquid saturation at the two vertically-adjacent cells nearest M2a are plotted instead.

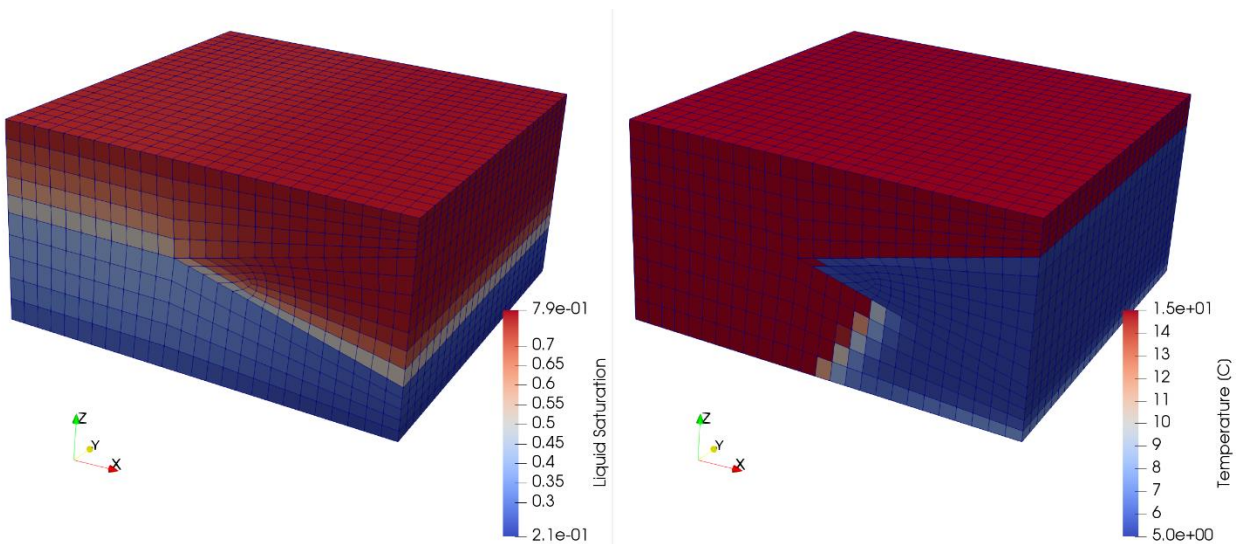


Figure 3-9. Simulated liquid saturation (left) and temperature (right) on the coarse hexahedral mesh on Test Case 2 at 1 hour.

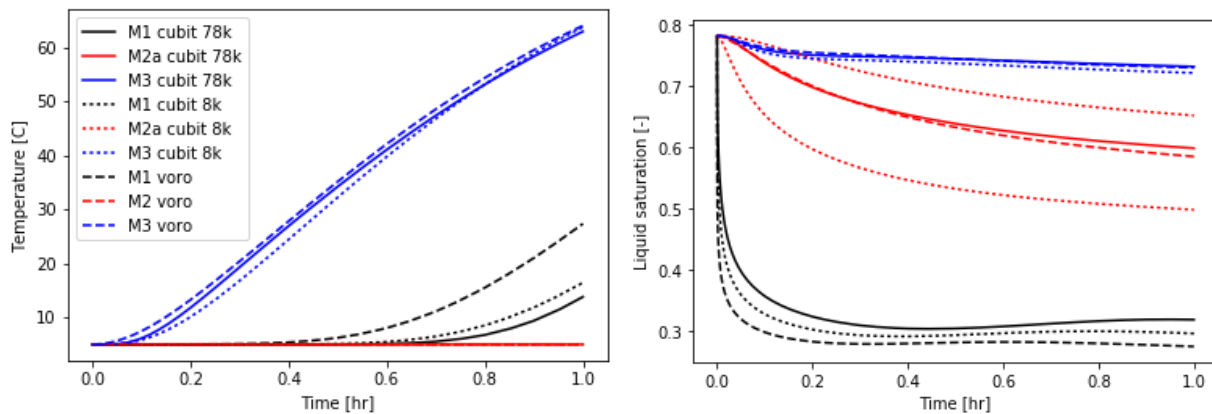


Figure 3-10. Simulated temperature (left) and saturation (right) versus time at three observation points for Test Case 2. M1 is centrally located in Material 1. M2a is centrally located in Material 2 and M3 is centrally located in Material 3.

3.2.3.3 Test Case 3: Interior Lens

The third test case is an interior lens that pinches out to zero height on all sides. This feature is entirely in the interior of the model domain. Figure 3-11 shows the surface Voronoi mesh for Test Case 3, while Figure 3-12 shows the hexahedral mesh for this model. In Figure 3-12 slices of the hexahedral mesh model are cut away to show the interior lens, which is assigned Material 2, while the rest of the domain is Material 1. The hexahedral mesh for this case has 511,000 cells and contains a number of distorted hexahedrons due to the difficulty in capturing the pinch-out of the lens in all directions using only hexahedrons. In contrast the Voronoi mesh of this model is just 22,000 elements.

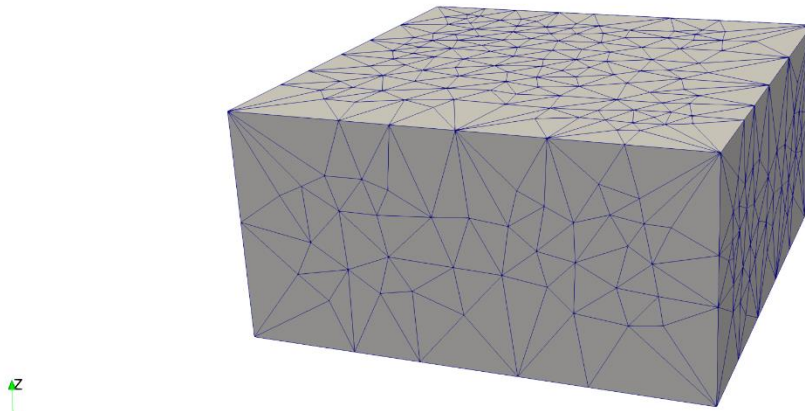


Figure 3-11. Voronoi surface mesh for Test Case 3. This mesh has approximately 22,000 elements.

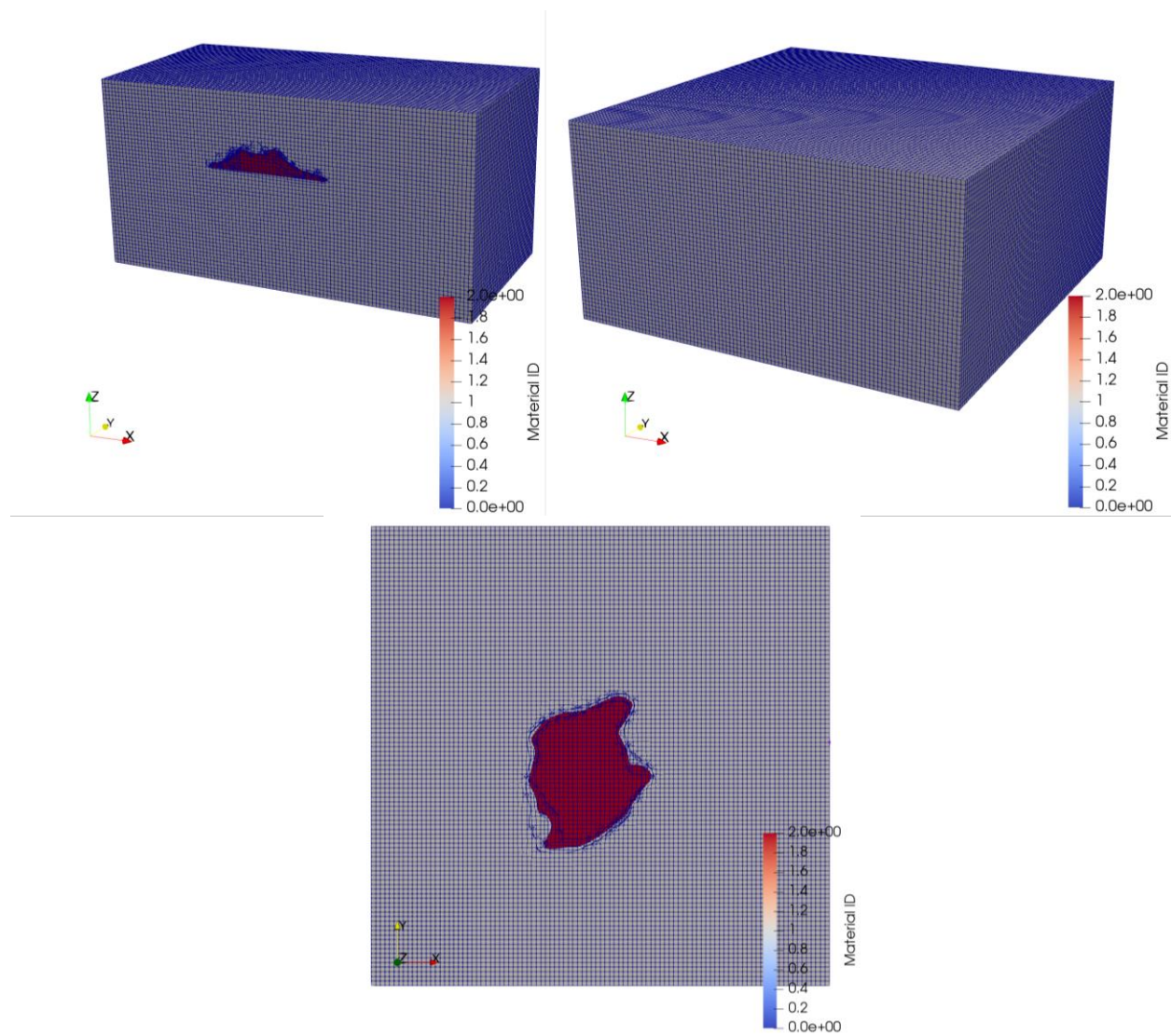


Figure 3-12. Hexahedral mesh of Test Case 3. Top left: XZ slice through the center of the domain to show the interior lens. Top right: the surface mesh of this model is all orthogonal hexahedral elements. Bottom: XY slice through the lens. This mesh has over half a million elements.

There is currently no easy way to assign a different material type to the lens on the Voronoi mesh. In the other test cases on Voronoi meshes each material is mapped to a region internally in PFLOTRAN by defining polygons in space. As the lens shape is highly irregular this method will not work for Test Case 3. PFLOTRAN also accepts region assignment by the ID numbers of the cells in each region, which is how materials are assigned on all the hexahedral meshes for the test cases. In the future VoroCrust will provide this information in an output file accompanying the simulation mesh.

Though it is not possible to populate the lens feature in the Voronoi mesh with a separate material type, a simulation is run to demonstrate that it is a suitable simulation mesh. In this simulation the cube from $(x, y, z) = (7.4, 7.4, -3.5)$ to $(10.6, 10.6, -4.0)$ inside the lens has a source term in it with an injection rate of $10 \text{ m}^3/\text{day}$ for one day, until the saturation in the observation cells begins to reach quasi-steady state. The entire domain is Material 1 from Test Case 2, with the properties shown in Table 3-3. All four side boundaries are open, but the top and bottom are sealed. Observation points are located 4 m from each boundary at a depth of $z = -4 \text{ m}$ directly north, south, east and west of the center of the model.

The saturation and pressure profiles at the observation points are shown in Figure 3-13. As expected, the pressure and saturation increase most rapidly at the southern observation point, as it is closest to the injection region, and more slowly at the northern observation point, as it is furthest from the injection region. This simulation demonstrates that the Voronoi mesh is functional; no comparison can be made because no simulation was run on the hexahedral mesh.

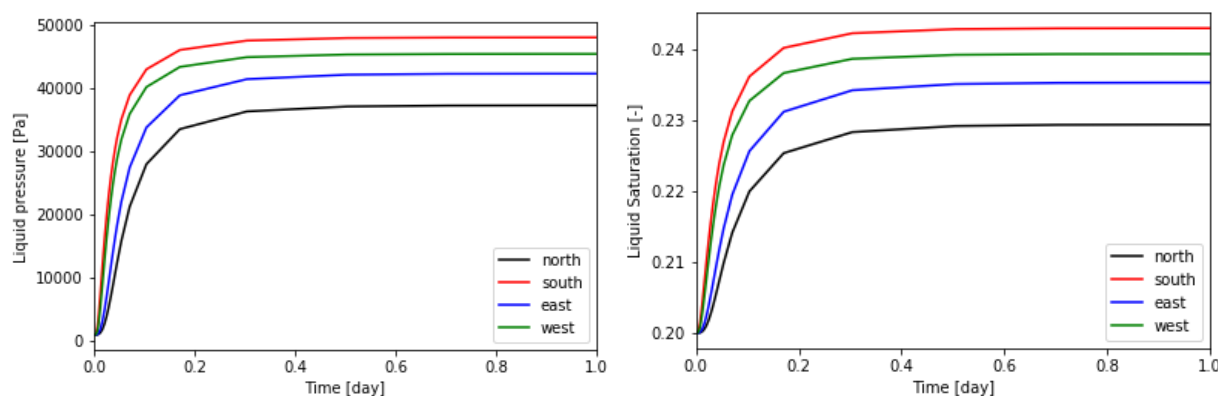


Figure 3-13. Simulated pressure (left) and saturation (right) profiles at the four observation points for Test Case 3. Observation points are all in the plane of the lens at a depth of $z = -4 \text{ m}$.

3.2.3.4 Test Case 4: Faulted Layers

The fourth test case contains three material layers which are offset across a fault that passes through the model at an angle. Two of the simulation meshes and the material domains are shown in Figure 3-14, the material properties are in Table 3-5, while the initial and boundary conditions are in Table 3-6. The Voronoi mesh has 10,813 cells, while the coarse and fine hexahedral meshes have 4,180 cells and 66,000 cells, respectively. As in Test Case 2, the hexahedral meshes of this model are flexed to the model features and non-orthogonal and so they are not a rigorous benchmark of the simulation on the Voronoi mesh.

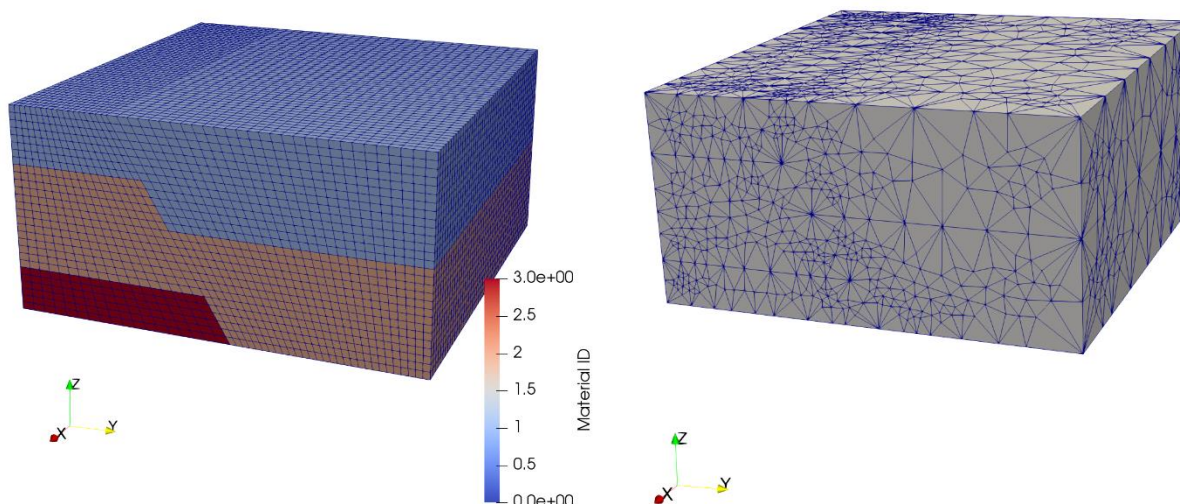


Figure 3-14. Hexahedral (left) and Voronoi (right) meshes for Test Case 4 which has an offset fault through the interior of the domain.

Table 3-5. Material properties for Test Case 4. Material IDs are assigned as shown in Figure 3-14.

	Material 1	Material 2	Material 3
Porosity (ϕ)	0.01	0.01	0.01
Tortuosity	1.0	1.0	1.0
Rock Density (kg/m ³)	2800	2800	2800
Specific Heat (J/kg·K)	500.0	500.0	500.
Thermal Conductivity (W/K·m)	0.0001	1000.0	0.001
Permeability (In all directions) (m ²)	1×10^{-9}	1×10^{-11}	1×10^{-8}

Table 3-6. Initial and boundary conditions for Test Case 4.

	Initial	Infiltration	Release
Pressure (Pa)	1000	100000	1000
Temperature (°C)	5.0	25.0	5.0
Liquid Flux (cm/min)	N/A	1.0	N/A
Region Assigned	All	Top Face	Bottom Face

The thermal conductivity of Material 2 is chosen to be very high, while the permeability of this domain is orders of magnitude lower than the other materials. Though unrealistic, this was chosen so that the temperature would rapidly propagate across Material 2, but the infiltrating water will preferentially flow into Materials 1 and 3. This is shown on a snapshot of the saturation and temperature on the 66,000-cell hexahedral mesh in Figure 3-15.

Temperature and saturation as functions of time for all three simulations at four observation points in the domain are shown on Figure 3-16. The temperature never changes at M1 or M3 due to the very low thermal conductivity of these materials, while saturation at M2 RT on the right side of Material 2 never changes due to the low permeability of that material. As can be seen in Figure 3-16, the conduction-dominated thermal profiles at all of the observation points are well-modeled by the Voronoi mesh and both of the flexed hexahedral meshes. The refined hexahedral mesh predicts a later increase in water saturation than the other two models at M1 and M2 LT. This could be because of changes to the location of the observation points, or because of the coarse grid refinement in the Voronoi and coarse hexahedral mesh.

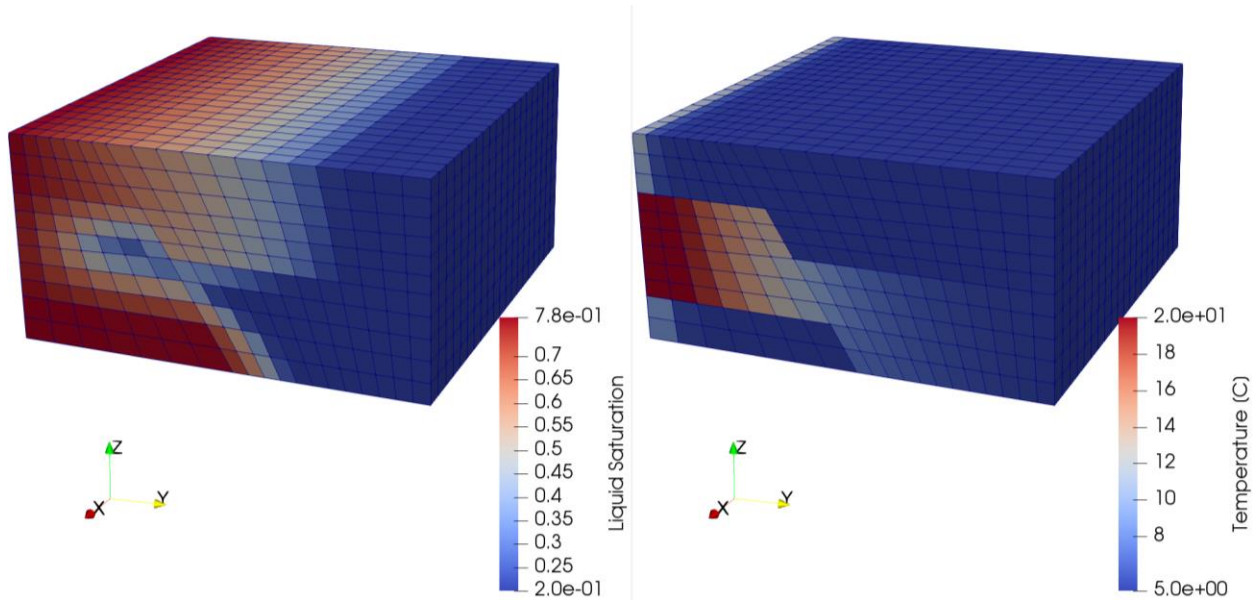


Figure 3-15. Simulated liquid saturation (left) and temperature (right) on hexahedral mesh on Test Cast 4 after 10 years.

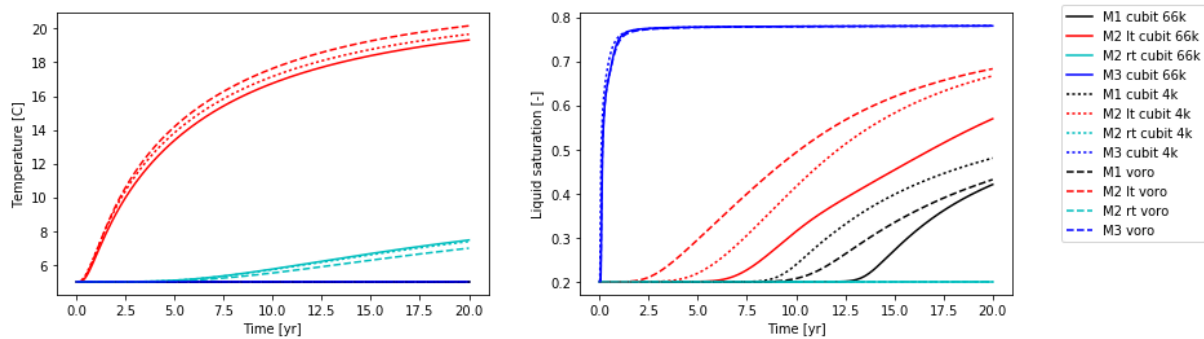


Figure 3-16. Simulated temperature (left) and saturation (right) versus time at four observation points for Test Case 4. M1 is centrally located in Material 1. M2 LT is in Material 2 to the left of the fault, M2 RT is in Material 2 to the right of the fault, and M3 is centrally located in Material 3. Simulations for a coarse and refined hexahedral mesh are shown as well as the results on the Voronoi mesh.

3.2.4 Conclusions and Future Work

Five example cases have been meshed with Voronoi meshes: the unit cube, layered model, pinch-out, interior lens, and fault. Voronoi meshes of all five models have been successfully used for PFLOTRAN simulations and four of them were compared with simulations on hexahedral meshes with similar and higher resolution. These results verify that solutions obtained on Voronoi meshes agree with solutions obtained on other meshes for models of increasing complexity. The longer-term goal is to create Voronoi meshes of subsurface geologic and engineered features with VoroCrust and use them for repository simulations in PFLOTRAN. Additional code development and testing is necessary as outlined in the following subsections.

3.2.4.1 PFLOTRAN Simulation Testing

To do a thorough simulation validation of Voronoi meshes for use in PFLOTRAN, additional simulation work should be done:

- Finer Voronoi meshes of Test Cases 1 to 4 have been generated using VoroCrust but have not been used in PFLOTRAN simulations yet. Simulations identical to the ones in the preceding sections should be run on them and compared against simulated results on the coarse Voronoi meshes, the hexahedral meshes and other unstructured meshes such as tetrahedral elements.
- All tests so far have been conducted in PFLOTRAN's TH mode and without transport. It would be useful to compare solutions and computation times on problems run using PFLOTRAN's GENERAL mode, which simulates two-phase miscible flow coupled to energy transport. Reactive transport simulations may also present unique grid discretization requirements.
- Voronoi meshes of increasingly complex features could be built and simulations on these compared to simulations on hexahedral meshes.

3.2.4.2 VoroCrust/PFLOTRAN Interface Developments

Two main features should be added to the VoroCrust/PFLOTRAN interface:

- The first is two- and three-dimensional visualization of simulation results on VoroCrust meshes. The current workflow does not output enough mesh information to populate 3D diagrams of PFLOTRAN simulation results in meshing software such as ParaView (<https://www.paraview.org/>).
- The second is to have VoroCrust generate output files indicating which cells belong to which region in the models. As discussed in the section on Test Case 3, currently PFLOTRAN can only define materials on relatively simple geometric shapes unless that information is provided cell-by-cell from an external source, such as the meshing software.

3.2.4.3 VoroCrust Development: Anisotropic Meshing

In the future it will be important to be able to mesh to highly anisotropic features that are common in the subsurface. A VoroCrust mesh of the next proposed test case is shown in Figure 3-17. PFLOTRAN simulations can be run on this problem once material ID marking is available from VoroCrust. This mesh has 85,000 grid cells and is able to capture even the thinnest part of all seven layers accurately. The trade-off is that cells become extremely small in all directions in these thin

regions, which can result in prohibitively large numbers of cells for complex models. Similar issues were encountered in creating a hexahedral mesh of the shale GFM in Section 5.1.1.3. Future development of anisotropic meshing capability in VoroCrust will allow thin regions to be meshed with cells that are longer in the x - and y -directions than in the z -direction.

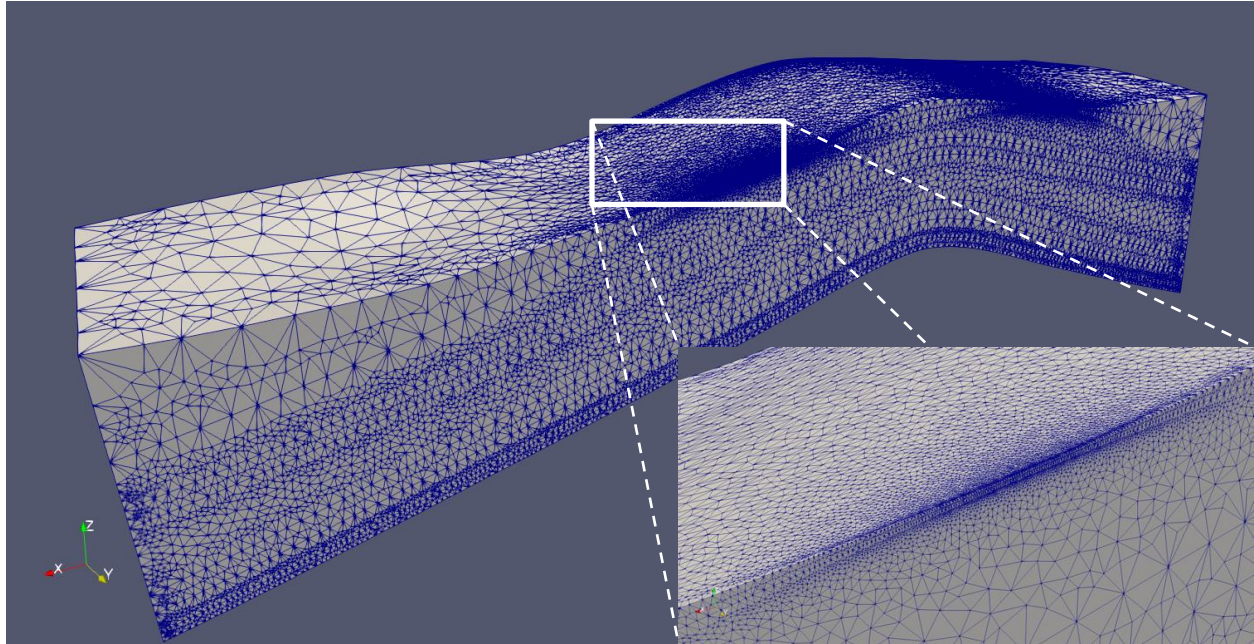


Figure 3-17. Voronoi mesh of a highly anisotropic geologic model with seven layers of varying thickness. The detail section shows that the mesh is able to capture thin layers exactly, but at the cost of very small grid cells.

4 GENERIC UNSATURATED ZONE REFERENCE CASE

In the second half of FY2019 there have been two parallel efforts on the alluvium reference case. The first has focused on improving computational methods for this challenging conceptual model and assessing the quality of simulated results. The second is development of a new geologic framework model (GFM) (Gross et al, 2019). Progress in the former effort is described here in Section 4.1, while the latter is briefly described in Section 4.4.

4.1 Post-Closure Repository Modelling

The conceptual model for a repository in unsaturated alluvium was developed by Sevougian et al. (2019b) and Mariner et al. (2018). The unsaturated zone repository is assumed to be 250 m below surface level in a high-permeability part of the alluvium formation. The advantage of putting the repository in this part of the formation is lower initial saturation which results in less steam generation when waste packages with high heat load are emplaced. The high permeability allows for the steam to escape more easily, preventing build-up of pressure in the repository in the first decades after closure. This was discussed in more detail in Sevougian et al. (2019b). All simulation parameters are identical to those used in simulations of 24-PWR waste packages 100-year OoR in the alluvium reference case in Sevougian et al. (2019b) and shown in Table 4.7 of that work.

Simulation of the unsaturated zone is numerically difficult due to rapid increase in temperature in the first few decades post-closure. To achieve numerical stability, simulation timestep size is limited by the Courant-Friedrich-Lewy (CFL) condition, which states that flowing fluids can traverse at most a single grid cell in a single timestep. Timestep size is limited by the rate at which the steam front propagates away from the hot waste packages, especially for single phase gas states. The cells around the waste packages are refined to as small as 1.67 m and the steam front expands rapidly, requiring very small timesteps during the first few hundred years of the simulations. If the simulator attempts to take timesteps that are too large, the solution may diverge, which will cause the simulation to stop. This limitation on timestep size is intrinsic to the physics of the problem but the time to converge at each timestep is solver-dependent. Some numerical solvers handle discontinuities and nonlinearities better than other, but this is still an active area of research in computational sciences from which GDSA can benefit.

4.1.1 Code Development

A new solver for the nonlinear system called the Newton trust region (TR) method has been implemented into PFLOTRAN (Mariner et al., 2019; Conn et al. 2000). The TR algorithm has not yet been fully tested in PFLOTRAN but, based on research in FY19, it appears to converge much more quickly than the default Newton's method for challenging multiphase problems. The TR algorithm is benchmarked against the Newton's method using the site-scale (multi-drift) UZ simulations in the sections below.

Two additional options have been made in PFLOTRAN to improve simulations of the UZ case (see Section 3.1). The first is to have water mole fraction in the gas phase as the independent variable when only the gas phase is present in a grid cell, rather than the default air mole fraction. When steam is rapidly generated, the cells near the waste packages dry out and the gas phase becomes almost entirely steam. Using air mole fraction as the independent variable means the solver has to operate on very small numbers, which may contribute to problems with convergence.

The other option added was an alternative pressure governor that limits timestep size based on only the gas-phase pressure in the two-phase region. During dry-out the liquid pressure, which is equal to gas pressure minus capillary pressure, steeply drops to large negative values as the residual liquid saturation is approached. By limiting timestep based only on gas pressure the solver is able to take larger timesteps during this process.

4.2 Site-scale Models

In this section, results of simulations conducted on a series of meshes with varying discretization are compared. The purpose of this modelling exercise is to test the robustness and speed of the Newton TR solver on numerical meshes of different resolution and to compare the results among the meshes, where appropriate, e.g., to compare temperatures and gas saturations at certain spatial locations of the simulation domains.

The geometry of this model is identical to the model in Sections 4.3.2.2 and 4.4.2.1 of Sevougian et al. (2019b) except that there is no east to west hydraulic gradient. The model domain has 25 waste packages per drift in 27 drifts. Drift spacing is 50 m, and center-to-center spacing of packages along the drift is 20 m. The model has a no-flow boundary condition at the south face, which acts as a reflector, so the total number of waste packages represented in the model is 1350. Heat sources representative of 24-PWR waste packages 100-year OoR are used. The repository layout, material properties, and heat source terms are identical to those used in Sevougian et al. (2019b).

Four meshes of varying grid resolution have been built for the UZ model:

1. **Fully-resolved mesh (Mesh 1).** This mesh resolves the waste packages, backfilled drifts, shafts and halls, the disturbed rock zone (DRZ), and the surrounding alluvium formation. This model has two levels of local grid refinement, resulting in some non-orthogonal cells around the drifts and around the repository. It has 2.4 million grid cells. (See top left of Figures 4-1, 4-2, and 4-3.)
2. **Mesh that resolves waste packages (Mesh 2).** This mesh resolves each waste package as a single grid cell and includes drifts and the surrounding halls. The shafts and the DRZ are not in this model. This model has flexing in the mesh and one level of local grid refinement, resulting in non-orthogonal cells around and above the repository. It has 215,000 grid cells. (See top right of Figures 4-1, 4-2, and 4-3.)
3. **Mesh that resolves drifts (Mesh 3).** This mesh resolves each drift as a volume one grid cell wide. Waste packages are not resolved, and the entire drift volume is assigned the material properties of backfill. Each drift grid-cell contains one waste package heat source. This model has flexing in the mesh, resulting in non-orthogonal cells around and above the repository. It has 105,000 grid cells. (See bottom left of Figures 4-1, 4-2, and 4-3.)
4. **Mesh that does not resolve drifts (Mesh 4).** This model has a coarse mesh across the repository so that each grid cell in the repository area contains a single waste package heat source. Two simulations are run on this mesh, one with backfill material throughout the repository and one with alluvium material throughout. The mesh in this model does not contain any flexing or local grid refinement so that all cells are orthogonal. It has 64,000 grid cells. (See bottom right of Figures 4-1, 4-2, and 4-3.)

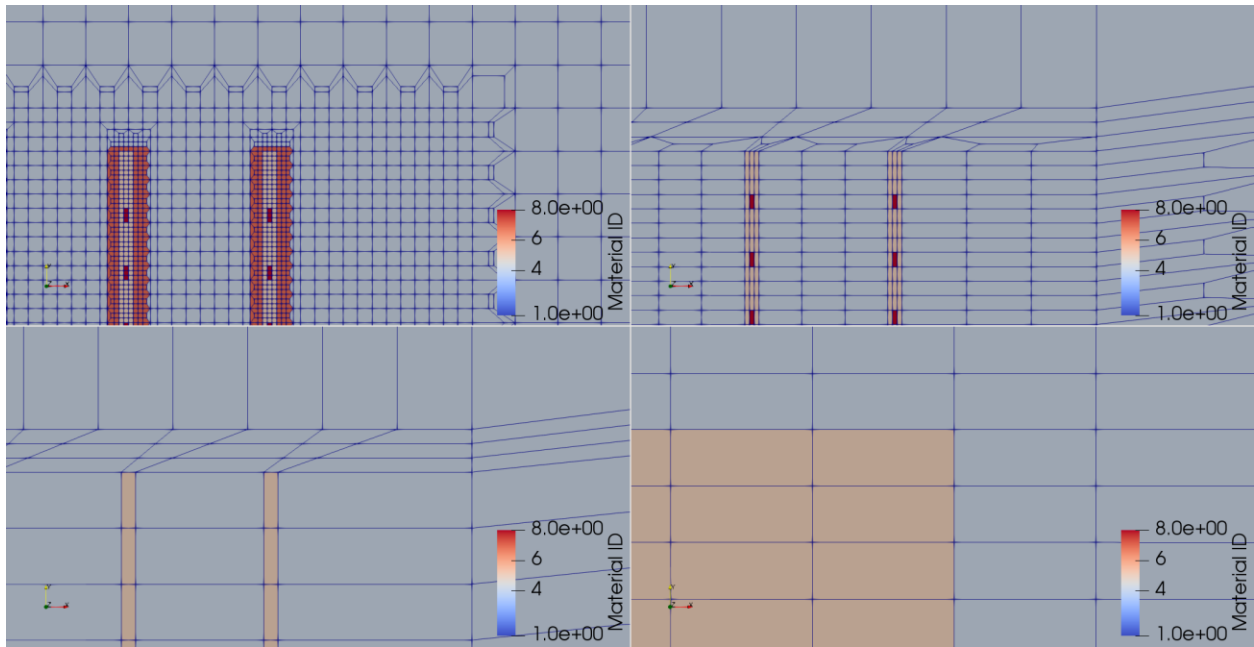


Figure 4-1. Plan view (XY slice) of the northeast corner of the repository in the four meshes of varying grid resolution.

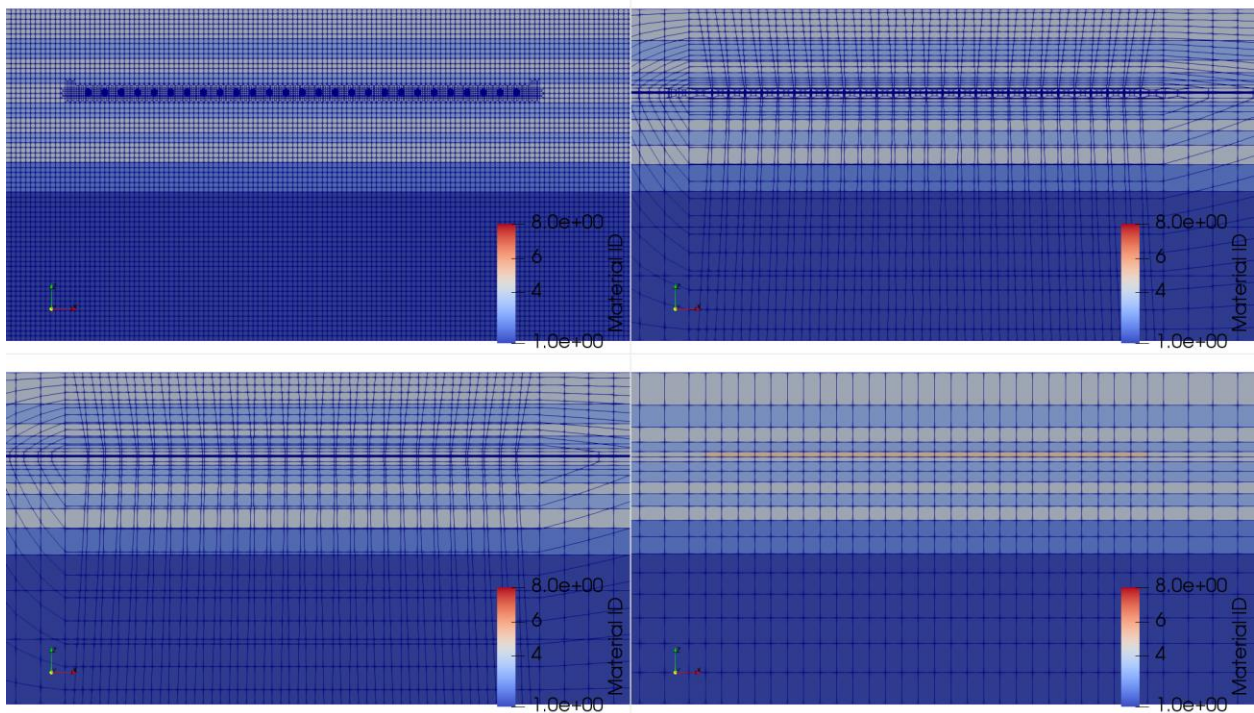


Figure 4-2. Vertical cross-section (XZ slice) through the repository including the repository area and full model depth. All grids preserve stratigraphic features. Four meshes of varying grid resolution are shown.

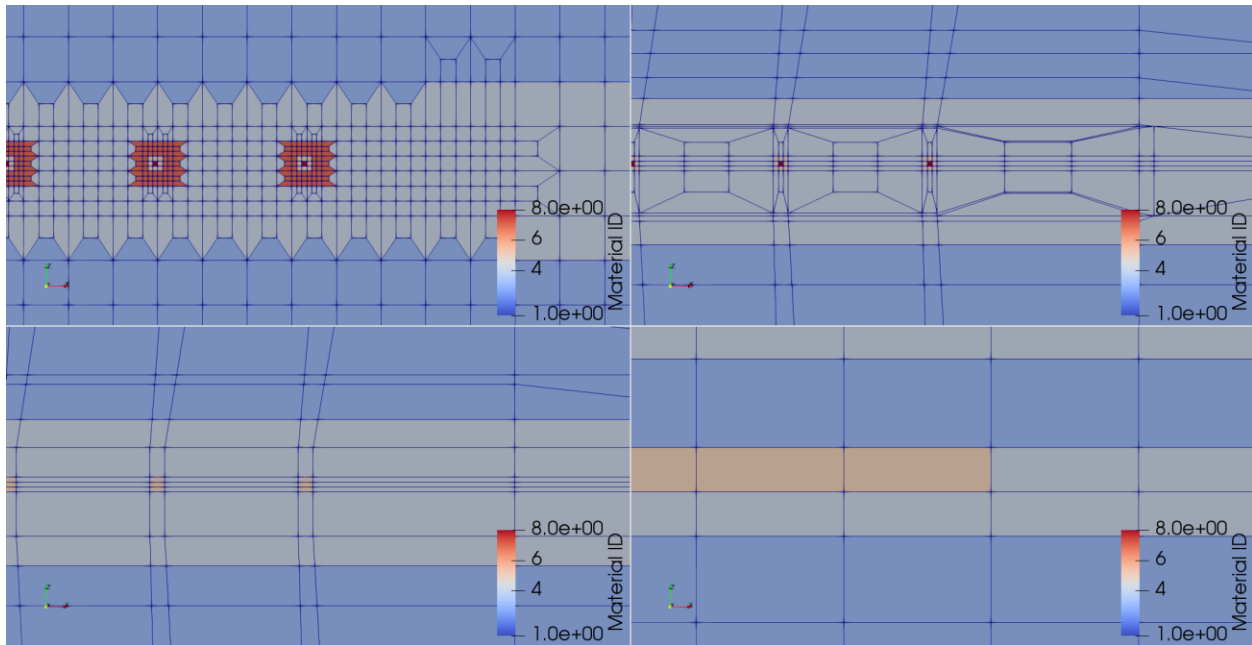


Figure 4-3. Vertical cross-section (XZ slice) through the repository including only the area around the three drifts on the eastern edge of the repository. The four meshes of varying grid resolution are shown.

Legend for Figures 4-1, 4-2, and 4-3: The **fully resolved** mesh (Mesh 1) on the top left of each of the above three figures includes the DRZ (material 7). The **resolved waste packages** mesh (Mesh 2) on the top right resolves the waste packages but does not include the DRZ. The **resolved drifts** mesh (Mesh 3) on the bottom left resolves the drifts, but not individual waste packages. The **all backfill** mesh (Mesh 4) on the bottom right does not resolve drifts or waste packages but has backfill properties throughout the repository. An additional set of simulations, called “**no backfill,**” are conducted on a mesh identical to the all backfill simulation (Mesh 4), but with alluvium rock properties throughout the repository.

4.2.1 A Question of Solvers

The Newton TR solver algorithm in PFLOTRAN is still being tested for stability and accuracy, so the first task in the present study is to validate this new TR solver against the default Newton LS algorithm, which reaches convergence in most settings and is used in simulations of other host-rock concepts (shale, crystalline, bedded salt).

Simulations were run on all four of the meshes using both the TR and LS solvers for up to 1000 years simulation time or 48 hours wall clock time. Simulation results are summarized in Table 4-1. Parameters specifying iteration behavior, timestep growth and limitations, and convergence criteria are identical among all simulations.

Neither solver algorithm completed the 1000-year simulation on the fully-resolved mesh (top left in Figures 4-1, 4-2, and 4-3). The LS algorithm diverged after just over 0.1 year, while the TR algorithm had only progressed 81.7 years of simulation after 48 hours of computation time on 64 cores of a parallel super-computer.

Table 4-1. Simulation time for all four meshes with both the experimental Newton TR and default Newton LS solvers. All simulations are run with identical input options and time stepping routine. Maximum wall clock time was set to 48 hours.

Mesh ID	Simulation name	Simulated time	If simulation did not finish, why not
1	Fully-resolved TR	81.7 yr	Time limit with small timesteps
1	Fully-resolved LS	0.1 yr	Solution diverged
2	Resolved WP TR	1000 yr	–
2	Resolved WP LS	19.3 yr	Linear solver failure
3	Resolved drifts TR	1000 yr	–
3	Resolved drifts LS	349 yr	Time limit with small timesteps
4	All drifts TR	1000 yr	–
4	All drifts LS	1000 yr	–
4	No drifts TR	1000 yr	–
4	No drifts LS	1000 yr	–

For the three coarser meshes (top right, bottom left, and bottom right in Figures 4-1, 4-2, and 4-3), simulation results are shown below in Figure 4-4. The results for the all-backfill and all-alluvium simulations are nearly identical, so only the all-backfill simulation is shown. The TR algorithm is able to simulate all of these meshes for 1000 years, but the LS solver runs only 19.3 years on the resolved waste packages mesh (Mesh 2) and 349 years for the resolved drifts mesh (Mesh 3) before falling into small timesteps and timing-out after 48 hours.

The comparison of gas saturation and temperature in Figure 4-4 shows that for each mesh the TR and LS simulations are identical for nearly all times. The only exception is that the LS algorithm on the model that resolves waste packages shows constant gas saturation around 15 years, while the TR model gas saturation is declining. The LS simulation stops a few years thereafter, likely because of this divergence. The resolved drifts simulations are identical for the 349 years that the LS algorithm runs, and the simulations that do not resolve the repository are indistinguishable throughout the full 1000-year simulations.

The simulations using the TR algorithm are nearly identical to the LS model wherever the LS results are available. Simulation time on the fully-resolved mesh remains prohibitive because the simulation fell into very small timesteps. It is likely that solver or time-stepper options could be fine-tuned to get this simulation to run more quickly.

4.2.2 Site-Scale Model Comparison Across Grid Refinement

In this section, the results of simulations on the four meshes are compared. All simulations are for 24-PWR waste packages and have identical parameters to Table 4-7 in Section 4.3.2 of Sevougian et al.(2019b).

As a result of leaving features out of each model, in some places we expect to see similar results from the simulations while in others we do not expect a similar result. Models that do not resolve the waste package cannot predict waste package temperatures. However, these models may predict saturation, temperature and pressure at some distance away from the waste packages, such as the midpoint between the drifts. Similarly, the models that do not resolve the drifts cannot predict

temperatures, pressures, or saturations within the repository, but may still produce acceptable results above and below the repository.

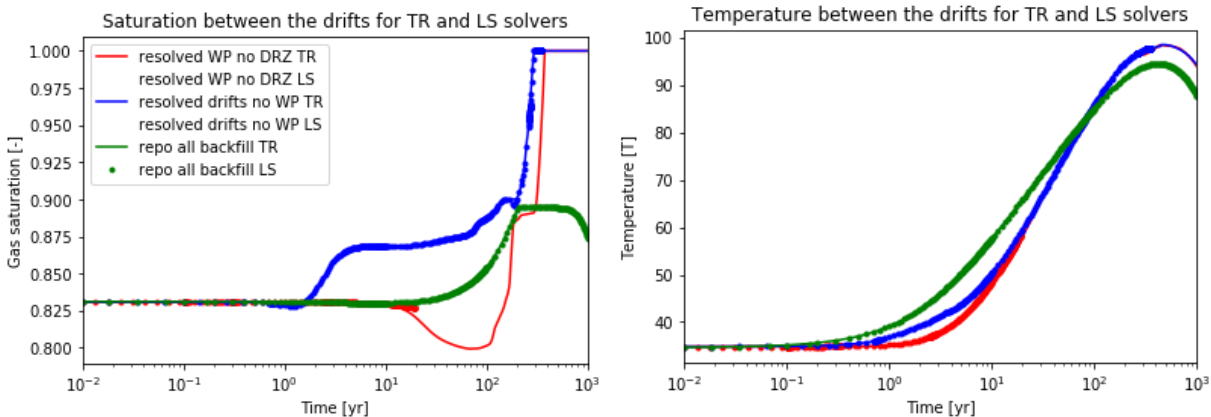


Figure 4-4. Comparison of simulated gas saturation (left) and temperature (right) as a function of the log of time for the TR and LS algorithm for three of the meshes. TR simulations are shown as lines while LS simulations are shown as symbols.

4.2.2.1 Simulation Results on Refined Model

The simulation chosen as the benchmark is that run on Mesh 2, which resolves the individual 24-PWR waste packages but not the DRZ. This simulation was chosen because the simulation on the fully-resolved mesh (Mesh 1) only ran for 82 years. Figure 4-5 shows the temperature and saturation at relevant points near the repository. The top left subfigure shows that the waste packages dry out almost immediately, but the drift between the waste packages dries out over decades. The formation between the drifts does not dry out until 400 years after closure and remains dry for the duration of the simulation. The bottom right picture shows that the regions above and below the repository will never dry out. This indicates that the dried-out region is localized in the repository.

The temperature in the waste packages reaches a maximum temperature of 200°C around 20 years post-closure. The repository between the waste packages does not reach its maximum temperature of 100°C until nearly 400 years post-closure. These results are identical to those observed in Sevougian et al.(2019b) and are discussed in more detail in that work.

4.2.2.2 Simulation Results Across Model Refinement

Figures 4-6, 4-7, and 4-8 show gas saturation in the repository at 20 years (the time of maximum temperature in the waste packages), at 80 years (the final time step for the fully-resolved model), and at 500 years (the time of maximum dry out), for all four simulation meshes. As expected, the propagation of the dry out zone away from the waste packages can clearly be seen in the fully resolved mesh (Mesh 1) and in the mesh that resolves the waste packages (Mesh 2), but not in the two coarser models (Meshes 3 and 4). The dry out zone is propagating more quickly in the y-direction for the mesh that omits the DRZ (Mesh 2) due to the large grid cells in the y-direction.

In the model that resolves the drifts but not the waste packages (Mesh 3), the drifts are almost entirely dry at all of the snapshots in time shown. The mesh that does not resolve the repository (Mesh 4) eventually reaches residual gas saturation of 10%, but never dries out at all.

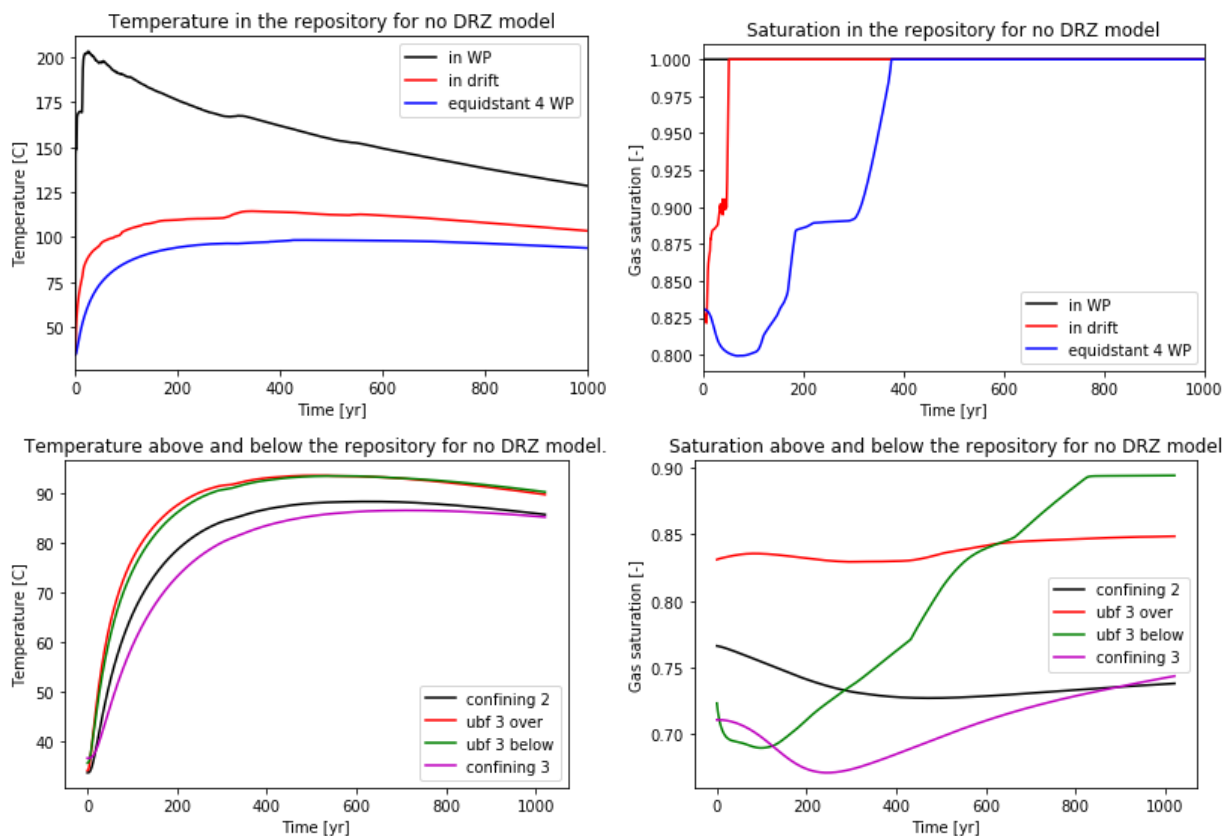


Figure 4-5. Temperature and gas saturation as a function of time for the model that resolves the waste packages but not the DRZ (Mesh 2). Temperature (top left) and gas saturation (top right) in the centermost waste package, between two waste packages in the drift and in the alluvium at the midpoint between four waste packages. Temperature (bottom left) and gas saturation (bottom right) in the formation that contains the repository (ubf 3 over and ubf 3 below—observation points in the upper basin fill just above and beneath the repository horizon) and in the confining beds above (confining 2) and below (confining 3) the repository.

4.2.2.2.1 In the Waste Package

As can be seen in Figure 4-9, all three models that resolve the drifts capture the rapid dry out of the waste packages, while only the two models that resolve the waste packages individually are able to capture the sharp initial increase in temperature. The model that does not resolve the waste packages (Mesh 3) has the heat sources spread over a volume of 500 m³, while the model waste packages are 13.77m³, so the temperature at the center of the heat sources is expected to be underestimated. In all three models the drifts mostly dry out within 50 years, so it makes intuitive sense that all three simulations that resolve the drifts can capture this phenomenon, though dry out is achieved slightly later in the coarsest model (Mesh 3).

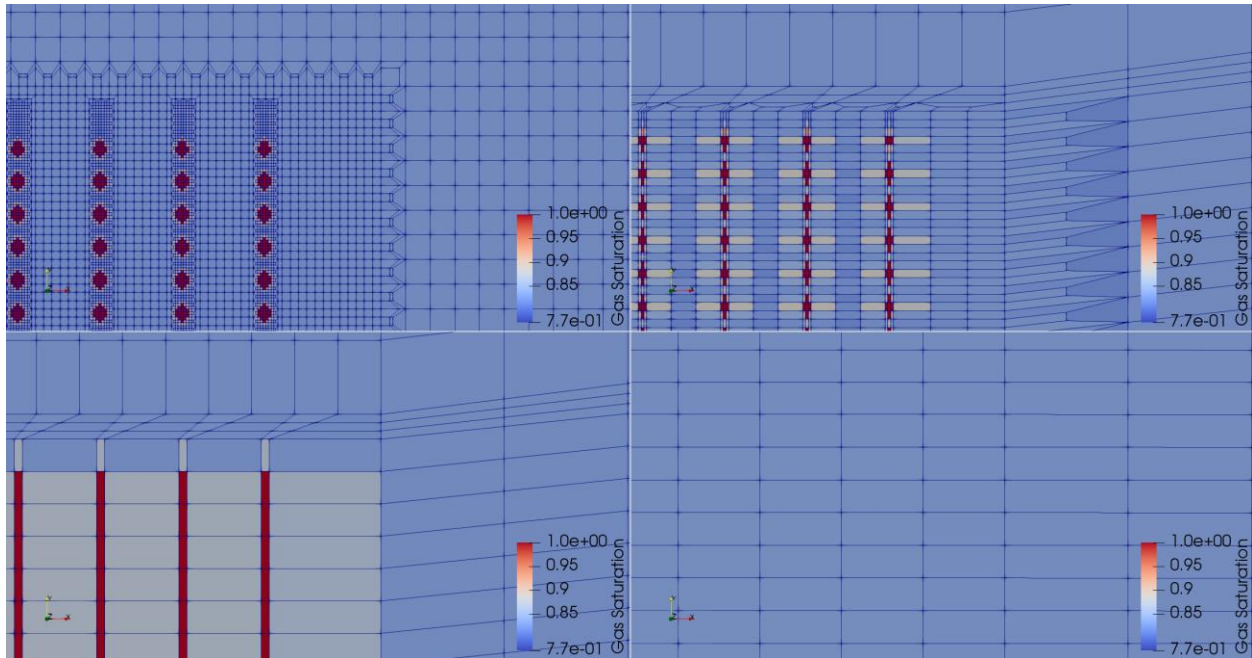


Figure 4-6. Plan view (*XY* slice) of saturation in the north east corner of the repository at time $t = 20$ yr. This is near time of the maximum temperature in the waste packages for the refined simulations. Top left (Mesh 1): fully resolved simulation. Top right (Mesh 2): simulation that resolves waste packages but not the DRZ. Bottom left (Mesh 3): simulation that resolves drifts but not waste packages. Bottom right (Mesh 4): Simulation that does not resolve the repository and has backfill throughout the repository area.

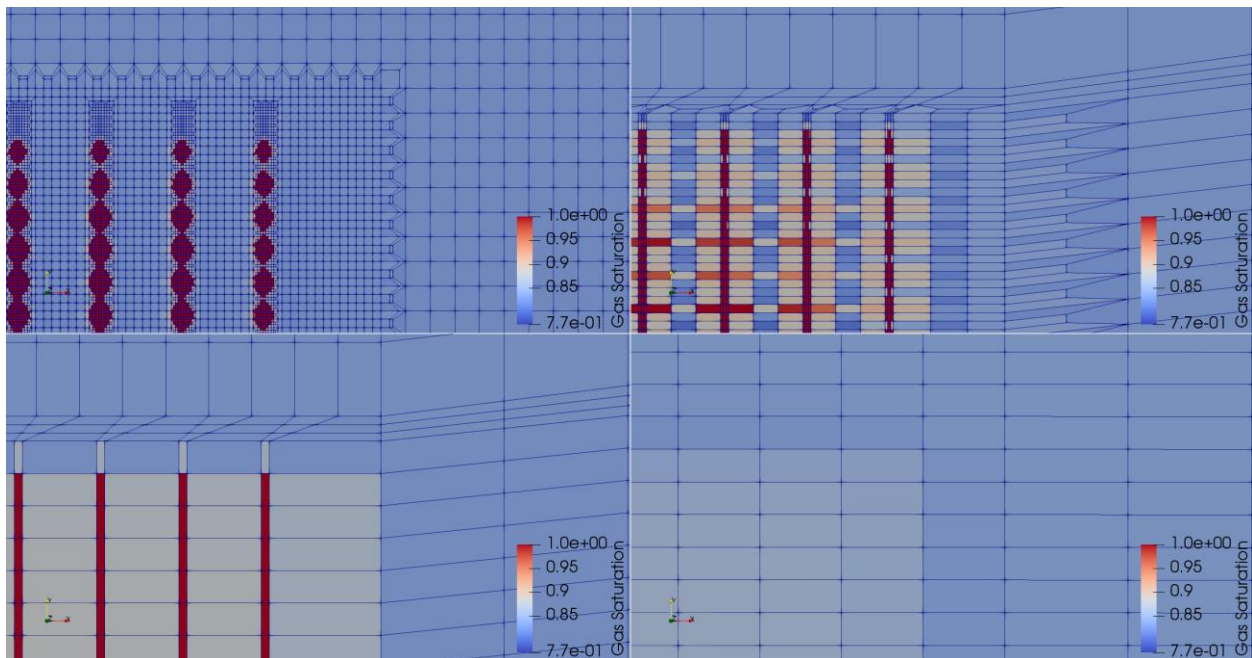


Figure 4-7. Plan view (*XY* slice) of saturation in the north east corner of the repository at time $t = 80$ yr. This is the final snapshot of the simulation on the fully-resolved mesh. Top left (Mesh 1): fully resolved simulation. Top right (Mesh 2): simulation that resolves waste packages but not the DRZ. Bottom left (Mesh 3): simulation that resolves drifts but not waste packages. Bottom right (Mesh 4): Simulation that does not resolve the repository and has backfill throughout the repository area.

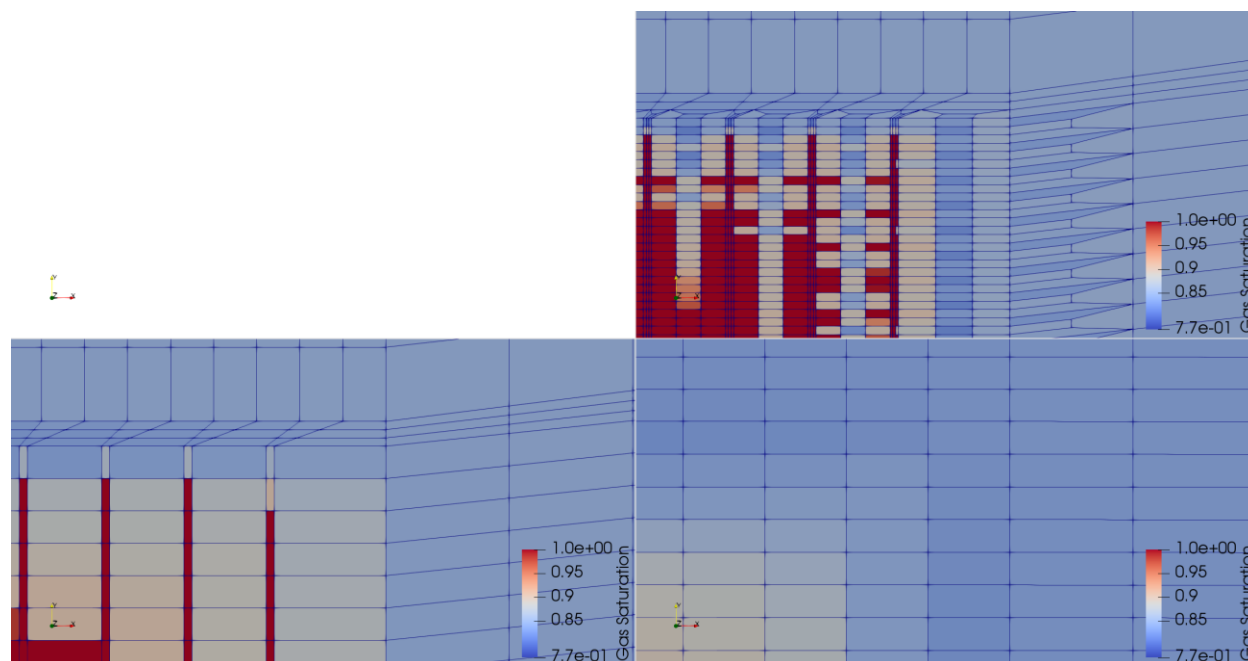


Figure 4-8. Plan view (XY slice) of saturation in the north east corner of the repository at time $t = 500$ yr. This is near time of the maximum dry out between the drifts for the refined simulations. Top left (Mesh 1): fully resolved simulation is not shown because it did not progress to this time. Top right (Mesh 2): simulation that resolves waste packages but not the DRZ. Bottom left (Mesh 3): simulation that resolves drifts but not waste packages. Bottom right (Mesh 4): Simulation that does not resolve the repository and has backfill throughout the repository area.

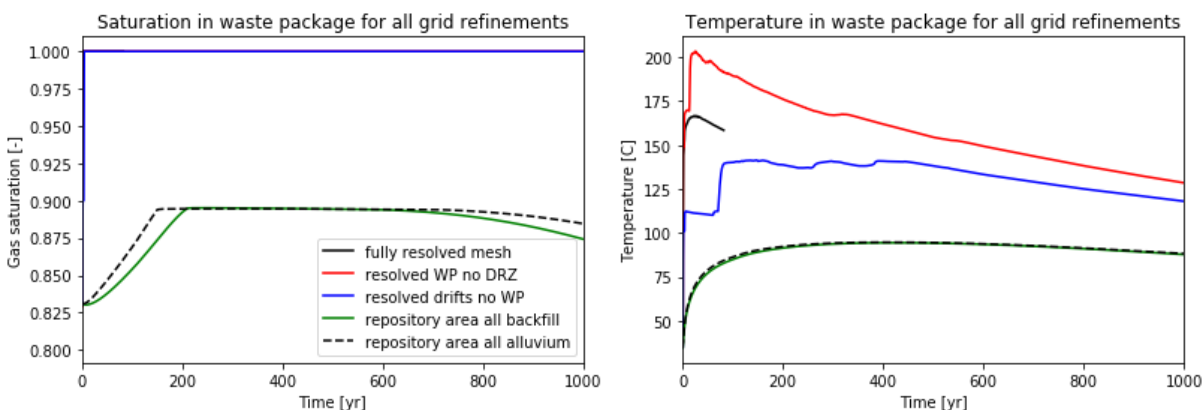


Figure 4-9. Gas saturation (left) and temperature (right) in the waste package for all 5 simulations.

4.2.2.2.2 In the Repository Between Drifts

Temperature and saturation at the midpoint between the two centermost drifts are shown in Figure 4-10. At this location all of the models do a relatively good job of capturing the temperature as a function of time. All of the coarsened meshes predict a slightly more rapid increase in temperature than the fully resolved model due to enhanced numerical dispersion.

The saturation between the drifts in the first few hundred years is only well-modeled by the mesh that resolves the waste packages. In that model the gas saturation first increases to one minus the residual water saturation as the mobile water flows out of the area, then 200 years later sufficient

heat has accumulated to flash the residual water to steam and the gas saturation abruptly changes to 100%. This is the correct sequence of events for propagation of gas in the repository. The model that resolves the drifts smears this two-step process, and the coarsest models do not capture the evaporation of the residual water at all.

4.2.2.2.3 In Surrounding Media

Figure 4-11 shows the gas saturation and temperature below the repository for all five simulations. As can be seen, the three meshes that resolve the drifts all predict a decrease followed by an increase in gas saturation and similar increases in temperature below the repository. The two simulations on the mesh that does not resolve the repository overestimate the gas saturation and underestimate the temperature at all times. Several observation points above and below the repository were compared, and the results were qualitatively similar.

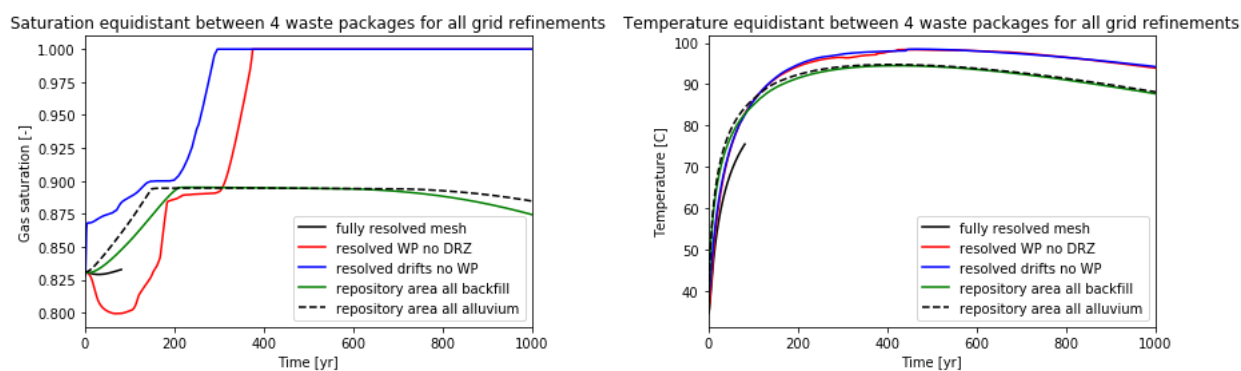


Figure 4-10. Gas saturation (left) and temperature (right) between two central drifts for all 5 simulation models.

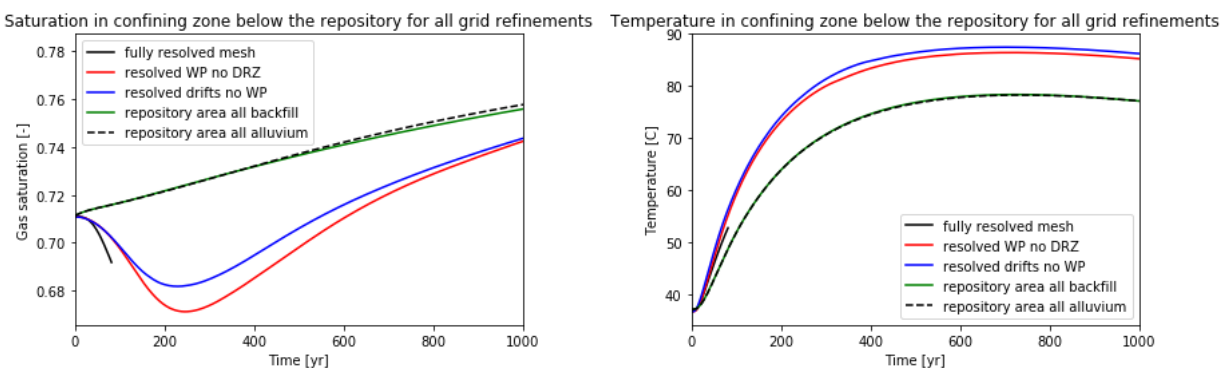


Figure 4-11. Gas saturation (left) and temperature (right) in the confining zone below the repository for all 5 simulation models.

4.2.2.3 Grid Refinement Conclusions

The simulation results have been compared for the five models with varying resolution. The two simulation meshes (Mesh 1 and Mesh 2) that explicitly grid the waste packages are able to resolve sharp temperature and saturation changes in the repository (Figure 4-9), but only the fully resolved grid (Mesh 1) seems accurate enough to capture the true peak values. The model that resolves only the drifts (Mesh 3) may be sufficient for modeling the area between drifts and is certainly usable for locations above and below the repository. The two models that did not resolve the

repository (Mesh 4) performed poorly at all observation points and are likely too coarse to be useful.

4.2.3 Single WP Model

In addition to the site-scale models in the previous section, a highly refined mesh of $\frac{1}{4}$ of a waste package was built. The geometry of this model is loosely based on the model in Section 6.2 of Sevougian et al. (2019b). It uses closed boundaries on all 4 lateral sides to simulate one waste package in the center of an infinite array of waste packages. The model is 150 m tall so that for heat sources representative of 24-PWR waste packages 100-year OoR, changes in temperature and saturation do not reach the top and bottom of the domain, which are both held constant at the initial condition.

The $\frac{1}{4}$ waste package model has identical dimensions to a package in the 25×27 array of the PA scale model and should be a good representation of the centermost waste packages in the array. The black rectangle in Figure 4-12 shows an XZ side-view of the part of the array captured in the $\frac{1}{4}$ waste package model. The single waste package model has dimensions $25 \times 10 \times 150$ m to represent 50 m drift spacing with 20 m between waste packages along the drift, like the site-scale array. This model has 37,440 elements with the mesh shown on the right side of Figure 4-13. The waste packages, drift, and damaged zone in Figure 4-13 have identical dimension to the fully resolved site-scale model. The low-permeability alluvium material above and below the repository have the same distance to the waste packages. All material properties are taken from the full-scale simulations. The initial conditions are equilibrated to have the same initial saturation, pressure and temperature as the site-scale model.

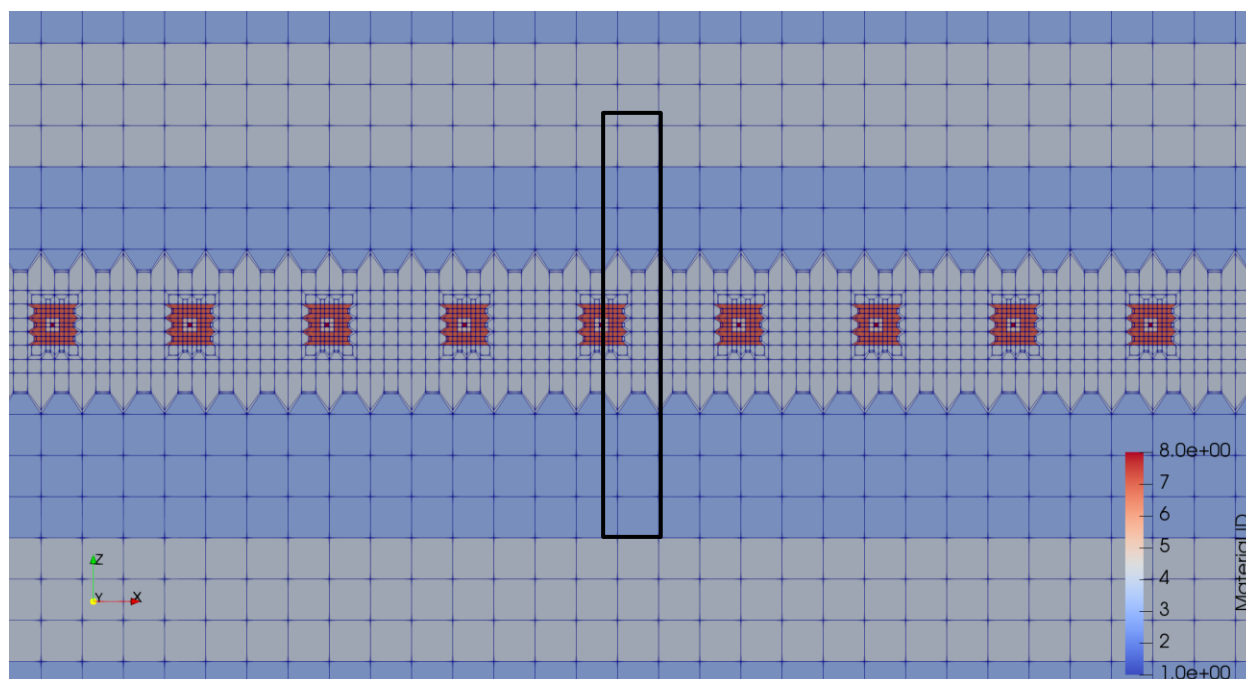


Figure 4-12. Section of the site-scale domain represented by the single waste package model is shown in the black square.

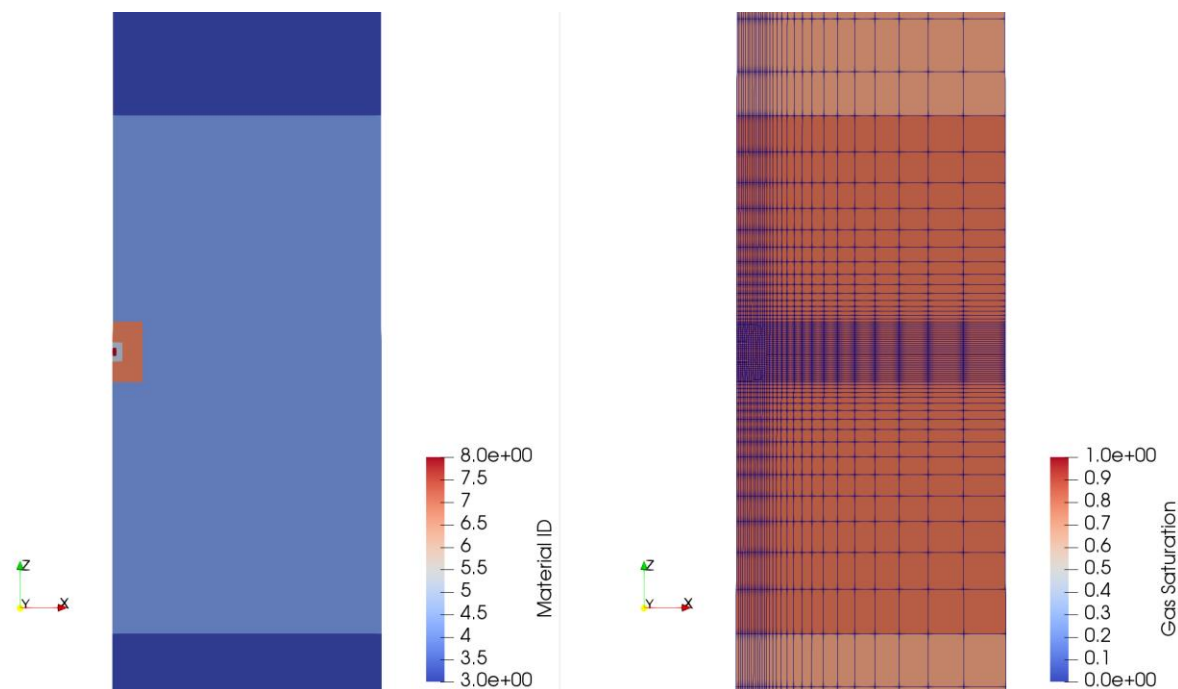


Figure 4-13. Left: Materials in the center section of the single waste package model. Waste package is Material 8, drift is Material 5, DRZ is Material 6 low permeability alluvium is Material 3 and high permeability alluvium is Material 4. Right: Gas saturation is lower in material 4 (high permeability) than material 3 (low permeability), like in full model. Simulation mesh is also shown. The full thickness of the model in the z direction is not shown.

One key change from Sevougian et al. (2019b) is that the waste package in the current study is rectangular. This was desirable because it preserves the waste package shape and dimension in the site-scale array. Furthermore, a model with nearly orthogonal cells everywhere will be numerically easier to simulate and have less potential for mass-conservation errors than the model with a radially flexed grid. Simulations with the Newton TR solver are shown, as it was far more computationally efficient in this model and has been benchmarked satisfactorily in the site-scale array section above.

4.2.3.1 Simulation Results for The Single Waste Package Model

Simulated saturation and temperature are shown for the $\frac{1}{4}$ waste package model with a 24-PWR waste package 100 years OoR in the alluvium formation in Figure 4-14, while Figure 4-15 shows saturation and temperature at selected observation points in and around the waste package.

Even though the waste package, drift and damaged zone have rectangular cross-section in this model, heat and the dry out zone propagate radially outward into the formation from very early time. For the first two snapshots in time in Figure 4-14, after 10 years and 50 years the dry out zone expands radially. At later times as the waste packages cool, the gas begins to migrate upward, and the dry-out zone forms a tear-drop shape. After 1000 years a large dry out zone still exists, even though the formation in the area shown near the waste package is a relatively constant temperature a few degrees warmer than the initial temperature.

This highly-refined model predicts that the region between drifts will never dry out completely, as can be seen in Figure 4-15 and the saturation profile on the top right of Figure 4-15. The waste

package dries out almost immediately, and the drift between the waste packages dries out in the first few decades, while saturation between the drifts increases slightly.

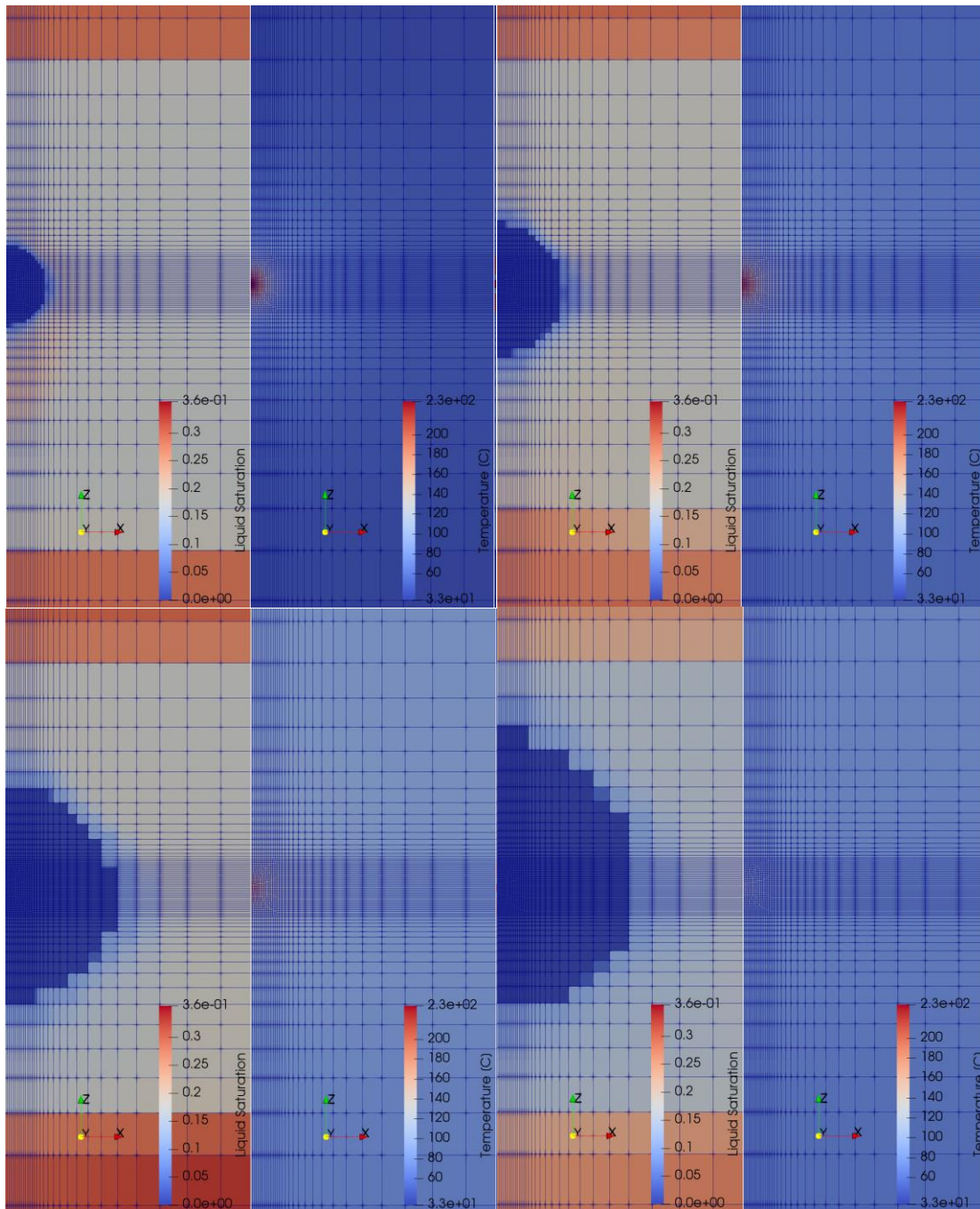


Figure 4-14. Top Left: simulated liquid saturation (left) and temperature (right) for 24-PWR waste package at 10 yrs, the time of peak temperature in the waste package. Top right: simulated liquid saturation (left) and temperature (right) at 50 years. Bottom left: simulated liquid saturation (left) and temperature (right) at 250 years. Bottom right: simulated liquid saturation (left) and temperature (right) at 1000 years, the time of maximum dry out.

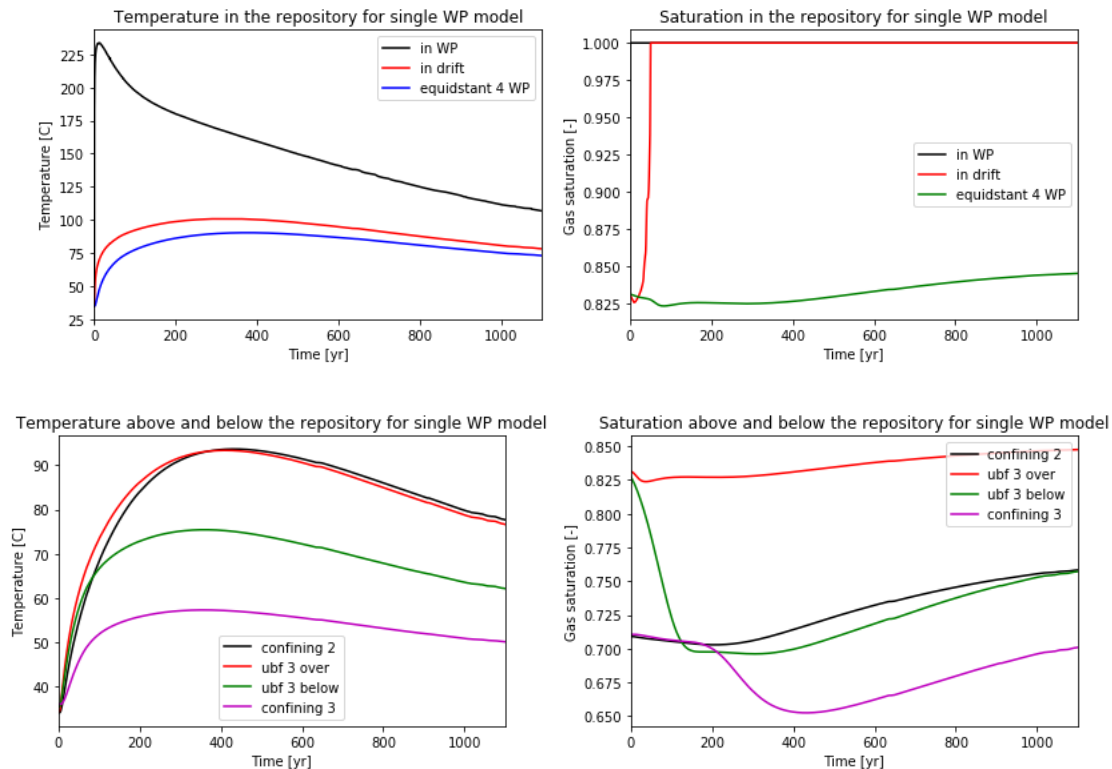


Figure 4-15. Temperature and gas saturation as a function of time for the $\frac{1}{4}$ waste package model. Temperature (top left) and gas saturation (top right) in the center of the waste package (in WP), in the drift halfway to the next waste package (in drift), and the midpoint between two drifts (equidistant 4 WP). Temperature (bottom left) and gas saturation (bottom right) in the formation that contains the repository (ubf 3 over and ubf 3 below—observation points in the upper basin fill just above and beneath the repository horizon) and in the confining beds above (confining 2) and below (confining 3) the repository.

The bottom left subfigure in Figure 4-15 shows that in the formation above and below the repository, temperature increases, but never reaches 100°C and dries out. Gas saturation in confining layer 2 and in ubf 3 above the repository increase slightly, while gas saturation at the two observation points below the repository decreases initially. As steam is formed it moves radially out from the waste package. When it reaches a cooler region it forms a re-condensation front, which can be seen in the top left of Figure 4-14, as a ring of higher water saturation surrounding the dried-out region. The condensed water is pulled downward by gravity, increasing the water saturation below the waste package. After the condensation front has passed and the formation cools the gas saturation slowly returns to its original value, as can be seen in the bottom right of Figure 4-15.

4.2.4 Comparison Across Model Scales

The most refined site-scale domain had waste packages modelled as three grid cells and the intermediate domain had waste packages as a single grid block, while the highly refined $\frac{1}{4}$ waste package model represents each waste package as $4 \times 4 \times 8 = 128$ grid cells (of which $\frac{3}{4}$ are mirrors in the closed boundaries). The $\frac{1}{4}$ waste package model provides a benchmark to test what physics at the small-scale are smoothed out by even the fully-resolved model with 2.4 million grid cells.

Figure 4-16 shows a comparison of the temperature and gas saturation between the $\frac{1}{4}$ waste package model and the centermost waste package in the two site-scale models that resolve the

waste packages. The top left subfigure shows that the site-scale models both predict a lower maximum temperature in the waste package. This is in part the result of numerical dispersion spreading out the temperature due to the relative coarseness of these meshes. However, the $\frac{1}{4}$ waste package model with closed boundaries represents a waste package at the center of an infinite array, so it may over-estimate the temperature of the real array that has dimensions 27×25 waste packages. The top right subfigure shows that the waste package dries out almost immediately in all the models and does not re-saturate during the 1000-year simulation.

The bottom of Figure 4-16 shows that the temperature and gas saturation between the drifts is very well modeled by the fully resolved site-scale model for the 82 years that it was able to simulate. The model that resolves the waste packages but not the drifts predicts complete dry-out of the area between the drifts, which is not observed in the $\frac{1}{4}$ waste package model. The temperature between drifts is also consistently overestimated by about 10 degrees. Over estimation of temperature away from the heat source coupled with underestimation of temperature inside the heat source (waste package) cells are consistent with what would be expected for numerical dispersion on the coarse mesh.

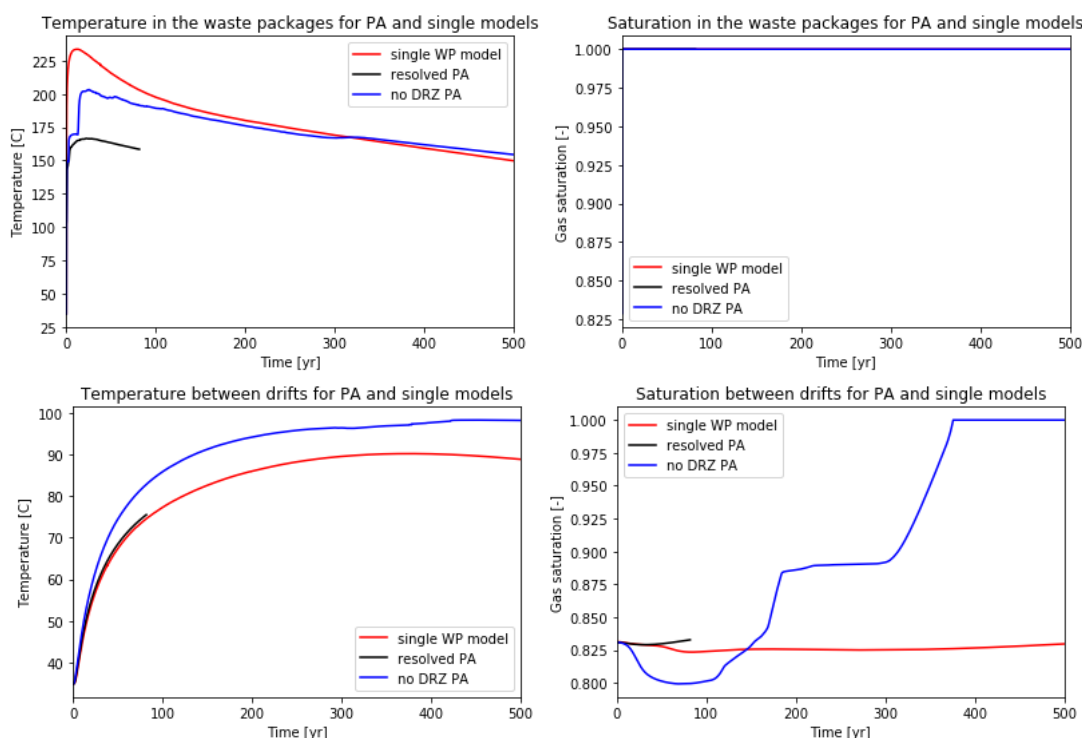


Figure 4-16. Saturation (left) and temperature (right) in and between the waste packages for the $\frac{1}{4}$ waste package model and the two site-scale models that resolve the waste packages.

4.3 Conclusions and Considerations for Future PA Modelling

The initial task in the UZ modelling section was to verify the suitability of the new Newton TR algorithm for simulations of this complex model. In all five models benchmarked this solver gave the same results as the default Newton LS method. The TR method was also much faster, allowing all except the finest mesh simulation to run to 1000 years within the 48-hour cutoff.

The study of multiple simulation models of one site-scale conceptual model has provided insight as to the level of grid refinement necessary to capture heat and fluid flow in the UZ repository for 24-PWR waste packages 100 years OoR. Of the five models, the most refined was unable to complete the simulation and the two least refined had unsuitable results for all observation points considered. The two intermediate models provided broadly acceptable results at observation points and could be improved through a suitable upscaling study.

Finally, a highly refined, $\frac{1}{4}$ waste package model was run to study dry out of the repository in detail. These results were also compared with the results of the site-scale models. This study served to highlight the impact of numerical dispersion, even in the site-scale models that resolved the waste packages.

Possible next steps for the alluvium reference case include:

1. Run simulations beyond 1000 years. The 1000-year simulation time in this work was too short to include the re-saturation process. Re-saturation can be challenging to simulate as the buoyancy driving force is so small and it is not always clear what direction is upstream. This may require additional code development.
2. Push the fully-resolved 2.4 million grid cell model to completion. The comparison with the $\frac{1}{4}$ waste package model highlighted the over-estimation of the dried-out region in the resolved waste packages model.
3. Develop intermediate-scale model that contains several waste packages, but is small enough to have a highly refined mesh. It could be used for additional benchmarking.
4. Simulate transport on one or more of the meshes to test the effects of grid refinement on radionuclide movement, including the impact of the dry-out zone. The grid resolution required for long-term radionuclide transport may be finer or coarser than required for the transient heat and fluid flow simulation.

4.4 Geologic Framework Model

A separate document by Gross et al. (2019) details the first steps in the development of a new geologic framework model (GFM) for an alluvial basin. In that work, development of a stratigraphic and hydrologic model of the Mimbres Basin from available seismic and well data is detailed.

A GFM must capture the geologic elements that may impact performance of a potential repository, such as basin geometry, stratigraphy, lithofacies, hydrofacies and geologic structures. The first step, and the focus of Gross et al. (2019), is to establish the geologic elements that define the boundaries of the alluvial sub-basin, such as depth to bedrock, basin-bounding and intra-basin faults, and the geometry of the bed rock on which the alluvial basin-fill sediments were deposited. The current basin structure GFM contains limited detail of the internal characteristics of the alluvium within the basin and these features will be added as part of future work. Eventually, the generic regional-scale GFM (whether an alluvial basin or other concept) will interface with the GDSA site-scale generic reference case.

5 GENERIC SHALE REFERENCE CASE

This section builds on the generic shale/argillite/clay reference case reported in Mariner et al. (2017), the shale Geologic Framework Model (GFM) presented in Sevougian et al. (2019b), and the near-field simulations addressing evolution of the disturbed rock zone (DRZ) in Sevougian et al. (2019b). Section 5.1 discusses additions to the shale GFM and the shale conceptual model for the features and process in the region of the GFM. Section 5.2 presents a geomechanical analysis of buffer resaturation and DRZ evolution on a fine-scale (i.e., high resolution grid) single-drift grid, developed for the eventual goal of showing how processes at this scale can be coupled to a coarser-scale PA grid. Finally, Section 5.3 presents the reference case and deterministic simulations of a generic shale host rock repository containing 24-PWR and 37-PWR DPC-canisterized commercial SNF, supplementing the 12-PWR and 4-PWR reference cases in Mariner et al. (2017).

5.1 Geologic Model for the Shale Reference Case

The geologic model for the shale (argillite) reference case includes a conceptual model of the geologic and hydrologic environment and a geologic framework model (GFM) to document and interpret the key features of a representative shale environment (the NBS). The methodology used to develop the shale GFM is documented in detail in Sevougian et al. (2019b). The methodology included selection of an area of Pierre Shale of suitable thickness and depth to locate a repository at a reference depth of 400 meters, identification of data sources to construct the GFM, and decisions on how to represent the stratigraphy of the region given incomplete data. The data used to develop the GFM were primarily oil and gas borehole logs that define the top elevation of each formation represented in the GFM. Interpolation of the elevation data from the boreholes was used to model the upper surfaces of each formation (Sevougian et al. 2019b).

The Pierre Shale was chosen as the basis of the shale conceptual model due to its large areal extent, thickness (>400 meters), accessible depth, stable tectonic history and desirable mechanical and hydrologic properties (Perry and Kelley 2017). The specific region chosen to develop the shale GFM is to the northeast of the Black Hills uplift in the Northern Great Plains Province (Figure 5-1). The dimensions of the region are 69 km (E-W) by 83 km (N-S). In this region, the Pierre Shale is near the top of a thick sequence (~1500-2000 meters) of sedimentary rocks dominated by marine shales in the upper part and sandstones and limestones in the lower part.

In this section, updates to the features of the shale GFM are presented and analytical methods are used to document the relationships between features represented in the GFM. Also updated are features and processes specific to the region of the shale GFM. The shale GFM was developed using RockWorks17® software (Rockware Inc., www.rockware.com) and ArcGIS 10.6 (ESRI, www.esri.com). The GFM was gridded at a horizontal resolution of 250 meters and a vertical resolution of 10 meters resulting in a grid array of 277 by 333 by 201.

5.1.1 Update of the Shale GFM for the Argillite Reference Case

This section presents new features and analyses that represent an update to the Shale GFM presented in Sevougian et al. (2019b). The new features are a synthetic fault that offsets the stratigraphy of the GFM and inclusion of the water table in this region. We also conduct a series of analyses using the GIS and GFM software to document the relationships between the reference repository horizon, the host formation, and hydrologic features represented in the GFM. Although

these analyses are applied to a relatively simple geologic environment, they demonstrate how the analytical tools available in GIS and GFM software can be used to evaluate areas where a repository could be located using basic criteria such as depth and thickness of the potential host formation.

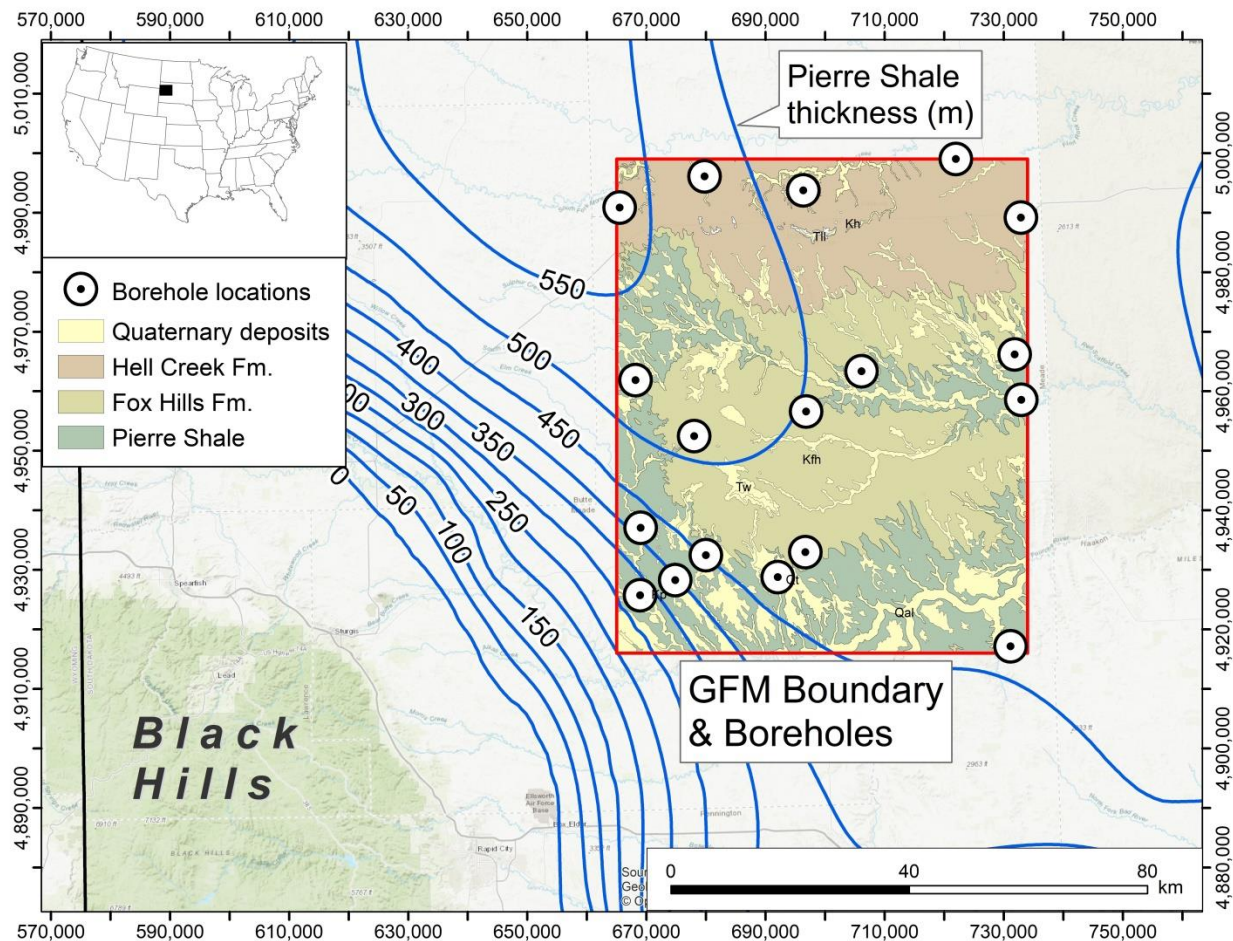


Figure 5-1. Location of the shale GFM and boreholes used as data inputs. The surface geology shown within the boundary of the GFM region is from Martin et al. (2004). Thickness contours for the Pierre Shale are from Perry et al. (2014). Note that the Pierre Shale is thinned by erosion where it ramps onto the Black Hills uplift.

5.1.1.1 Geologic and Hydrologic Features Represented in the GFM

The GFM represents a stratigraphic column of approximately 1500-1800 meters of sedimentary rock, depending on location (Table 5-1; Figure 5-2). The entire sedimentary sequence is characterized by alternating confining units (shales) that separate major regional aquifers (Figure 5-2). The upper half of the stratigraphy is dominated by Cretaceous shales (the Pierre Shale near the top as well as several hundred meters of underlying shale units) while the lower half of the stratigraphy includes the major regional sandstone and limestone aquifers as well as shale confining units (Figure 5-2). The Pierre Shale and the other sedimentary rocks ramp up to the southwest towards the Black Hills uplift and dip generally to the north and the northeast in the region of the GFM. In the northern portion of the GFM, the Pierre Shale is overlain by the Fox

Hills and Hell Creek Formations (combined in the GFM due to lack of borehole data; Figure 5-2). The sandstone facies within these formations comprise the Fox Hills/Hell Creek aquifer.

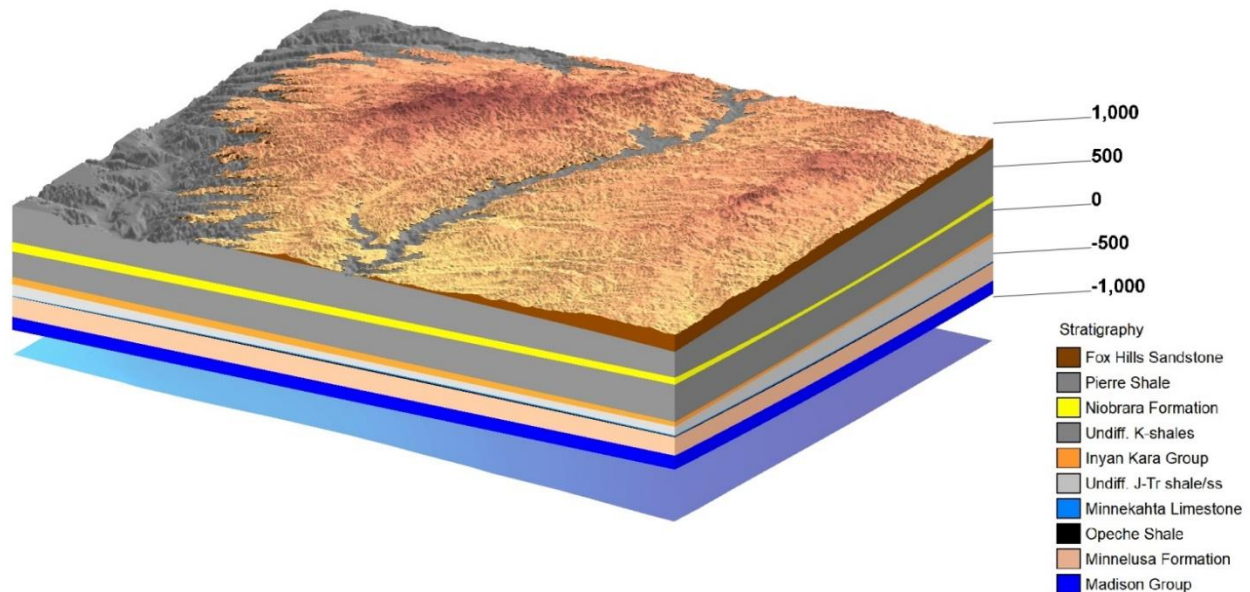


Figure 5-2. Block diagram of the stratigraphy represented in the GFM. View is from the northeast at 10x vertical resolution. Vertical scale is elevation relative to sea level. The Fox Hills Formation and parts of the Pierre Shale are at the modern erosional surface. The base of the GFM is the bottom of the Madison Group. The Precambrian surface (McCormick 2010) below the base of the Madison Group is shown for reference but is not part of the GFM.

The lower half of the stratigraphic column represented in the GFM includes four regional aquifers at depths of approximately 1000 meters (Inyan Kara aquifer) to 1500 meters (Madison aquifer; Driscoll et al. 2002). Groundwater flow in these aquifers is controlled largely by recharge in the Black Hills uplift to the southwest. Groundwater flows downgradient from the southwest to the northeast in the area of the GFM (Driscoll et al., 2002). The Inyan Kara aquifer is composed of several sandstone units and has a typical thickness of 100 meters. The Minnekahta aquifer is composed of laminated limestone and has a typical thickness of 15 meters. The Minnelusa aquifer is within sandstone in the upper half of the Minnelusa Formation and has a typical thickness of 100 meters (Greene, 1993). The Madison aquifer is composed predominantly of massive limestones of the Madison Group. The aquifer is contained within the upper 70 meters of the Madison Group, where fractures and paleokarstic solution features have created secondary porosity within the limestone (Greene, 1993; Driscoll et al. 2002).

Other aquifers in the region are considered minor or local aquifers. The Niobrara aquifer is not identified as an aquifer by Driscoll et al. (2002) in their discussions of Black Hills hydrology and Bredehoeft et al. (1983) consider it a minor aquifer. The Greenhorn Limestone, which lies below the Niobrara Formation and is separated from it by the Carlile Shale, is also considered a minor aquifer (Bredehoeft et al. 1983). The equivalent of the Dakota aquifer in the Black Hills region is the thin Newcastle sandstone which lies stratigraphically above the Inyan Kara Group and is separated from it by the Skull Creek shale (Bredehoeft et al. 1983). Well to the east of the Black Hills region, the Inyan Kara and the Newcastle sandstones merge (the Skull Creek Shale pinches out) and the aquifer is known as the Dakota aquifer.

The minor sandstone and limestone aquifers that lie above the Inyan Kara Group are included as part of the “undifferentiated Cretaceous Shales” in the GFM (Table 5-1). Within this undifferentiated interval, the Newcastle Sandstone is part of the Graneros Group, which includes three shale formations and the Newcastle Sandstone (Fahrenbach et al. 2007).

Estimates of the permeability and porosity of the formations in the GFM are summarized in Table 5-1. These estimates are based on data summarized in Driscoll et al. (2002) and Perry and Kelley (2017). A few permeability estimates are inferred based on like rock types.

Table 5-1. Stratigraphic and hydrologic properties of formations represented in the GFM.

Borehole Stratigraphy	Lithology	GFM stratigraphy	Thickness (m)	Representative thickness	Permeability m ²	Porosity %
Fox Hills Sandstone/Hell Creek Fm.	Sandstone, shale, siltstone	Fox Hills Sandstone	0-209	60	1e-13	20
Pierre Shale	Shale with minor sand or silt intervals	Pierre Shale	250-598	450	1e-19	10-30
Niobrara Formation	Shale, chalky limestone	Niobrara Formation	33-159	50	1e-14	40
Carlile Shale	Shale	Undifferentiated Cretaceous Shales	315-509	350	1e-20	20
Greenhorn Formation	Shale, limestone					
Graneros Group	Shale, sandstone					
Inyan Kara Group (regional aquifer)	Sandstone, shale	Inyan Kara Group	26-136	50	1e-13	20
Morrison Formation	Shale, sandstone	Undifferentiated Jurassic-Triassic Shales/Sandstones	106-259	200	1e-20	20
Sundance Formation	Sandstone, shale					
Spearfish Formation	Shale, gypsum					
Minnekahta Limestone (regional aquifer)	Limestone	Minnekahta Limestone	12-18	15	1e-12	10
Opeche Shale	Shale	Opeche Shale	12-34	20	1e-20	20
Minnelusa Formation (regional aquifer)	Sandstone	Minnelusa Formation	219-239	230	1e-12	10
Madison Group (regional aquifer)	Limestone	Madison Group	150-160	150	1e-12	35

5.1.1.1.1 Faulting

The GFM is in a stable region of the US that has been largely unaffected by Quaternary tectonism or faulting. No faults are documented within the area of the GFM, although normal and reverse faulting with displacements of several tens of meters has been documented directly the east of the GFM area (Nichols et al. 1994). Given the occurrence of faults to the east, it would not be surprising if similar (undocumented) faults occur within the area of the GFM. Although there are no documented faults to include in the GFM, we have an interest in introducing more complex features in the GFM for the purpose of developing a meshing capability for these features. To that end, we introduced a synthetic fault to the GFM. The fault geometry was chosen to be a simple normal fault with vertical displacement. We arbitrarily chose a fault displacement of 250 meters, to clearly see the offset of the formation surfaces within the GFM.

To create a fault model, data is needed for the location and orientation of the fault (fault trace), the fault dip (observed or inferred). The amount of offset on a fault can be obtained from subsurface

markers that indicate the displacement of surfaces on either side of the fault. These markers can be obtained from borehole data, geophysical imaging, or in some cases surface observations and mapping. In many areas where subsurface data is sparse, the geometry of a fault or fault system and the displacement of faulted surfaces must be estimated from simplified assumptions based on limited knowledge of the fault system.

For the synthetic fault, we assumed a constant offset of 250 meters for all the stratigraphic surfaces (Figure 5-3). We then manually offset each of the surfaces at the fault boundary using the raster or grid math utilities that are available in either ArcGIS or Rockworks. The workflow to create the synthetic fault is as follows:

1. Draw (from a map view) a NNE-trending fault trace across the extent of the GFM. This information is then included in a Rockworks fault file that also includes the dip angle (90 degrees in this case) and vertical extent of the fault plane.
2. Use the fault trace as a segment of a polygon that is used to clip the original unfaulted surfaces into two surfaces separated by the fault.
3. Use grid math tools to calculate a 250-meter offset of the downthrown surface.
4. Repeat these steps for all the stratigraphic surfaces included in the GFM.

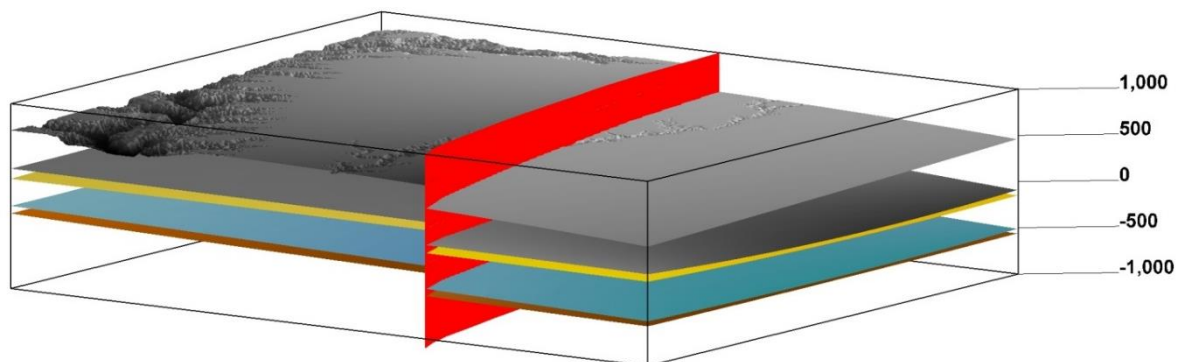


Figure 5-3. Synthetic fault (red surface) offsetting the upper four stratigraphic units in the Shale GFM. View is from the northeast at 10x vertical exaggeration. The fault is vertical and offsets each of the stratigraphic units by 250 meters.

The results of the workflow are shown in Figure 5-3. Only the upper four stratigraphic units were calculated for this example. The resulting model demonstrates the capability to create a fault surface and offset stratigraphic surfaces. These surfaces can be meshed using CUBIT for use in simulation modeling.

Rockworks is not intended to model complexly faulted systems that include multiple faults or fault intersections. High-resolution geophysical imaging is typically required to constrain the geometry of complexly faulted systems, a capability that is most commonly applied in the oil and gas industry. GFM software with more advanced fault modeling capabilities can solve fault/surface or fault/fault intersections to ensure that no gaps or intersection errors exist.

5.1.1.1.2 Depth and Elevation of the Water Table

The configuration of the water table in the GFM region is important to document because it delineates the boundary between the saturated and unsaturated zones. Groundwater levels were obtained from water well data that resides in the USGS National Water Information System Groundwater Levels database (<https://nwis.waterdata.usgs.gov/usa/nwis/gwlevels>). Seventy-seven water wells from the database lie within the boundary of the GFM. The data points for water table depth were used to create a water table depth surface using nearest neighbor interpolation in ArcGIS (Figure 5-4, left panel). Water depths in wells range from less than 10 meters to more than 120 meters in the southwestern portion of the GFM. There is no clear spatial pattern to the depth to the water table and, accept for a few areas, the water table in a large proportion of the GFM is at a depth of less and 20 meters (Figure 5-4, left panel) and resides within the Fox Hills Formation.

To calculate the elevation of the water table, the water table depth surface was subtracted from the ground surface (DEM) using grid math (Figure 5-4, right panel). As expected, the water table elevation follows the topography of the region and is highest in areas with the highest topography. A 3-D view of the water table elevation relative to the upper surface of the Pierre Shale shows that the water table lies above the top of the Pierre Shale in much of the northern portion of the GFM (Figure 5-5). These areas correspond to areas where the Fox Hills Formation is present; within these areas the water table lies within the Fox Hills Formation.

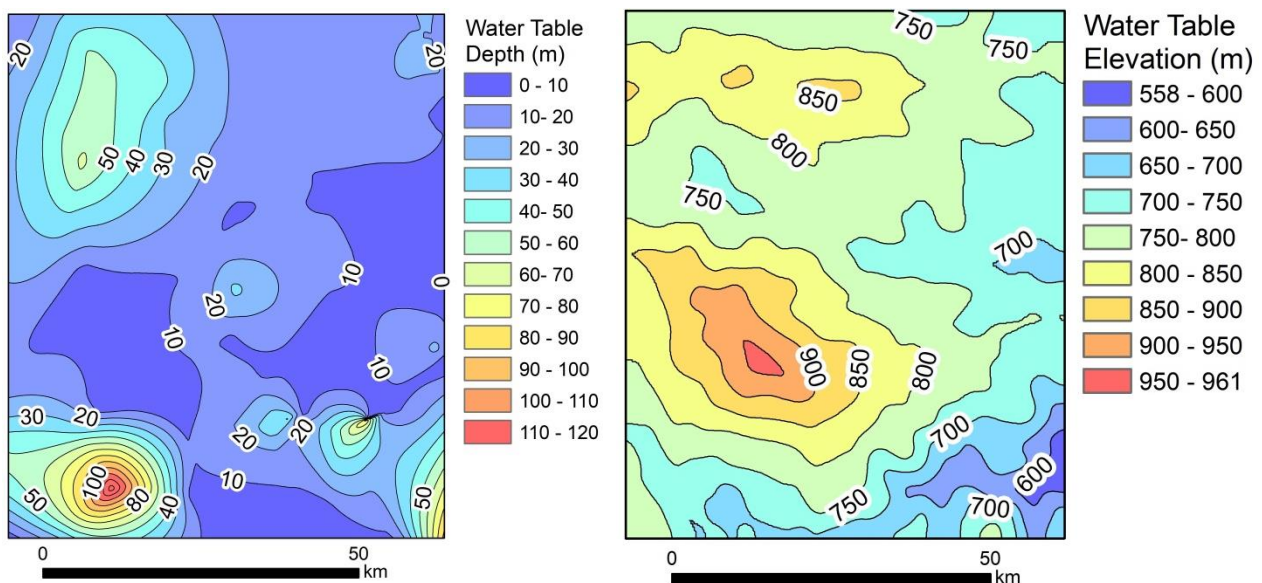


Figure 5-4. Depth (left) and elevation (right) of the water table in the GFM.

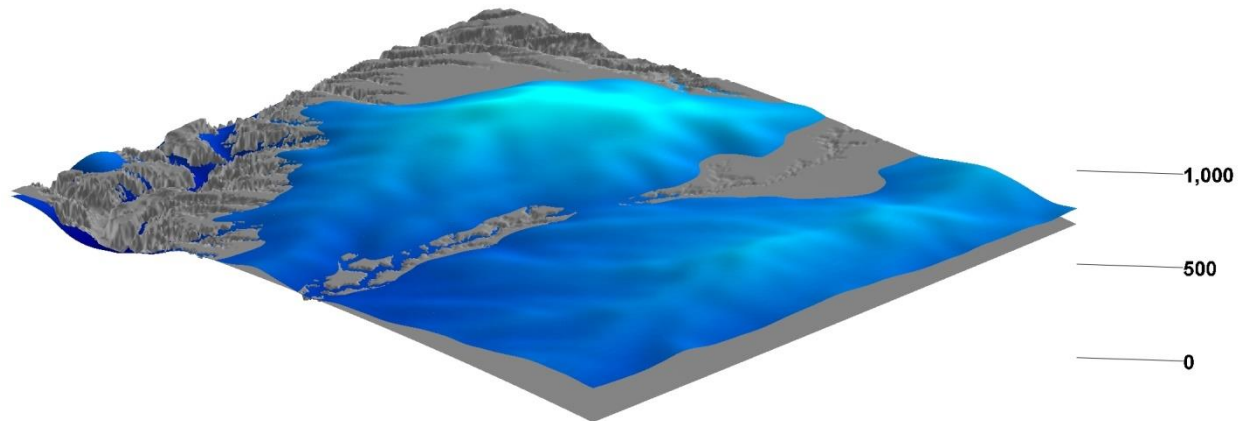


Figure 5-5. 3-D view of the relationship between the top of the Pierre Shale (gray surface) and the water table (blue surface). View is from the northeast with a vertical exaggeration of 10x. In much of the area, the water table lies above the top of the Pierre Shale within the Fox Hills Formation. The water table surface is the equivalent of the map view of elevation in Figure 5-4. Vertical scale is in meters relative to sea level.

5.1.1.2 Analysis of the Relationships between Geologic and Hydrologic Surfaces

One purpose of a GFM is to analyze the relationships between the features represented in the model. For the purposes of SFWST, this would include analyzing the relationship between a reference repository depth and key features related to repository location such as the host rock geometry and key hydrologic features. These relationships can be analyzed using the analytical capabilities of GIS and GFM software with the results displayed as 2-D maps or 3-D visualizations.

Determining the quantitative relationship of features in the geologic environment to a reference repository horizon involves grid math calculations to determine distances (e.g., thickness, depth, vertical separation) between the repository horizon and the features of the GFM. The spatial relationships of these features can constrain the areas of a host rock that are suitable for locating a repository. Similar analyses of the depth and thickness of the host rock relative to potential repository locations within the host rock have been carried out for other repository programs (e.g., Vis and Verweij 2014).

5.1.1.2.1 Relationship of Repository Horizon to the Pierre Shale Geometry

Depth to the repository is often imagined as a horizontal plane of constant elevation. This is true only in a region where the ground surface is flat. In an area of topographic relief, the depth to a repository is not constant over the area of the repository but varies depending on the surface relief above the repository. As an example, the depth of the proposed Yucca Mountain repository block varied by more than 100 meters depending on location relative to the crest and slopes of Yucca Mountain.

The depth of the reference case repository is 400 meters below the ground surface. Using grid math functions in the GIS and GFM software we constructed a constant-depth surface of the repository horizon by subtracting 400 meters from the DEM representing the ground surface. The repository horizon surface represents the 400-meter depth from the surface at every grid point in the GFM. It therefore mimics the surface relief of the GFM.

The relationship between the repository horizon and the top and base of the Pierre Shale is shown in Figure 5-6. The 400-meter repository horizon lies within the Pierre Shale over most of the area

of the GFM (Figure 5-6, bottom). In the northern 2/3 of the GFM, the base of the Pierre Shale lies between 100 and 300 meters below the repository horizon with the distance increasing to the north, consistent with the regional northerly dip of the formation (Figure 5-6, top left). Along the southern margin of the GFM the repository horizon lies below the base of the Pierre Shale and a repository could not be located in these areas if the 400-meter repository horizon was honored (Figure 5-6, top left). The depth of the repository horizon below the top of the Pierre Shale is 400 meters where the Pierre Shale is at the ground surface and between 400 and 120 meters where the Fox Hills Formation is present above the Pierre Shale (Figure 5-6, top right).

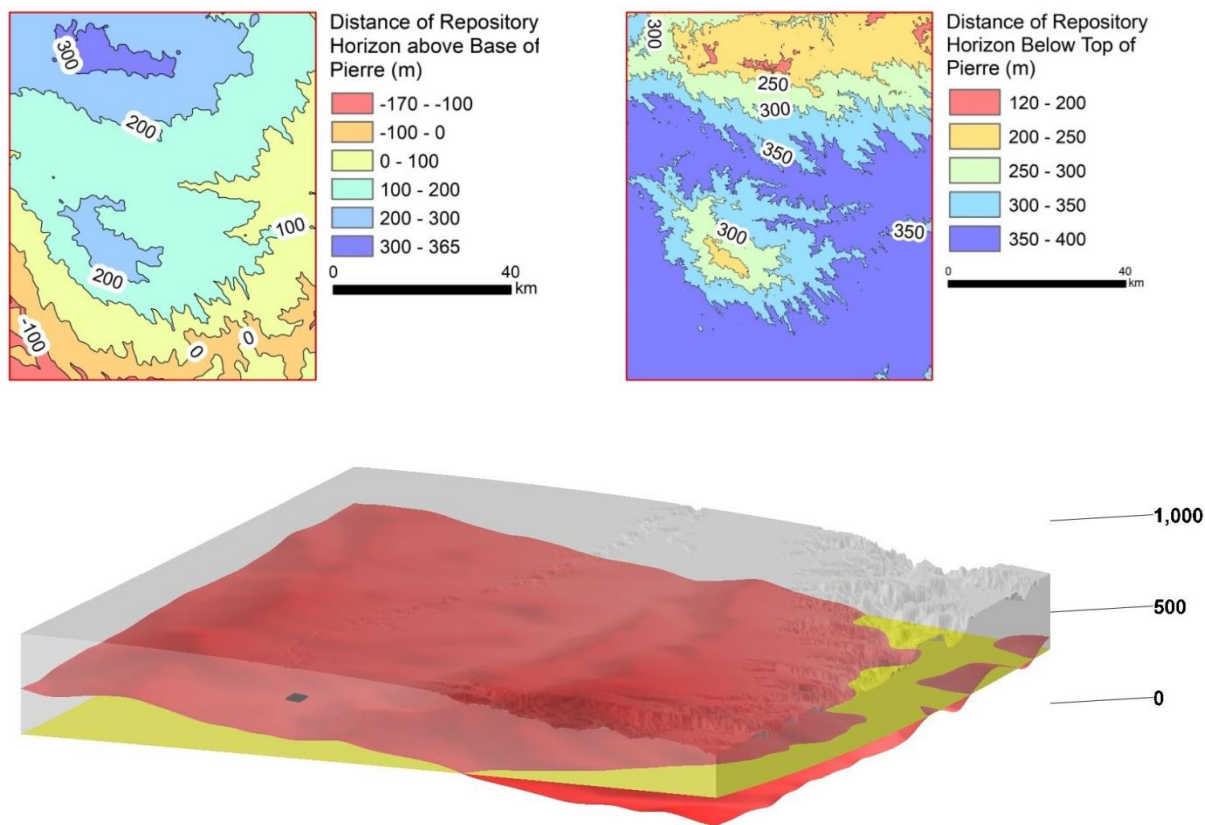


Figure 5-6. 2-D and 3-D representations of the relationships between a reference repository depth of 400 meters and the top and bottom of the Pierre Shale. In the 3-D view (bottom panel) the repository depth is the red surface and the semi-transparent gray volume is the Pierre Shale. The base of the Pierre shale is shown in yellow. View is from the southwest at a vertical exaggeration of 10x. Shown for scale is the shale reference repository footprint (black) that is pinned to the repository depth surface (front left of bottom panel).

5.1.1.2.2 Relationship of Repository Horizon to Hydrologic Features of the Region

Hydrologic features included in the GFM are the water table and major aquifers. The vertical distances between the water table, the Inyan Kara aquifer and the repository horizon are calculated using grid math. These calculations show the thickness of the saturated zone above the repository horizon and the distance between the repository horizon and first major aquifer that lies below the repository horizon.

The water table in the region of the GFM typically lies at a depth of 10-20 meters (Figure 5-7), well above the reference repository horizon. The distance from the repository horizon to the water table ranges from 265 meters almost 400 meters (Figure 5-7). Over most of the GFM area, the water table is 380 to 400 meters above the repository horizon, which defines the typical thickness of the saturated zone above the repository horizon.

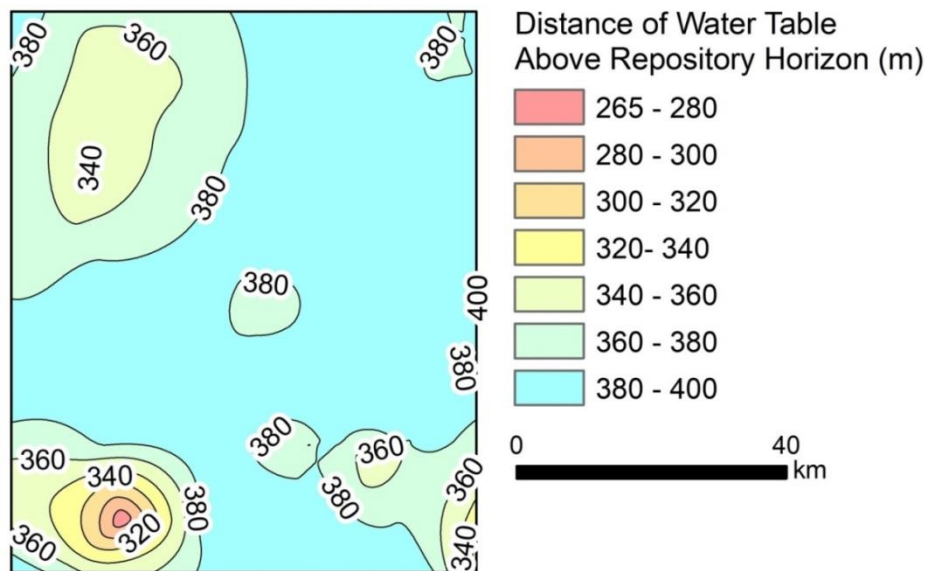


Figure 5-7. Distance of the water table from 400-m depth repository horizon. The distance represents the thickness of the saturated zone above the repository horizon.

The water table in the region of the GFM typically lies at a depth of 10-20 meters (Figure 5-7), well above the reference repository horizon. The distance from the repository horizon to the water table ranges from 265 meters almost 400 meters (Figure 5-7). Over most of the GFM area, the water table is 380 to 400 meters above the repository horizon, which defines the typical thickness of the saturated zone above the repository horizon.

The Inyan Kara aquifer is the first regional aquifer lying below the Pierre Shale and the undifferentiated Cretaceous Shales (Figure 5-2). The thickness of shale between the reference repository horizon and the Inyan Kara aquifer thus represents a thick low-permeability barrier between the repository and a potential pathway for radionuclide migration. The distance between the repository horizon and the Inyan Kara Group ranges from less than 400 meters in the southern part of the GFM to more than 700 meters in the northern part (Figure 5-8). The increased separation of these surfaces to the north is due to the northerly dip of the formations, a general thickening of units to the north and the higher elevation of the repository horizon to the north (Figure 5-6). The northern area of the GFM thus provides a thicker low-permeability barrier between the repository horizon and the Inyan Kara aquifer.

The spatial relationships between the Pierre Shale, hydrologic features and the repository horizon are shown together in a 3-D visualization of the GFM (Figure 5-9).

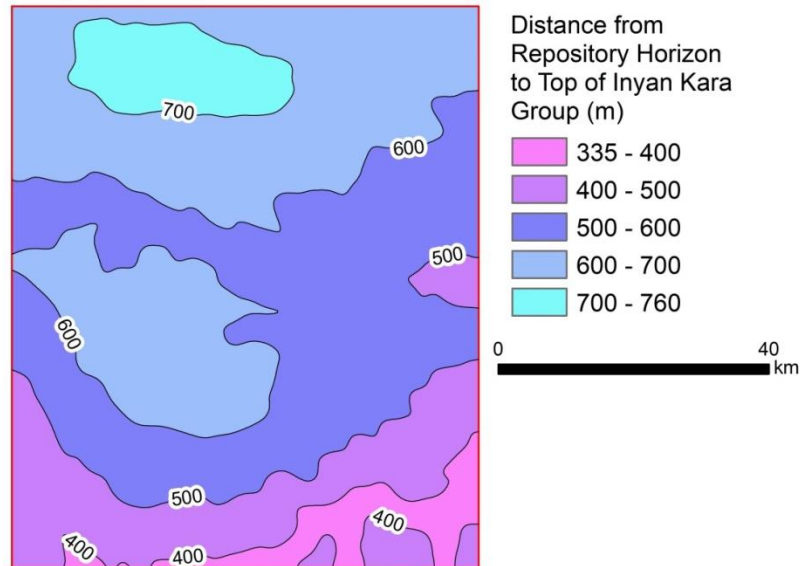


Figure 5-8. Depth (distance) of the Inyan Kara aquifer below the 400-m depth repository horizon.

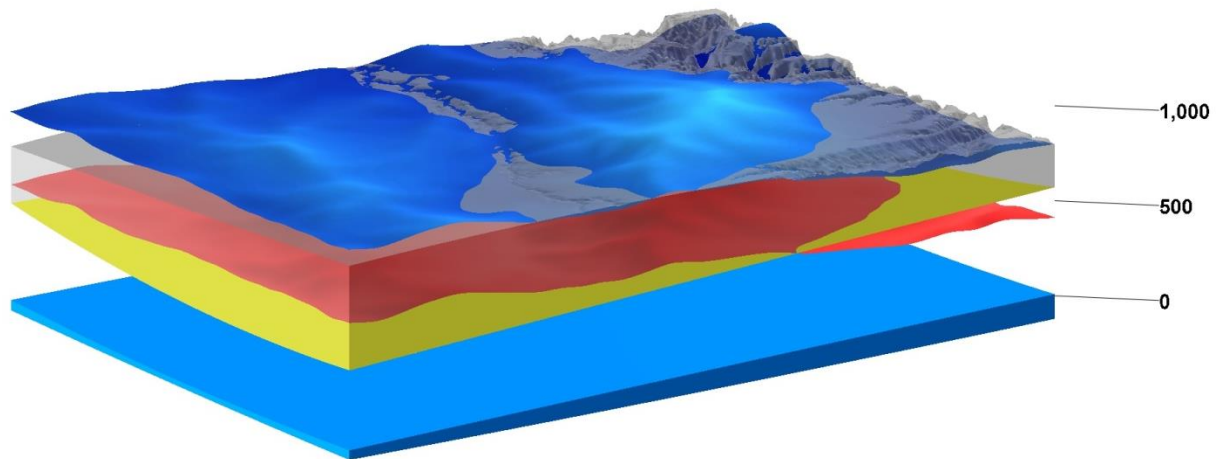


Figure 5-9. View of the GFM from the northwest showing the relationships between the water table and Inyan Kara aquifer (blue surfaces), the Pierre Shale (semi-transparent gray, base is yellow) and the reference repository depth (red surface). The base of the Fox Hills aquifer is approximately coincident with the top of the Pierre Shale.

5.1.1.3 Meshing the Features of the GFM

One of the goals in developing the shale GFM is to demonstrate a workflow that uses the features of the GFM to create a mesh for simulation modeling. This is accomplished by exporting the geologic surfaces (formation tops) shown in Figure 5-10 for input into the meshing software. Generating a simulation mesh from the geologic surfaces generated by Rockworks required a multistep process using python, CUBIT and SCULPT software (Owen et al, 2019a; Owen et al, 2019b).

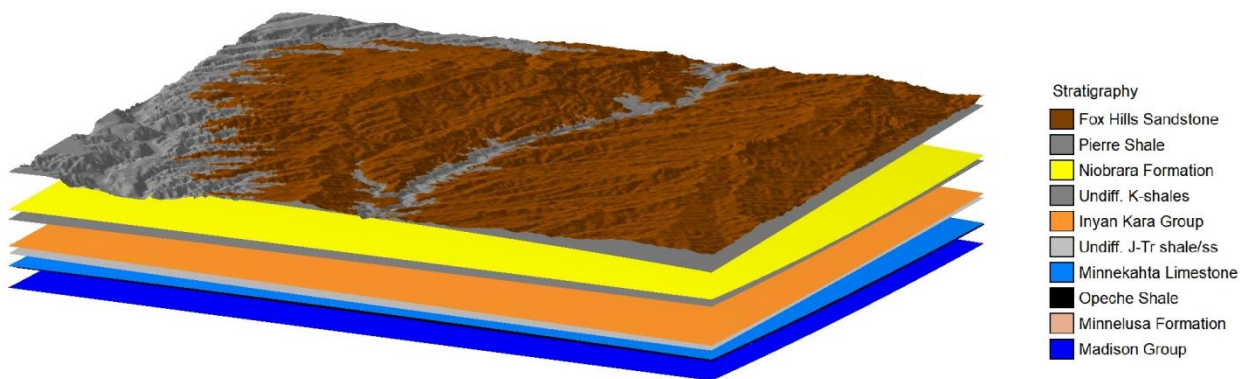


Figure 5-10. Surfaces (formation tops) used as the basis for meshing the features of the GFM.

The geologic software outputs each surface as coordinates on a grid of equal-distant points in x and y , but CUBIT requires connectivity data to read in surfaces. The first step in generating a surface mesh is a python/CUBIT script that connects each point in space with its three nearest neighbors. A small rectangular surface is then created for each set of neighbors. Each of these surfaces is joined together into a single large surface that spans the model in x and y space. This surface is meshed to the desired resolution, in this case 1000 meters by 1000 meters (x , y). The surface mesh is then exported in STL format. This process is repeated for all 10 surfaces that span the entire shale GFM.

Finally, the SCULPT software is used to create the volume mesh for simulation (Figure 5-11). The Fox Hills base surface is used to create a volume mesh that extrudes to a flat surface beyond the base of the Madison group. This volume is then cut by each of the interior surfaces. The Minnekahta Limestone and Opeche Shale are left out of the final volume because their vertical extent is much thinner than the current vertical grid resolution. New developments in SCULPT make it possible to create a mesh that includes these thin formations, however the resulting mesh has very small grid cells between the surfaces and the number of cells in the model increases accordingly.

The Fox Hills is also omitted because it has an erosional surface that pinches out without extending to all edges of the domain. The current workflow can only generate surfaces that span the full model in x and y space (Figure 5-11). The lowest volume in the model has a flat base surface. This volume could be deleted or used in the simulation model as impermeable cells to easily make a no-flow boundary at the base of the model.

5.1.2 Update of the Shale Conceptual Model for the Region of the GFM

Perry and Kelley (2017) presented a geologic and hydrologic conceptual model of the Pierre Shale and the surrounding geologic environment to support the argillite reference case. This model was generalized in that it did not represent a specific area of the Pierre Shale, but the formation as a whole. Included in the conceptual model were estimates of hydrologic properties (permeability, porosity) for the Pierre Shale and adjacent formations and a discussion of the high clay content of the Pierre Shale (~70%), which is at the upper end for shales. Clay content determines the sealing properties and other material properties of the shale (Bourg 2015). The conceptual model also presented a review of the pore water chemistry of the Pierre Shale, which is moderately saline and

reducing at depth as indicated by the presence of organic carbon and pyrite in unoxidized samples (Schultz et al. 1980; Neuzil 1993).

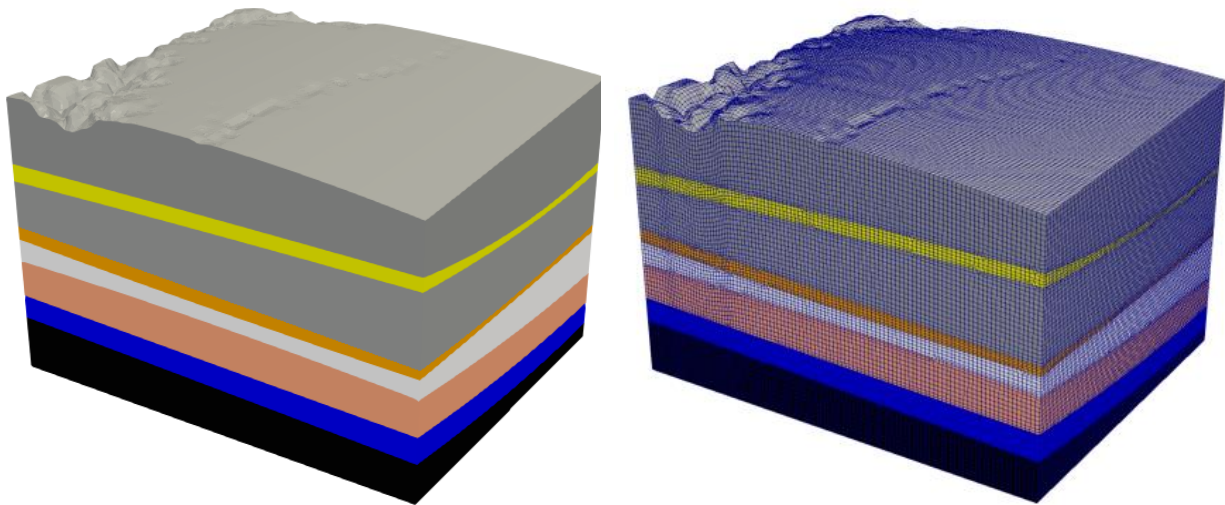


Figure 5-11. Results of the meshing process represented as formation volumes (left) and a hexahedral mesh (right). View is from the northeast at 30x vertical exaggeration.

Perry and Kelley (2017) also reviewed the issue of the scale dependency of shale permeability (Bredehoeft et al., 1983; Neuzil 1993; Neuzil 2015). Laboratory tests and field-scale borehole tests indicate permeabilities that typically range from 10^{-19} to 10^{-21} m². Regional scale modeling of drawdown in the Dakota Sandstone below the shale confining formations indicate a significant amount of water was supplied from the confining shales during groundwater withdrawal (Bredehoeft et al. 1983). This result requires leakage of groundwater into the confining shales and a regional-scale permeability of $\sim 10^{-16}$ m² for the Pierre Shale. This higher permeability suggests that flow through the shale is largely through fractures and that the lower permeabilities measured in laboratory and field tests reflect unfractured rocks or rocks with non-transmissive fractures (Bredehoeft et al. 1983; Neuzil 1993).

Neuzil (1993) and Neuzil (2015) described the presence of an anomalously low-pressure region preserved in the midlevel thickness of the Pierre Shale and concluded that preservation of the anomaly requires very low permeability, in contrast to the apparently higher regional permeability that suggests fracture flow. This suggests that pressure anomalies are preserved within large shale blocks (scale of several kilometers or more) that lie between sparse regional fracture networks (Neuzil 2015). Identifying low-permeability regimes within a shale body would be an important task when considering siting of a repository within shale.

In this section we update the shale conceptual model to include features and processes that are specific to the area of the GFM. We focus on the hydrologic setting and processes of the GFM region and the characteristics of the lower part of the Pierre Shale, where a reference repository would be located given the geometry of the Pierre Shale in the GFM region.

5.1.2.1 Hydrologic Features and Processes of the Black Hills Region

The hydrology of the Black Hills region is described by Bredehoeft et al. (1983) and Driscoll et al. (2002). Because it is the major area of groundwater recharge in the region, the Black Hills uplift dominates the hydrology of the region. Precipitation in the Black Hills averages 50 cm/year. Recharge occurs primarily in outcrops of the permeable sandstone and limestone units that are ramped up at the margins of the Black Hills uplift (Figure 5-12). Because of their large outcrop areas, 84 percent of recharge to bedrock outcrops is to the Madison and Minnelusa Formations, which are the most heavily used aquifers in the region (Driscoll et al. 2002). The recharge areas in the Black Hills are to the southwest of the GFM and groundwater flow in the area of the GFM is to the northeast (Driscoll et al. 2002; Figure 5-13).

The Madison and Minnelusa aquifers in particular are the source of artesian springs that discharge around the periphery of the Black Hills (Driscoll et al. 2002). In these formations, paleokarstic dissolution features and breccia pipes provide a hydraulic connection between the two aquifers and possibly the Minnekahta aquifer (Driscoll et al. (2002). Artesian springs do not discharge beyond the outcrop limits of the Inyan Kara group, indicating that there are no pathways (fractures or faults) to the surface in areas where the Pierre and other Cretaceous shales confine the Inyan Kara Group (i.e., the GFM area; Figures 5-12 and 5-13).

We are not aware of any measurements of the potentiometric surface of the Inyan Kara aquifer in the area of the GFM, but the groundwater gradient may be approximated as groundwater flow is generally thought to follow bedding dips (Driscoll et al. 2002). For the Inyan Kara structural surface, the regional dip results in a decrease in elevation of 50 meters over a distance of 10 km in the southwest part of the GFM region (closest to the Black Hills) to 20 km in the northern part of the GFM (Sevougian et al. 2019b). These values suggest a groundwater gradient of 0.0025 to 0.005.

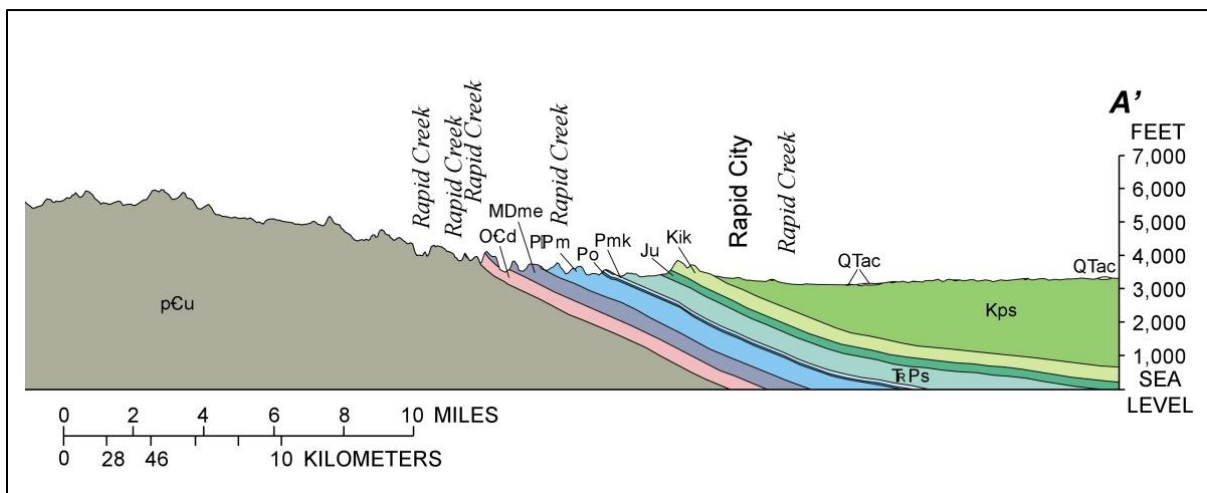


Figure 5-12. E-W cross-section through the eastern margin of the Black Hills uplift (Driscoll et al. 2002). Major regional aquifers are the Madison (MDme), the Minnelusa (PPm), and the Inyan Kara (Kik). The Pierre Shale and underlying Cretaceous shales are the upper confining unit (Kps).

Potentiometric surface contours for the upper Cretaceous aquifer (Fox Hills) were presented by Lobmeyer (1985). These contours indicate that the Fox Hills aquifer in the northern part of the GFM has a groundwater gradient of approximately 0.003 with flow to the east, which is similar to the gradient estimated for the Inyan Kara Group.

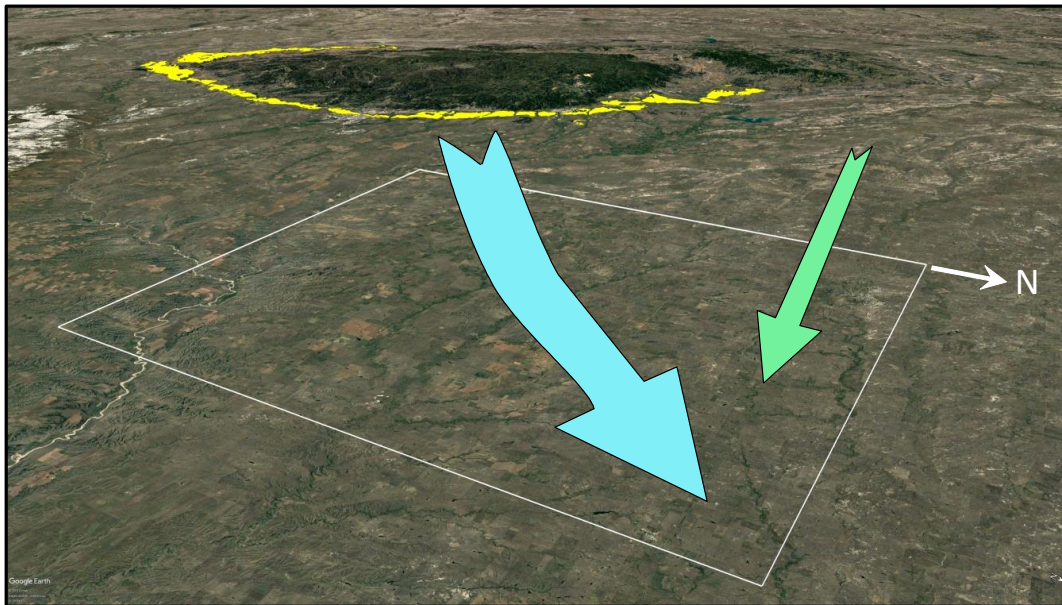


Figure 5-13. View to the west of the Black Hills uplift and outcrop area of the Inyan Kara Group (yellow pattern) relative to the boundary of the GFM. The southwest corner of the GFM boundary is 35 kilometers from the closest Inyan Kara outcrop. The outer margins of the Inyan Kara outcrops mark the outer boundary of artesian springs in the Black Hills region. The blue arrow indicates the general direction of groundwater flow within aquifers that are recharged in the Black Hills. The green arrow indicates the general direction of groundwater flow within the Fox Hills aquifer.

5.1.2.2 Characteristics of the Lower Pierre Shale

Except for the northwest corner, the reference repository horizon lies in the lower half of the Pierre Shale within most of the area of the GFM (Figure 5-6). Formations in the lower part of the Pierre Shale in the Black Hills region are the Red Bird Silty, Mitten, Sharon Springs and Gammon Ferruginous Formations (Martin et al. 2007; Bertog 2010)—see Figure 5-14. These are black shales with higher organic content than the upper formations of the Pierre Shale (Schultz et al. 1980). A measured stratigraphic section described by Schultz et al. (1980) to the northeast of the Black Hills uplift (about 40 km northeast of the northeast corner of the GFM) has a total thickness of about 450 meters with lower Pierre Shale forming the lower 120 meters. The total thicknesses of these formations are expected to increase to the west within the area of the GFM.

The three lower formations in the Pierre Shale (Gammon, Sharon Springs, Mitten)—see Figure 5-14 have higher organic content than the formations that make up the upper Pierre Shale Group. The organic carbon of these units ranges from 0.7 to 1.8 percent, compared to ~ 0.6 percent in the upper formations (Schultz et al. 1980). Pyrite is also most abundant in the Sharon Springs Formation, constituting about 7 to 9 percent of the rock, where typical content in the rest of the Pierre Shale is 1 to 3 percent (Schultz et al. 1980). The presence of organic carbon and pyrite in the Pierre Shale indicate deposition under anaerobic, reducing conditions that still persist at depth. A repository located within the lower Pierre Shale would lie within a reducing environment that has relatively high organic content and is saturated with moderately saline groundwater (Schultz et al. 1980; Neuzil 1993).

		Western	Central/Eastern
Pierre Shale Group	upper unnamed shale		Elk Butte Fm.
	Kara Bentonitic Fm.		Mobridge Fm.
	Monument Hill Bentonitic Fm.		Virgin Creek Fm.
	lower unnamed shale		Verendrye Fm.
			DeGrey Fm.
	Red Bird Silty Fm.	← →	Gregory Fm.
	Mitten Fm.		Sharon Springs Fm.
	Sharon Springs Fm.		
	Gammon Ferruginous Fm.		

Figure 5-14. Formations of the Pierre Shale Group. Western (left) column are formations recognized in western South Dakota/North Dakota and Eastern Wyoming including the region around the Black Hills uplift. Central/Eastern (right) column refers to formations recognized in the central South Dakota and in eastern South Dakota/North Dakota (Martin et al., 2007; Fahrenbach et al., 2007) The lower Pierre Shale Group includes the formations below the top of the Red Bird Silty Formation. Figure modified from Korn and Pagnac (2017).

5.2 Reduced Order Modeling and Geomechanical Analysis

This study investigates the near-field thermal-hydrologic behavior of pore fluids and the resulting geomechanical impacts to the disturbed rock zone (DRZ) surrounding the drifts of a shale-hosted deep geologic repository subject to waste-heat thermal loading. The DRZ surrounding a repository tunnel excavation area (see Figure 5-15) connects the host rock to the EBS and therefore acts as a link for flow and reactive transport between these two components of the repository system. If the physical properties of the DRZ evolve over time, then flow and transport processes could correspondingly be affected. Near-field coupled THM simulations using the TOUGH-FLAC software suite have demonstrated that during the repository re-saturation process post-closure, bentonite backfill material within the repository can swell and exert stress on the surrounding formation (Rutqvist et al., 2011). This swelling stress could work to compress fractures in the surrounding DRZ and therefore lower its permeability; furthermore, it has been suggested that geochemical changes (e.g. changes in ionic concentration) with time could simultaneously work to reduce swelling stress (Rutqvist et al., 2014).

Near-field processes such as those identified above constitute linkages for flow and transport between a repository and the far-field, which can involve transport of reactants from the far field to waste package surfaces as well as transport of radionuclides from a drift to the far field. The focus of this study is to perform geomechanical analysis of buffer swelling stress due to thermo-hydrologic processes with the goal of adopting more sophisticated process models in the future to

study how these processes influence DRZ permeability and ultimately geochemical transport. For the geomechanical analysis of the host rock, we model bentonite swelling stress as a function of liquid saturation changes during the re-saturation process in a GDSA PFLOTRAN near-field model. To do this, we employ a combination of empirical and theoretical relationships as functions of PFLOTRAN state variables (e.g., pressure, saturation, and temperature).

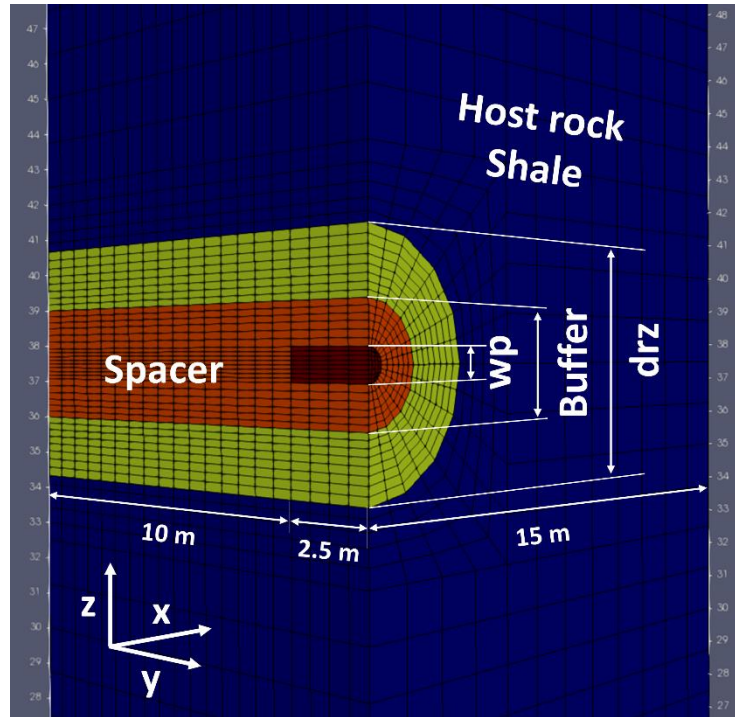


Figure 5-15. Near-field model domain used in PFLOTRAN simulation.

5.2.1 Geomechanical Analysis

Wellbore stability analysis (Zoback, 2007) is applied here for the geomechanical analysis of a cylindrical drift in a deep geologic nuclear waste repository (Figure 5-16). The repository drift can be considered as a horizontal wellbore parallel to the maximum horizontal stress ($S_{H,max}$). When buffer swelling occurs, the swelling stress is assumed to act homogeneously in the radial direction:

$$S_{rr} = \sigma_{swelling} \quad \text{Eq. (1)}$$

where S_{rr} is the radial component of stress and $\sigma_{swelling}$ is the swelling stress exerted by the buffer on the side walls of the drift. The change in the swelling stress, $\Delta\sigma_{swelling}$, is a linear function of the change in average liquid saturation, ΔS_l , within buffer/spacer (Rutqvist et al., 2011):

$$\Delta\sigma_{swelling} = 3K\Delta S_l\beta_{sw}, \quad \text{Eq. (2)}$$

where K is the buffer bulk modulus and β_{sw} is a moisture swelling coefficient, approximately 0.238 for a bentonite buffer material (Rutqvist et al., 2011). The buffer material is required to have high swelling capacity and low hydraulic conductivity to minimize the penetration of ground water

5.2.2 Model Setting

The near-field multi-phase thermal-hydrologic model used in this study is for unsaturated conditions in the buffer, waste package, and DRZ; solute transport is excluded in this study. The domain is discretized such that one quarter of a waste package in the repository system is located at the middle of the domain at depth and on the corner in both lateral dimensions for symmetry across the x - z and y - z planes (Figure 5-15). The whole domain is 15 m (width) \times 12.5 m (length) \times 75 m (height), and includes three concentric sections of waste package, buffer, and DRZ at 0.42 m, 1.5 m, and 3.17 m in radius, respectively, within the shale host rock. The waste package is discretized with 128 grid cells. The simulation was conducted for up to 1000 years.

The near-field model was run for both a 12-PWR and a 24-PWR waste package within a shale host rock in PFLOTRAN GENERAL mode, which solves two-phase (liquid and gas) miscible flow coupled to energy. The material properties are the same as those used in the previous near-field model (Sevougian et al. 2019b), and the two-phase (liquid-gas) flow conditions are added in this study as shown in Table 5-2.

The buffer/spacer are filled with compacted bentonite. The DRZ is defined as the portion of the host rock adjacent to the engineered buffer system that experiences elevated permeability due to mining-induced perturbations in stress state. Initial pressure and temperature throughout the model domain are calculated by applying hydrostatic and geothermal gradients (10 kPa/m and 0.025°C/m, respectively) in the vertical direction assuming temperature of 18°C and atmospheric pressure at the surface (~ 450 m above the top of the model domain). For unsaturated conditions, the initial gas saturation (S_{gi}) is set to 0.35 for the waste package, buffer, and spacer, and 0.1 for the DRZ, while the shale host rock is fully saturated with liquid. The model domain represents a quarter of a tunnel and therefore symmetry boundary conditions are implemented at side boundaries.

Table 5-2. Rock and fluid properties for hydrological characteristics of the near-field model.

	Buffer/Spacer	DRZ	Shale
Porosity [-]	0.35	0.2	0.2
Permeability [m ²]	1 \times 10 ⁻²⁰	1 \times 10 ⁻¹⁸	1 \times 10 ⁻¹⁹
Density [kg/m ³]	2700	2700	2700
Initial gas saturation (S_{gi})	0.35	0.1	0.0
Liquid residual saturation (S_{rl})	0.1	0.1	0.1
Gas residual saturation (S_{rg})	0.1	0.1	0.1
Saturation function	Van Genuchten function*		
alpha [Pa ⁻¹]	6.25 \times 10 ⁻⁸	6.67 \times 10 ⁻⁷	6.67 \times 10 ⁻⁷
m [-]	0.375	0.333	0.333
Liquid relative permeability	Mualem function*		
m [-]	0.375	0.333	0.333
S_{rl} [-]	0.1	0.1	0.1
Gas relative permeability	Mualem function*		
m [-]	0.375	0.333	0.333
S_{rl} [-]	0.1	0.1	0.1
S_{rg} [-]	0.1	0.1	0.1

* Details of van Genuchten saturation function and Mualem relative permeability functions can be found in the following website: <https://www.pflotran.org/documentation>

5.2.3 Preliminary Results

Two different scenarios were modeled to study heat and mass transport in the near-field of a repository in shale host rock: one with a 12-PWR heat source and another with a 24-PWR heat source. The decay heat curves for each heat source are plotted in Figure 5-17 and reflect one quarter of the total amount of heat generated in a waste package because of the quarter symmetry conditions imposed in this conceptual model.

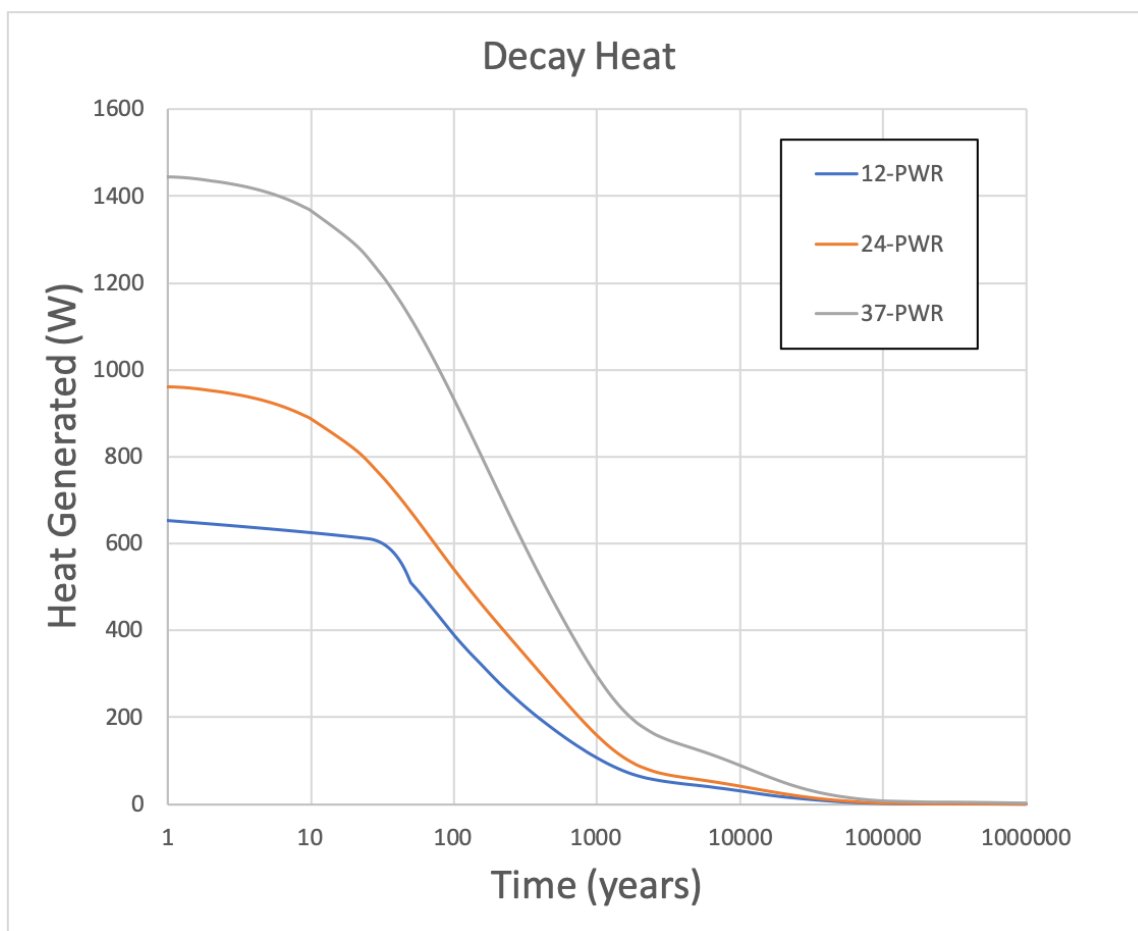


Figure 5-17. Decay heat source terms used as the basis for the near-field simulation ¼ waste package for 12-PWR 100 years OOR (Mariner et al. 2017); 24-PWR 100 years OOR, and 37-PWR (150 years OOR) waste packages (see Section 5.3.1.2).

5.2.3.1 12-PWR Waste Form Results

Figures 5-18, 5-19, and 5-20 show the simulation results of the changes in gas saturation (S_g), liquid pressure (P_l), and temperature (T) for 1000 years. For gas saturation (Figure 5-18), the color bar ranges from 0.0 (blue) to 0.35 (red). The fluids from the shale host rock penetrate into the unsaturated regions (buffer/spacer/DRZ) over time.

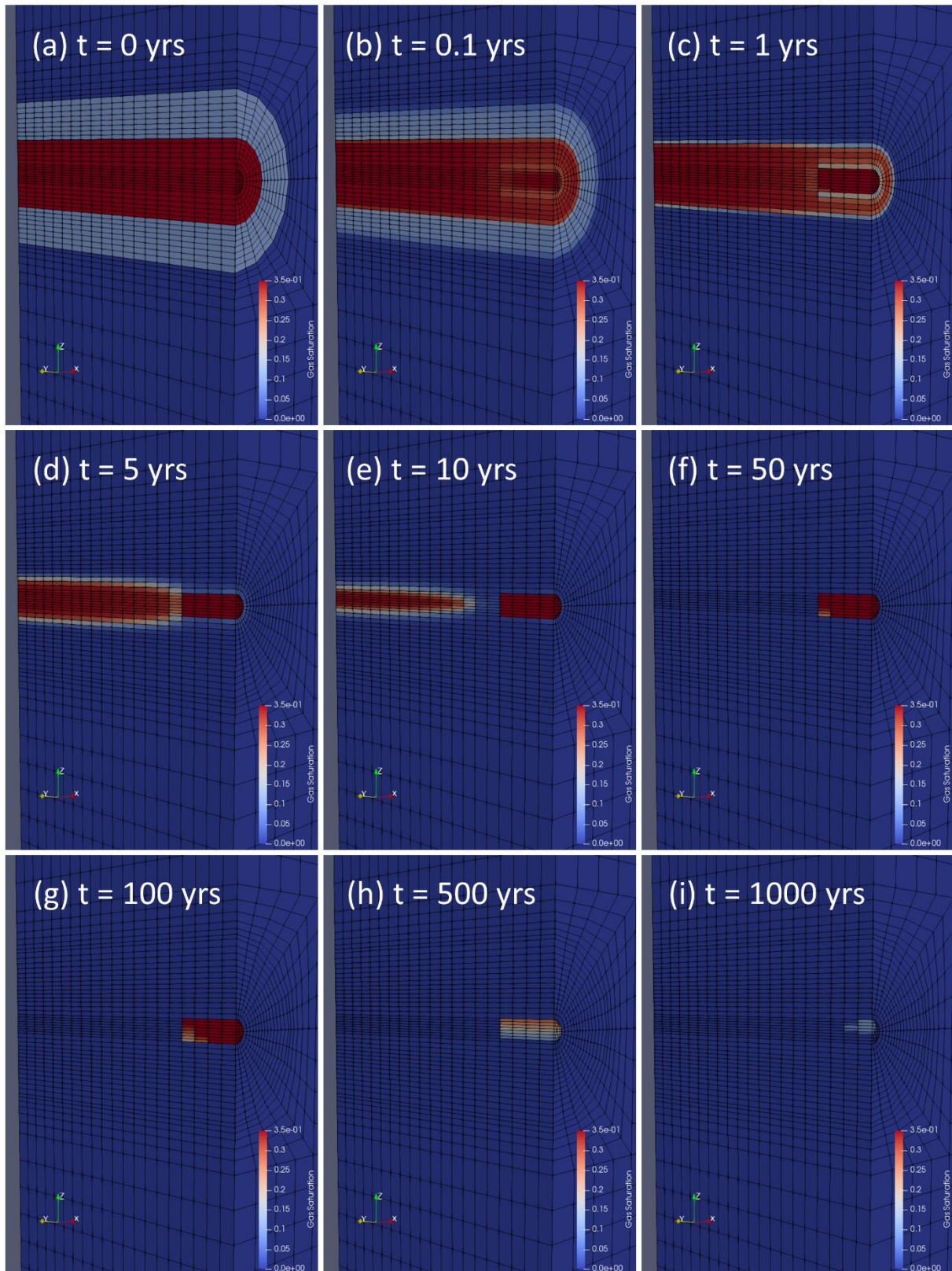


Figure 5-18. Spatio-temporal distribution of gas saturation (S_g) for a 12-PWR heat source.

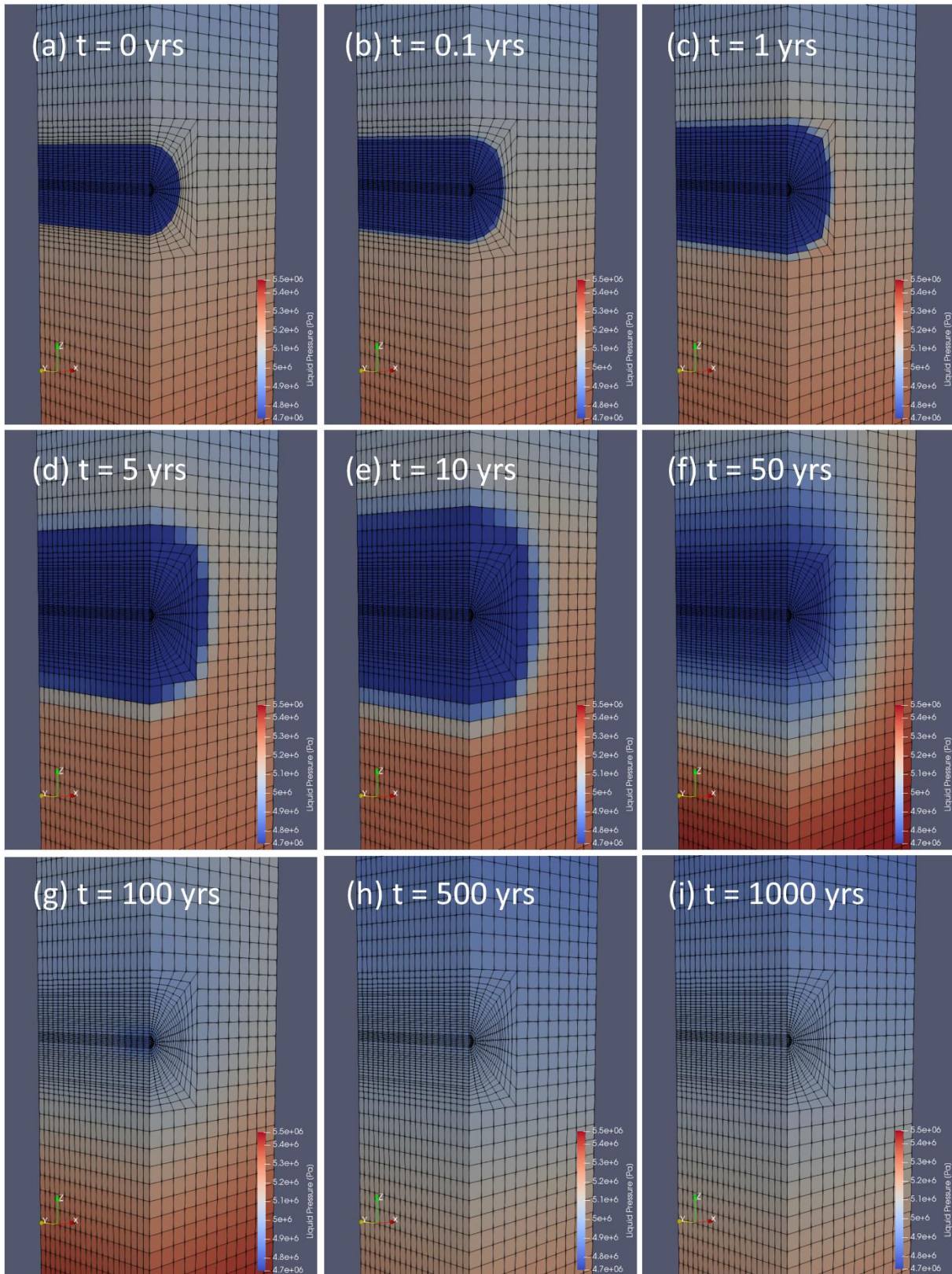


Figure 5-19. Spatio-temporal distribution of liquid pressure (MPa) for a 12-PWR heat source.

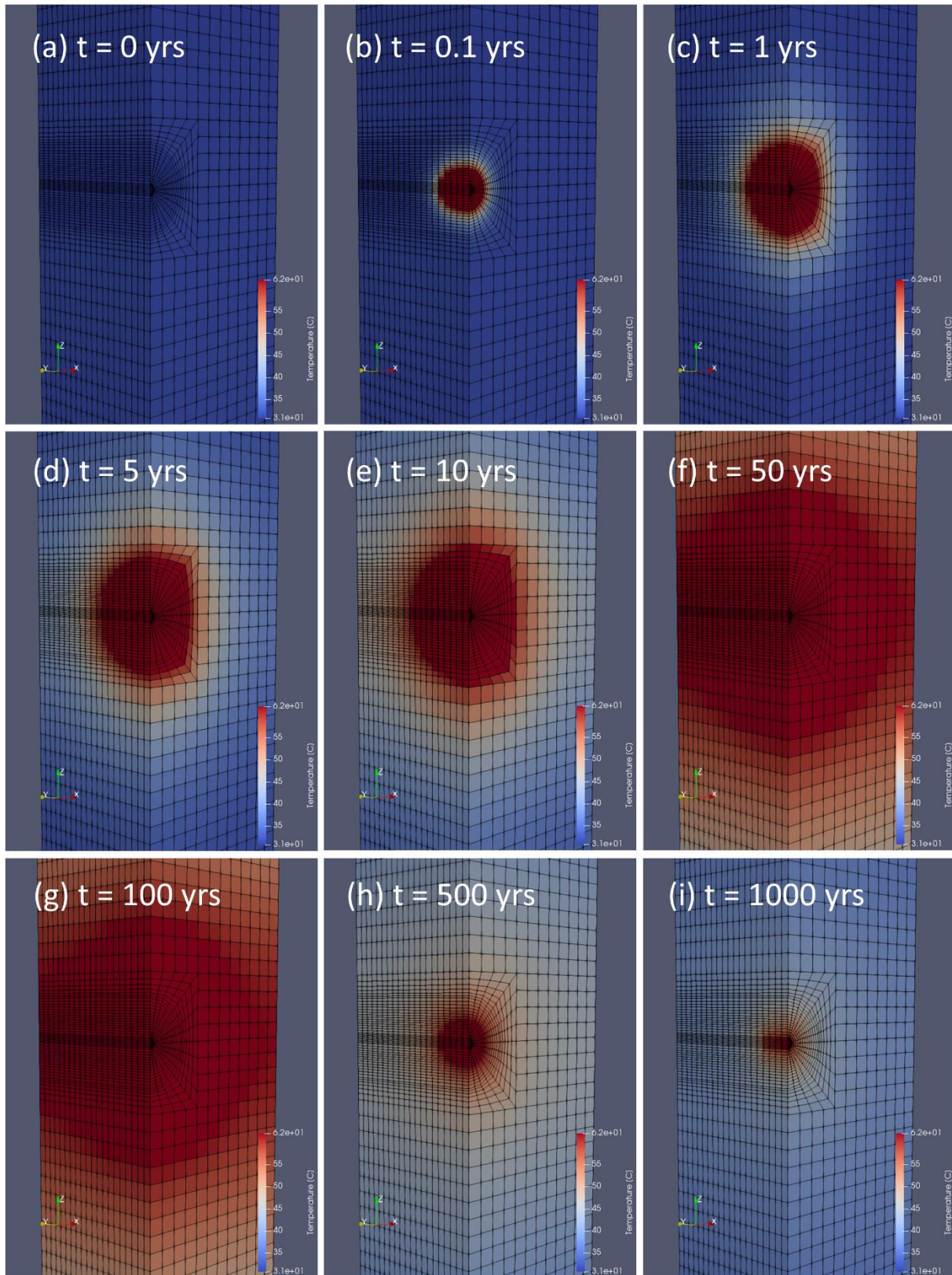


Figure 5-20. Spatio-temporal distribution of temperature (C) for a 12-PWR heat source.

Using simulation results for S_l , P , and T over time, we can calculate the swelling stress ($\sigma_{swelling}$), the poroelastic stress ($\sigma_{h,p}$), and the thermal stress ($\sigma_{h,T}$) as shown in Figure 5-21 based on the parameter values shown in Table 5-3. At time $t = 0$, swelling stress, poroelastic stress, and thermal stress all start at 0 for initial saturation, pressure, and temperature conditions at drift closure (following Rutqvist et al., 2011). To calculate the changes in swelling stress, the liquid saturation is taken as the average over the buffer grid cells at each time step. The pressure and temperature distributions are obtained from the edge of the domain (refer to Figure 5-15).

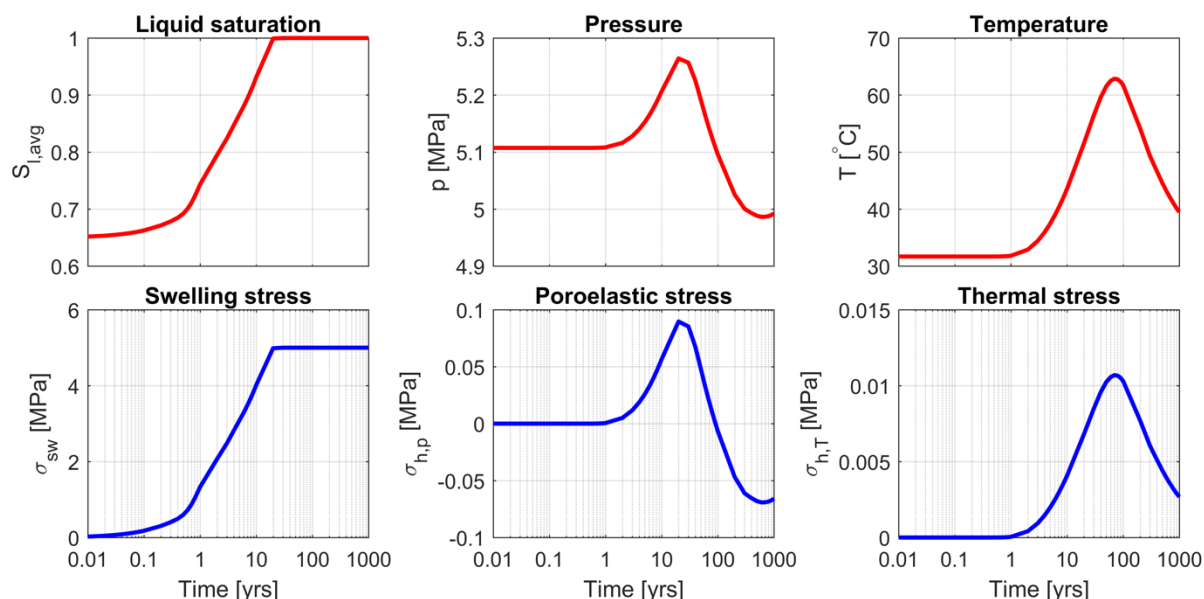


Figure 5-21. Temporal distribution of swelling stress ($\sigma_{swelling}$), poroelastic stress driven by pore pressure change ($\sigma_{h,p}$) and thermal stress due to temperature change ($\sigma_{h,T}$) at the far-field edge of the domain.

Table 5-3. Parameter values used in the preliminary analysis of geomechanical stability of the nuclear waste repository (Rutqvist et al. 2011; Zoback 2007).

Parameter	Value
Biot-Willis coefficient (α) [-]	1
Thermal expansion coefficient (α_T) [1/°C]	1×10^{-5}
Bulk modulus (K) [MPa]	20
Young's modulus (E) [MPa]	24
Poisson's ratio (ν) [-]	0.3

During re-saturation, a swelling buffer exerts stress on the surrounding DRZ, which can in turn work to compress fractures in the DRZ material. As fractures represent high-permeability pathways through the medium, closing them can result in decreased permeability of the DRZ. Therefore, as imbibition and condensation drive an increase in liquid saturation over time in the buffer, permeability of the surrounding DRZ should correspondingly decrease over time. Integrating a relationship between liquid saturation in the buffer and permeability in the DRZ into PFLOTRAN simulations is the subject of ongoing work. An example of DRZ permeability

evolution over time due to buffer re-saturation is given in Figure 5-22. For this calculation, an exponential function relating DRZ permeability to changes in effective stress is used (Chen et al., 2015):

$$k = k_0 e^{-3c_f \Delta \sigma_e} \quad \text{Eq. (6)}$$

where k_0 is the initial DRZ permeability ($1 \times 10^{-18} \text{ m}^2$), c_f is the fracture compressibility (0.263), and $\Delta \sigma_e$ is the change in effective stress on the DRZ; which is computed as the sum of swelling stress in the buffer and poroelastic stress and thermal stress in the host rock (Eq.5).

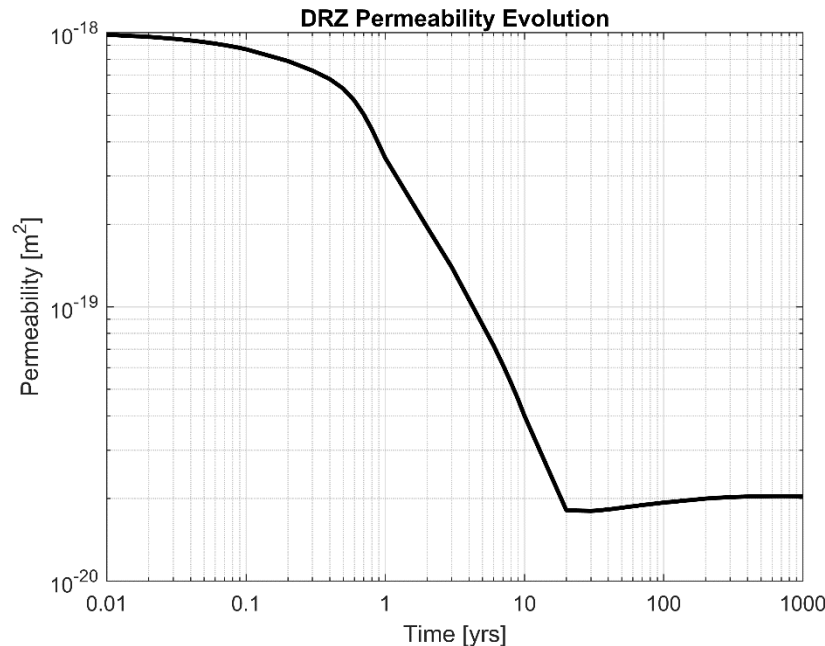


Figure 5-22. Evolution of DRZ permeability over time.

Fracture compressibility exerts a strong control on the evolution of permeability with effective stress, and over large changes in effective stress c_f is not constant (Chen et al., 2015). But over changes in swelling stresses of ~ 5 MPa, c_f can be considered roughly constant. The fracture compressibility chosen here was taken from a silty gas shale (Dong et al., 2010) with comparable initial permeability to the DRZ permeability chosen here. Future work will focus on selecting the best representative fracture compressibility for the DRZ.

It is notable here that this relationship predicts DRZ permeability that drops below the initial permeability of the shale host rock. This behavior is realistic since in addition to fracture closure the DRZ matrix should also compress. Future work will compare this approach to modeling geomechanical behavior of the DRZ with fully coupled THM modeling that includes compressibility both in the DRZ and the shale host rock to assess whether simplifications made here adequately represent near-field phenomena.

5.2.3.2 24-PWR Waste Form Results

In this simulation, physical properties of all materials (waste package, buffer, DRZ, and host rock) are consistent with the 12-PWR simulation. Just as in the 12-PWR simulation, host rock is initially

water-saturated, liquid pressure is set hydrostatically, and temperature is set along a geothermal gradient of 0.025°C with the land surface at a temperature of 18°C and at atmospheric pressure. Initial gas saturation is set to 70% within all materials contained in the repository and in the DRZ (compared to 35% in the 12-PWR case). Initial gas pressure is set to 1.02×10^5 Pa, just above atmospheric pressure, and initial temperature is set to 24°C, which is lower than the host rock at that depth. Finally, a 24-PWR heat source is implemented, which will generally produce a greater thermal load on the system than the 12-PWR waste package heat source (Figure 5-17).

Using a 24-PWR heat source, a greater thermal loading evaporates all of the water at the center of the simulated waste package after 0.2 years (Figure 5-23). Gas saturations at the waste package reach 100% at this time and then remain that way until 200 years simulation time, at which point the heat source has already been declining steadily (Figure 5-17). The decline in the heat source leads to a rapid drop in temperature concurrent with imbibition and condensation of water back into the dried-out region. This process proceeds for another 1400 years until the repository becomes completely saturated with water after about 1600 years simulation time.

The 24-PWR heat source generates peak temperatures of around 150-200°C in the vicinity of the waste package (Figure 5-24), as compared to maximum temperatures of about 60°C in the vicinity of the 12-PWR source (Figure 5-20). Complete evaporation only occurs in the region containing the waste package. The rest of the tunnel experiences net influx of the aqueous phase throughout the duration of the simulation.

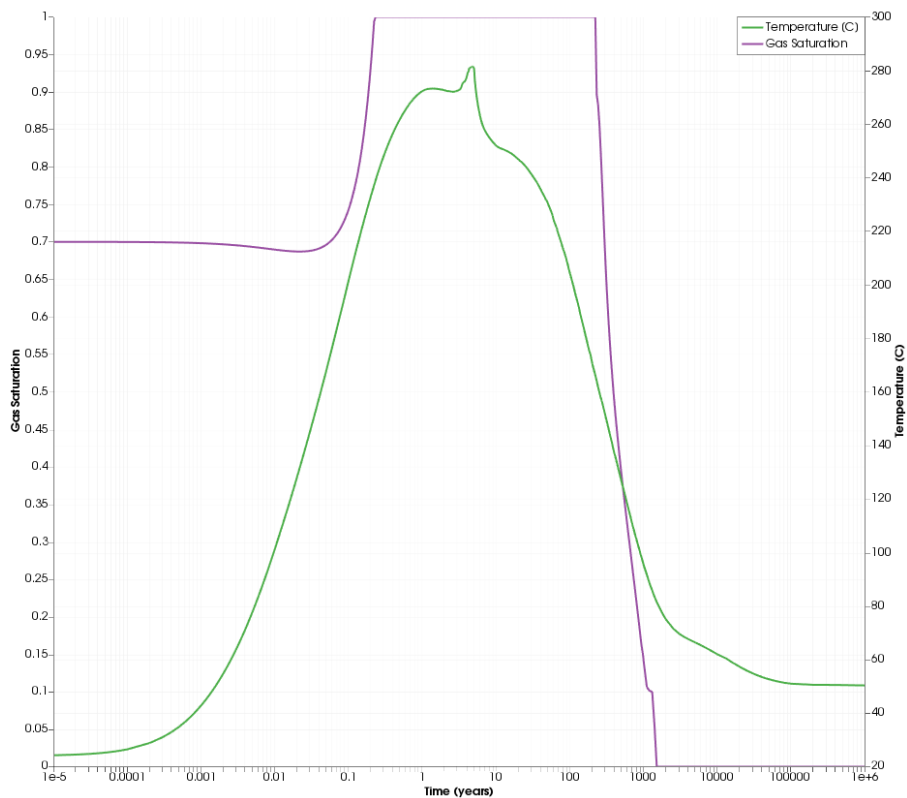


Figure 5-23. Temperature profile and gas saturation at the center of the simulated waste package.

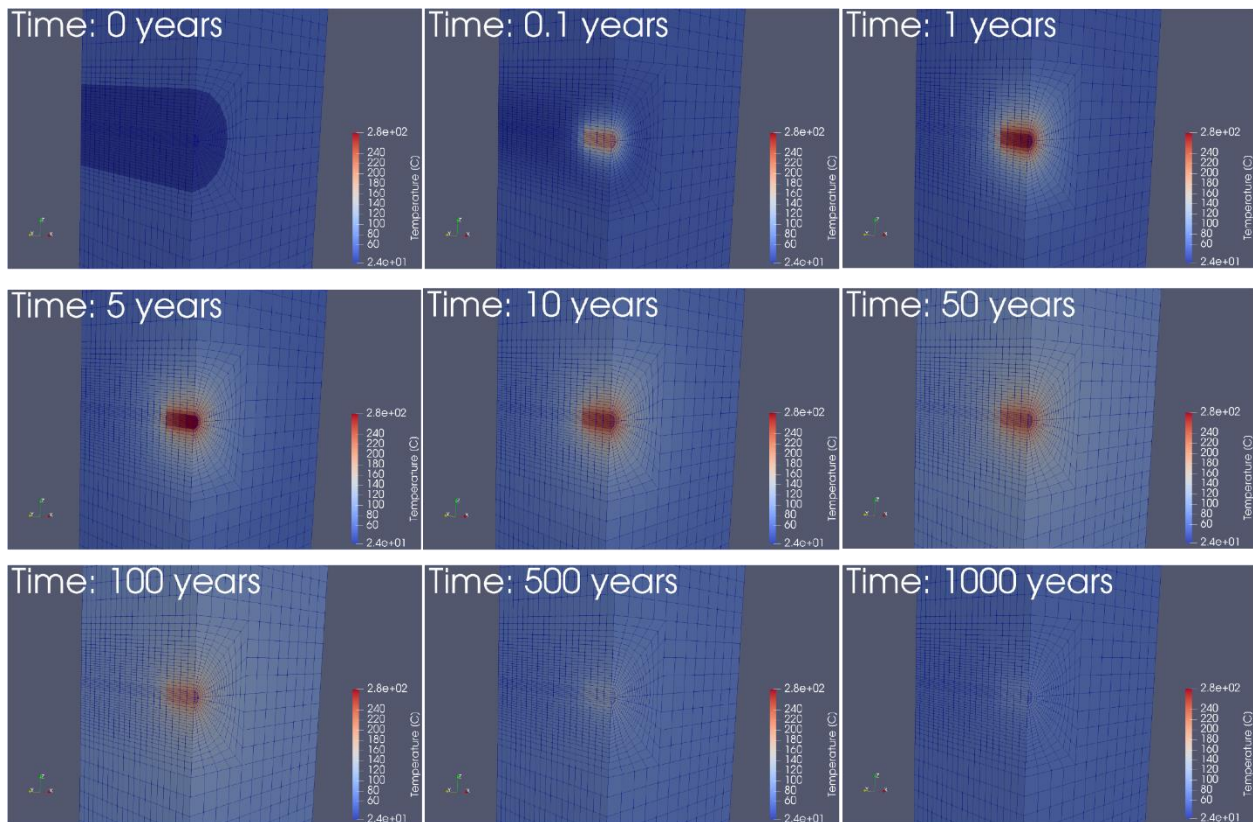


Figure 5-24. Simulation temperature over 1000 years using a 24-PWR heat source.

Just as in the 12-PWR scenario, water infiltrates the repository radially while thermal pressurization near the waste package also pushes water axially away from the waste package. This leads to asymmetric re-saturation of the repository beginning closer to the waste package and then proceeding away from it (Figure 5-25). The trends between both simulations are very similar, only gas saturations are much higher in the 24-PWR simulation scenario—this is likely due in part to higher initial gas saturation in the 24-PWR simulation. Since gas saturations reach a higher peak in the 24-PWR case, it also takes longer for the repository to fully re-saturate with liquid, and therefore longer to reach the maximum swelling stress (see Figure 5-21) that closes the fractures in the DRZ.

Due to high temperatures and high gas saturations experienced in 24-PWR simulations, gas pressure in the waste package reaches nearly 11 MPa (Figure 5-26). Future work will consider the potential effect of high gas pressures on the surrounding host rock, and how thermal conductivity of engineered materials could help to diffuse heat more quickly and avoid buildup of hot steam.

Just as with gas saturation profiles, highest gas pressures are localized at the waste package (Figure 5-27). Gas pressurization extends beyond the vicinity where the domain is entirely gas-saturated, however, which reflects the fact that heat transfer by conduction is outpacing convective flux due to the low permeability of the buffer and host rock. [The grid block at the center of the waste package in Figure 5-27 is completely saturated with water after 1400 years, so gas pressure is no longer relevant at this point and is not plotted.]

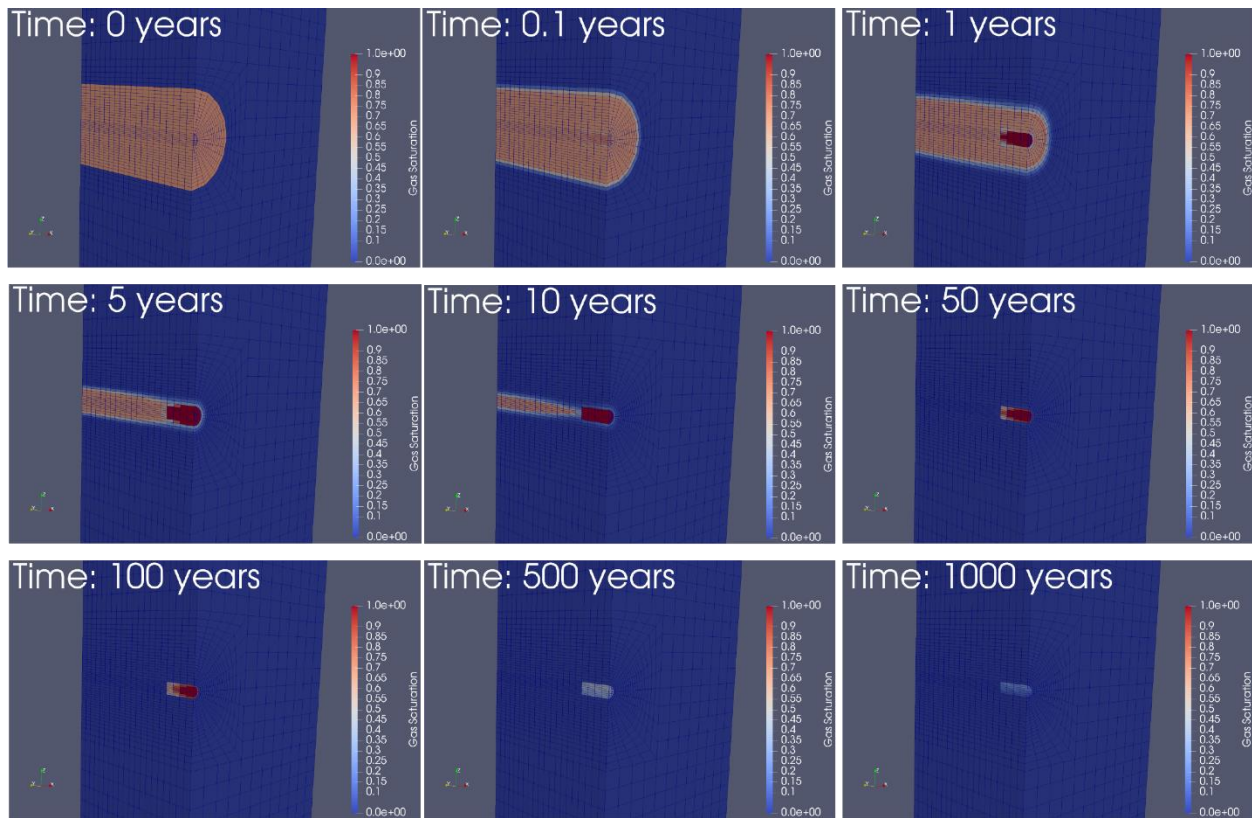


Figure 5-25. Simulated gas saturation throughout the domain over 1000 years for a 24-PWR heat source.

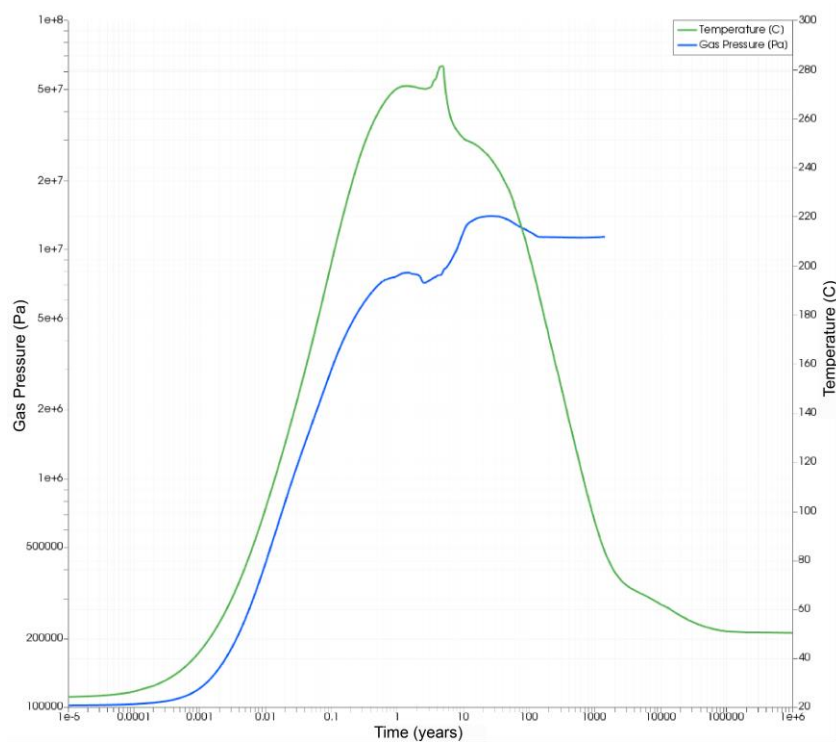


Figure 5-26. Temperature and gas pressure as a function of time at the center of the waste package (edge of the simulation domain) for a 24-PWR waste package.

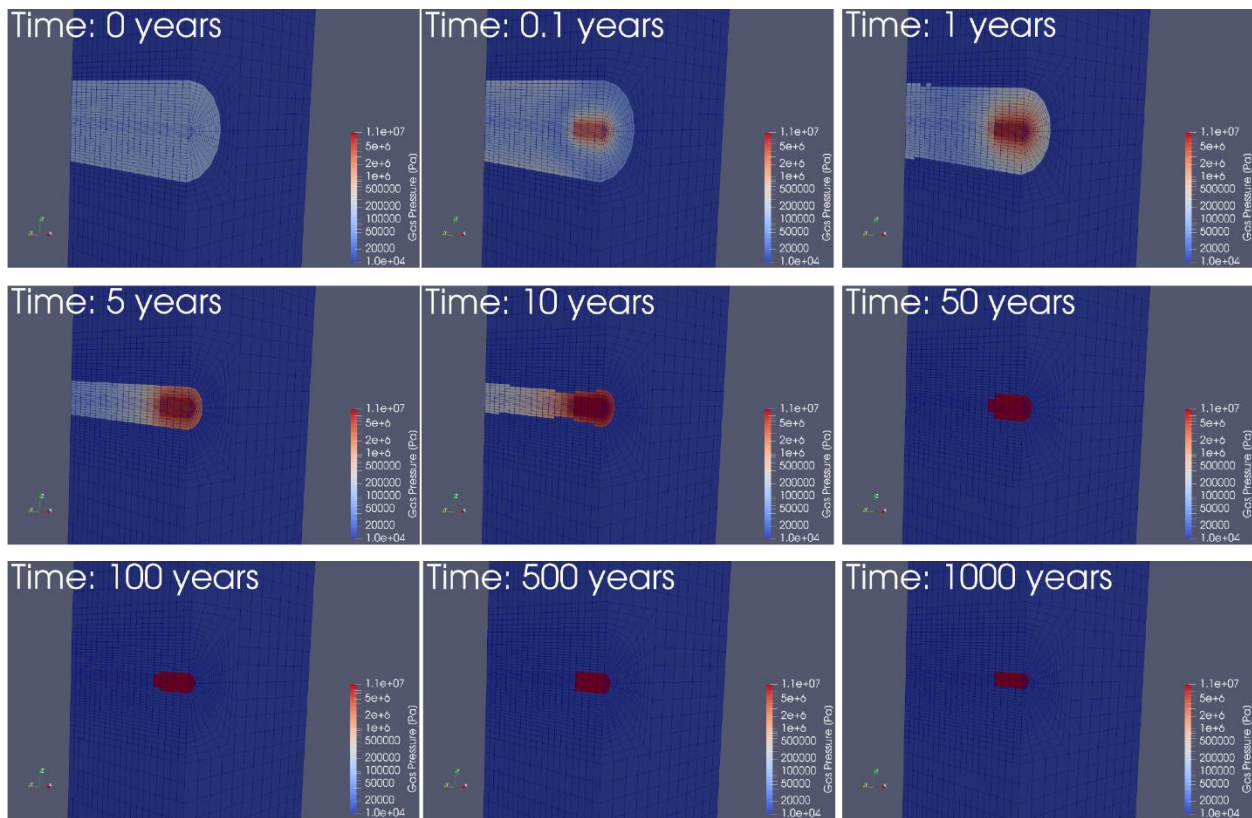


Figure 5-27. Simulated gas pressure profiles over 1000 years for a 24-PWR heat source.

5.2.4 Considerations for Future Work

Perturbations in saturation, temperature and pressure in the near field around the waste packages in a repository drift can affect the mechanical behavior of the surrounding DRZ. Decay heat emitted from waste packages can influence both the near-field buffer re-saturation process and the effective stress in the buffer and DRZ; these processes depend heavily on the waste package thermal loading, which is a function of the waste package assembly. Additionally, when a bentonite buffer material re-saturates with liquid (e.g., Figure 5-18 and Figure 5-25), the material can swell and exert a swelling stress on the DRZ. This swelling stress works to close small fractures in the DRZ that are responsible for its increased permeability relative to the host rock. As these fractures close, the DRZ permeability correspondingly decreases.

Work considering mechanical impacts of temperature and pressure buildup on near-field porosities and permeabilities will continue in FY2020, with a goal of integrating near-field process modeling into *GDSA Framework*.

5.3 Updated Shale Reference Case PA Model and Simulations

Clay-rich sedimentary strata have been considered a potential medium for disposal of radioactive waste in the United States since the forerunner to the DOE introduced a program to develop radioactive waste disposal technology in 1976 (Shurr 1977; Gonzales and Johnson 1985; Rechar et al. 2011). Clay-rich formations are an attractive disposal medium due to their low permeability, high sorption capacity, typically reducing porewaters (which limit radionuclide solubility), and ability to deform plastically, which promotes self-healing of fractures. Clay-rich formations suitable for isolation of radioactive waste span a range of rock types, varying in degree of foliation and degree of consolidation and induration, from unconsolidated mud (such as the Boom Clay) to argillite (such as the Callovo-Oxfordian argillite) (Hansen et al. 2010). For instance, the Glossary of Geology (Jackson 1997) defines mudstone (“an indurated mud having the texture and composition of shale, but lacking its fine lamination or fissility”), claystone (“an indurated rock with >67% clay-sized minerals”), shale (“a laminated, indurated rock with >67% clay-sized minerals”), and argillite (“a compact rock, derived from either mudstone or shale, that has undergone a somewhat higher degree of induration than mudstone or shale but is less clearly laminated than shale and without its fissility, and that lacks the cleavage distinctive of slate”), among others. In this report, we use the term “shale” imprecisely to represent all of the above.

The U.S. hosts several marine sedimentary sequences containing thick beds of clay-rich sediments potentially suitable for deep geologic disposal of radioactive waste (Gonzales and Johnson 1985; Perry et al. 2014; Perry and Kelley 2017). Of these, the Pierre Shale in the northern Great Plains was considered for radioactive waste isolation by Shurr (1977), who lists a number of criteria for assessing the suitability of a shale or similar clay-rich formation for geologic disposal of radioactive waste. The same or similar criteria are considered by later authors (Gonzales and Johnson 1985; Hansen et al. 2010; Perry et al. 2014; Jove Colon et al. 2014; Perry and Kelley 2017) and include:

- Depth – The isolation horizon should be from 300 to 900 m below surface.
- Shale thickness – Maximum thickness of the isolation medium is desired, and a minimum thickness of 150 m is preferred.
- Overburden thickness – Minimal thickness of overlying geologic units is preferred.
- Lithology and mineralogy – The repository interval should be a reasonably uniform shale or other clay-rich unit with few or no interbeds of more permeable lithology.
- Penetrations (boreholes) – Boreholes of any kind are undesirable, particularly if they penetrate to rocks below the disposal horizon. It is recognized that some holes are necessary to provide geologic information at depth.
- Structure – The disposal zone should have nearly horizontal bedding and the surrounding region should be structurally simple (e.g., no folding or faulting).
- Seismicity – Seismically inactive regions are preferred.
- Topography – Minimal topographic relief is desirable to limit the influence of topography on subsurface hydraulic gradients.
- Mineral and water resources – Regions with minimal exploitable mineral and water resources, at or below the surface, are preferred.

Locations of areally extensive shale formations in the U.S. are shown in Figure 5-28.

This section presents status on the FY2019 update to the GDSA Shale Reference Case described in Section 4 of Mariner et. al (2017). The primary new tasks undertaken in FY2019 were:

- (1) Inclusion of 24-PWR and 37-PWR DPC waste packages in the reference case simulations.
- (2) An update to the stratigraphic model for a representative shale domain (Perry et al. 2014; Perry and Kelley 2017)—see Section 5.1 above.
- (3) An update to the numerical model grids and formation properties to incorporate changes to stratigraphy and repository design needed for DPC waste packages.

The remainder of this section includes a current description of the reference engineered barriers (Section 5.3.1) and natural barriers (Section 5.3.2), followed by an update of the generic PA simulations that reflect the impact of direct disposal of the large DPC spent fuel waste packages (Section 5.3.3). Table 5-4 below compares the characteristics of the current updated shale reference case with the reference case presented in 2017.

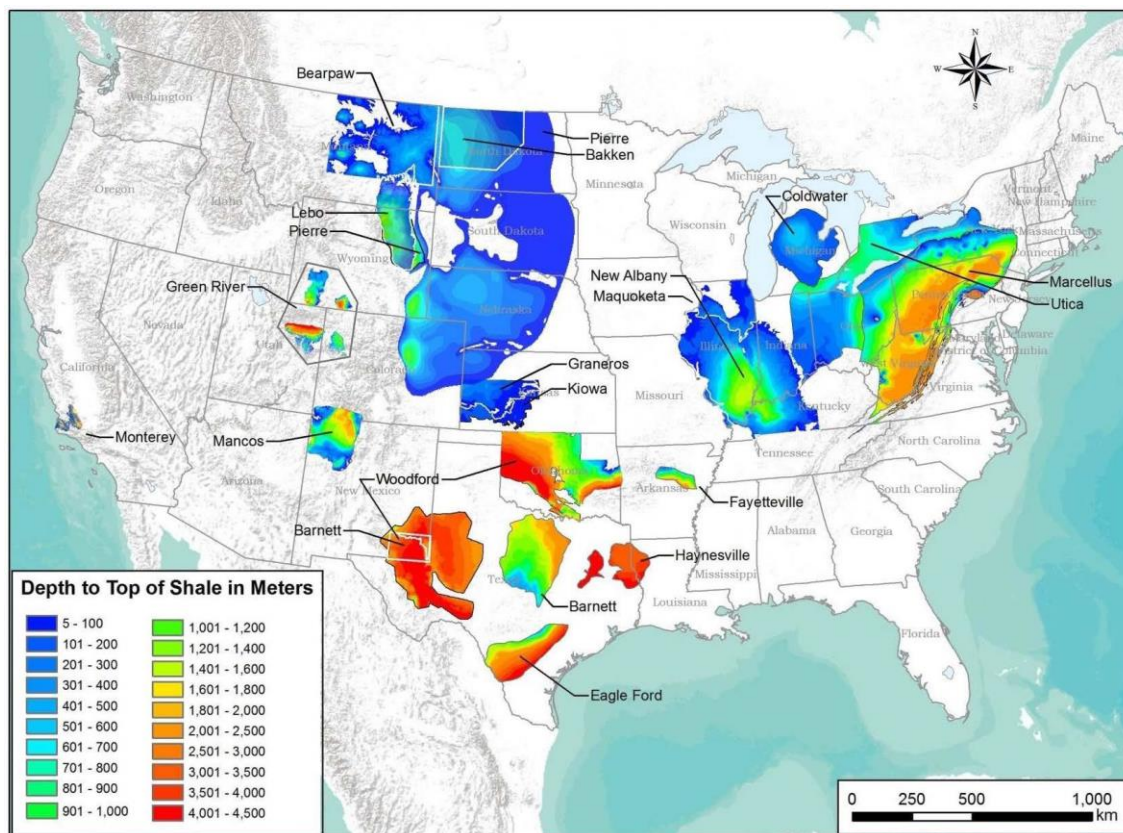


Figure 5-28. Locations of areally extensive shale formations in the U.S. Shale formations of an appropriate depth are the darker shades of blue (Perry et al. 2014; Mariner et.al. 2017, Figure 4-1).

Table 5-4. Comparison of current (2019) GDSA simulations to 2017 shale reference case GDSA simulations. Inventory count (MTHM and number of waste packages) includes *the virtual inventory beyond the reflection boundary condition*.

	2019 GDSA 24-37-PWR	2017 GDSA 12-PWR
Waste Inventory	65,000 MTHM in 3150 24-PWR WPs and 2000 37-PWR WPs	21,000 MTHM in 4200 WPs
Waste Emplacement	In-drift axial emplacement 40-m drift spacing 42 emplacement drifts for 24-PWR 40 emplacement drifts for 37-PWR 20-m center-to-center WP spacing for 24-PWR 30-m center-to-center WP spacing for 37-PWR Bentonite/sand buffer/backfill Additive such as graphite to increase buffer thermal conductivity in 37-PWR disposal drifts	In-drift axial emplacement 84 emplacement drifts 30-m drift spacing 20-m center-to-center WP spacing Bentonite/sand buffer/backfill
Grid	Unstructured 9.9 million cells	Unstructured 7 million cells
Boundary and Initial Conditions	Regional head gradient (0.0013 m/m) Geothermal heat flux (60 mW/m ²) Fully saturated simulation in TH mode Two-phase simulation in GENERAL mode	Regional head gradient (0.0013 m/m) Geothermal heat flux (60 mW/m ²) Fully saturated simulations in TH mode
Natural Barrier	Shale (450 ^a m thick) with silty shale stratum Aquifer above and two below	Shale (585 m thick) with silty shale stratum Aquifer above and two below
Shafts and Seals	4 vertical shafts	4 vertical shafts
Radionuclides	18	18
WP Degradation	WPs breach over time (sampled distribution)	WPs breach over time (sampled distribution)
WF Degradation and Radionuclide Release	Decay in waste form is accounted for in instantaneous releases and in releases due to WF dissolution	Decay in waste form is accounted for in instantaneous releases and in releases due to WF dissolution
Radionuclide Transport	Advection, diffusion, element-based solubility, medium-specific sorption, decay in all phases	Advection, diffusion, element-based solubility, medium-specific sorption, decay in all phases
Biosphere	Not considered	Well water ingestion dose model

^a 450 m shale is from updated stratigraphic model

5.3.1 Engineered Barriers

5.3.1.1 Engineered Barrier Characteristics

The 24- and 37-PWR shale reference case assumes a mined repository located approximately 400 m below land surface, accessed by vertical shafts, and containing 70,000 MTHM of CSNF, 50% of which is in 24-PWR and 50% in 37-PWR DPC waste canisters. The total inventory of MTHM load is consistent with the maximum allowed by the Nuclear Waste Policy Act of 1983.

Assuming 0.435 MTHM/PWR (Sevougian et al. 2013), the half-symmetry model domain contains 16,095 MTHM in 1000 37-PWR waste packages (Table 5-5). These are emplaced in 20 1525-m long emplacement drifts, each containing 50 waste packages emplaced lengthwise and spaced 30

meters center-to-center. Nominal waste package dimensions, including overpack, are 2-m diameter and 5.6-m length (Price et al. 2019). A bentonite seal, approximately 25-m long, is placed at either end of each emplacement drift. Drifts are nominally 4.5 m in diameter; they are spaced 40 meters center-to-center. With the reflection boundary condition, the model simulates 32,190 MTHM in 2000 37-PWR waste packages emplaced in 40 disposal drifts.

The half-symmetry model domain contains 16,443 MTHM in 1575 24-PWR waste packages (Table 5-5) in 21 1525-m long emplacement drifts each containing 75 waste packages spaced 20 meters center-to-center. Waste package dimensions and the dimensions and spacing of the disposal drifts for 24-PWR disposal are the same as those for 37-PWR disposal. With the reflection boundary condition, the model simulates 32,886 MTHM in 3150 24-PWR waste packages emplaced in 42 disposal drifts.

Table 5-5 compares the repository layout of the 24- and 37-PWR reference case to that of the 12-PWR reference case in Mariner et al. (2017). Dimensions are as gridded, e.g., waste package dimensions and drift dimensions are slightly different than nominal assumptions.

Table 5-5. Dimensions and counts for the 24- and 37-PWR repository layout compared to the 12-PWR repository layout (Mariner et al. 2017).

Parameters	2019 GDSA Model Value	2017 GDSA Model Value (12-PWR)
Waste Package (WP)		
WP length (m)	5.00	5.00
WP outer diameter (m)	1.67 (5/3 on a side)	1.67 (5/3 on a side)
WP center-to-center spacing (m)	37-PWR: 30 24-PWR: 20	20
Inventory per WP (MTHM)	37-PWR: 16.1 24-PWR: 10.4	5.225
Number of WPs	37-PWR: 1000/2000 ^a 24-PWR: 1575/3150 ^a	2100/4200 ^a
Emplacement Drift		
Drift diameter (m)	5.0 (on a side)	5.0 (on a side)
Drift center-to-center spacing (m)	40	30
Number of WPs per drift	37-PWR: 50 24-PWR: 75	50
Drift seal length (m)	25	25
Drift length, including seals (m)	1525	1035
Repository		
Repository Depth (m)	405	515
Number of drifts	37-PWR: 20/40 ^a 24-PWR: 21/42 ^a	42/84 ^a
Number of shafts	2/4 ^a	2/4 ^a
Shaft access size (m ²)	5x10	5x10
Emplacement footprint (km ²)	2.4/4.9 ^a	1.3/2.6 ^a

^a Value in half-symmetry domain / Value with reflection

5.3.1.2 Inventory

PA simulations assume that the inventory consists entirely of PWR SNF assemblies, each containing 0.435 MTHM. Half of the inventory is lower burn-up fuel emplaced in 24-PWR waste packages, and half is higher burn-up fuel emplaced in 37-PWR waste packages. Radionuclide inventory at the time of emplacement (Tables 5-6 and 5-7) and heat of decay as a function of time (Figure 5-29) are calculated via decay and ingrowth from the 5-year out of reactor (OoR) radionuclide inventories given by Carter et al. (2013, Table C-1). Calculated values for 24-PWR waste packages assume an initial enrichment of 3.72 wt% 235U, 40 GWd/MTHM burn-up, and 100-year OoR surface storage prior to deep geologic disposal. Calculated values for 37-PWR waste packages assume an initial enrichment of 4.73 wt% 235U, 60 GWd/MTHM burn-up, and 150-year OoR storage. Because the average burn-up of SNF under the “no replacement scenario” is predicted to be only 54 GWd/MTHM (Carter et al. 2013), the assumption of 60 GWd/MTHM results in a conservatively high heat load for the 37-PWR waste packages.

Table 5-6. 24-PWR SNF inventory (40 GWd/MTHM burnup, 100-year OoR) of selected radionuclides for the shale reference case.

Isotope	Inventory (g/MTHM) ¹	Inventory (g/g waste) ²	Atomic weight (g/mol) ³	Approximate Decay Constant (1/s) ⁴
²⁴¹ Am	1.35E+03	9.36E-04	241.06	5.08E-11
²⁴³ Am	1.38E+02	9.61E-05	243.06	2.98E-12
²³⁸ Pu	1.79E+02	1.24E-04	238.05	2.56E-10
²³⁹ Pu	6.38E+03	4.43E-03	239.05	9.01E-13
²⁴⁰ Pu	2.57E+03	1.79E-03	240.05	3.34E-12
²⁴² Pu	5.65E+02	3.92E-04	242.06	5.80E-14
²³⁷ Np	7.60E+02	5.28E-04	237.05	1.03E-14
²³³ U	1.32E-02	9.18E-09	233.04	1.38E-13
²³⁴ U	2.66E+02	1.85E-04	234.04	8.90E-14
²³⁶ U	4.72E+03	3.28E-03	236.05	9.20E-16
²³⁸ U	9.33E+05	6.48E-01	238.05	4.87E-18
²²⁹ Th	2.90E-06	2.01E-12	229.03	2.78E-12
²³⁰ Th	3.34E-02	2.32E-08	230.03	2.75E-13
²²⁶ Ra	7.34E-06	5.1E-12	226.03	1.37E-11
³⁶ Cl	3.52E-01	2.44E-07	35.97	7.30E-14
⁹⁹ Tc	9.16E+02	6.36E-04	98.91	1.04E-13
¹²⁹ I	2.16E+02	1.5E-04	128.9	1.29E-15
¹³⁵ Cs	4.86E+02	3.37E-04	134.91	9.55E-15

¹ Calculated from Carter et al. (2013, Table C-1)

² (g isotope/g waste) = (g isotope/MTHM)/(g waste/MTHM), where g waste = g all isotopes

³ Weast and Astle (1981)

⁴ Decay constants from ORIGEN (Croff 1983)

Table 5-7. 37-PWR SNF inventory (60 GWd/MTHM burn-up, 150-year OoR) of selected radionuclides for the shale reference case.

Isotope	Inventory (g/MTHM) ¹	Inventory (g/g waste) ²	Atomic weight (g/mol) ³	Approximate Decay Constant (1/s) ⁴
²⁴¹ Am	1.36E+03	9.42E-04	241.06	5.08E-11
²⁴³ Am	2.67E+02	1.86E-04	243.06	2.98E-12
²³⁸ Pu	1.91E+02	1.33E-04	238.05	2.56E-10
²³⁹ Pu	7.39E+03	5.14E-03	239.05	9.01E-13
²⁴⁰ Pu	4.09E+03	2.84E-03	240.05	3.34E-12
²⁴² Pu	8.17E+02	5.67E-04	242.06	5.80E-14
²³⁷ Np	1.51E+03	1.05E-03	237.05	1.03E-14
²³³ U	6.64E-02	4.61E-08	233.04	1.38E-13
²³⁴ U	6.02E+02	4.18E-04	234.04	8.90E-14
²³⁶ U	6.29E+03	4.37E-03	236.05	9.20E-16
²³⁸ U	9.10E+05	6.32E-01	238.05	4.87E-18
²²⁹ Th	2.65E-05	1.84E-11	229.03	2.78E-12
²³⁰ Th	1.82E-01	1.26E-07	230.03	2.75E-13
²²⁶ Ra	1.01E-04	7.04E-11	226.03	1.37E-11
³⁶ Cl	5.01E-01	3.48E-07	35.97	7.30E-14
⁹⁹ Tc	1.28E+03	8.89E-04	98.91	1.04E-13
¹²⁹ I	3.13E+02	2.17E-04	128.9	1.29E-15
¹³⁵ Cs	7.72E+02	5.36E-04	134.91	9.55E-15

¹ Calculated from Carter et al. (2013, Table C-1)

² (g isotope/g waste) = (g isotope/MTHM)/(g waste/MTHM), where g waste = g all isotopes

³ Weast and Astle (1981)

⁴ Decay constants from ORIGEN (Croff 1983)

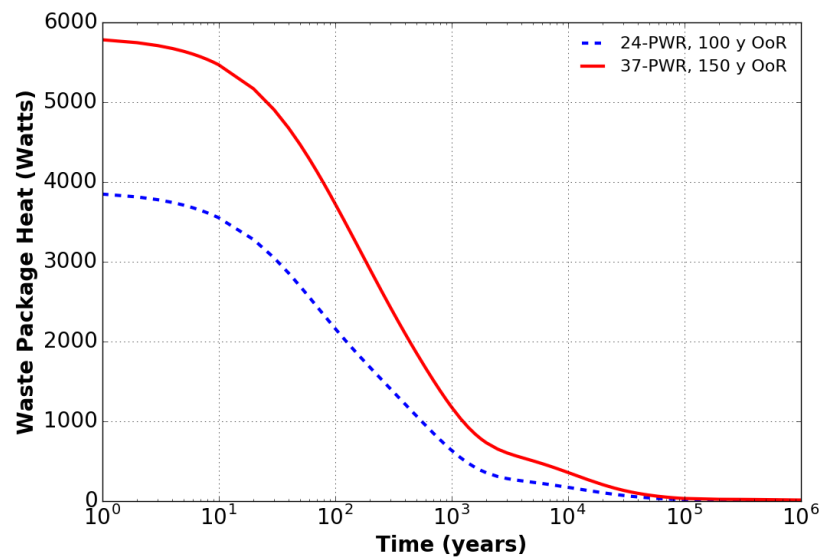


Figure 5-29. Waste package heat source terms for the shale reference case.

5.3.1.3 Waste Form

The waste form is spent uranium oxide (UO₂) fuel, a polycrystalline ceramic material stable to high temperatures and likely slow to degrade in the disposal environment (Mariner et al. (2017, Section 4.1.3). Fission products are assumed to concentrate in voids of the waste form, resulting in two radionuclide release fractions: instant-release (upon waste package breach) and slow-release (according to the UO₂ matrix dissolution rate (Mariner et al. 2017; Mariner et al. 2016, Section 3.2.2).

5.3.1.4 Waste Package

The 2019 shale reference case considers two DPC waste package configurations: a 24-PWR waste package and a 37-PWR waste package. Both are assumed to consist of a stainless-steel canister and a stainless steel overpack. The waste package is 5.6 meters in length with a diameter of 2 m (Price et al. 2019). Due to gridding considerations, the size of simulated waste packages is $1.67 \times 1.67 \times 5 \text{ m}^3$, which is slightly smaller in volume than waste packages are expected to be.

Waste package porosity is set equal to the fraction of void space within the waste package, which is set at 50% (Mariner et al. 2016). Permeability is set several orders of magnitude higher than that of the surrounding materials, so that flow through waste packages is uninhibited. The waste package is given the thermal properties of stainless steel (Shelton 1934).

The shale reference case uses a temperature-dependent waste-package degradation rate with a truncated log normal distribution. The degradation rate distribution is such that 50% of the waste packages breach within a few tens of thousands of years (Mariner et al. 2017, Section 4.1.4). See Section 6.3.3.6 below for additional information.

5.3.1.5 Bentonite Buffer

The bentonite buffer described in Mariner et al. (2017, Section 4.1.3) has been modified for 2019 as appropriate for disposal of generic DPC waste packages and inventory (Sec. 5.3.1.2). The reference case assumes horizontal, in-drift emplacement with 24- and 37-PWR waste packages elevated on plinths of compacted bentonite and drifts buffered and filled with compacted bentonite pellets and/or bricks in a single layer as shown in Figure 5-30. For simplicity, PA simulations assume that access drift and shafts are filled with compacted bentonite buffer; see the next section for a brief discussion of other materials likely to be used in these areas.

Compacted bentonite has low permeability, high sorption capacity, and may be engineered to achieve desirable thermal properties; for instance, quartz sand or graphite can be added to increase thermal conductivity (Choi and Choi 2008; Jobmann and Buntebarth 2009; Wang et al. 2015). The current set of simulations employs a buffer material with properties appropriate for a compacted mixture of 70% bentonite and 30% quartz sand in the 24-PWR disposal drifts and access hallways, and a buffer with a higher thermal conductivity, such as could be achieved through the addition of 15% graphite, in the 37-PWR disposal drifts. Both buffer materials are assigned a porosity of 0.35 (Liu et al. 2016) and a permeability of 10^{-20} m^2 (Liu et al. 2016). The bentonite/sand buffer has a water-saturated thermal conductivity of 1.5 W/m/K (Wang et al. 2015), and a dry thermal conductivity of 0.6 W/m/K. The bentonite/graphite buffer has a water-saturated thermal conductivity of 3.0 W/m/K and a dry thermal conductivity of 1.9 W/m/K (see Jobmann and Buntebarth 2009, Figure 8).

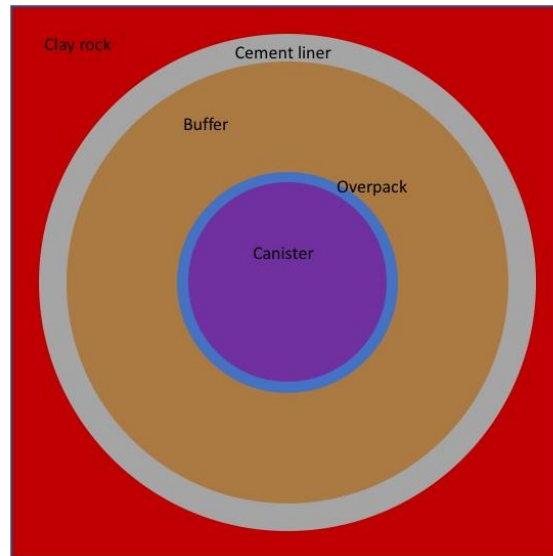


Figure 5-30. Schematic cross-section of a single-layer buffer in a 24- or 37-PWR disposal drift of a generic shale repository.

5.3.1.6 Other Materials

As in Mariner et al. (2017, Section 4.1.3), this reference case assumes that engineered materials in a shale repository would include shotcrete or cement liners for ground support in disposal drifts and other tunnels, seals of compacted bentonite supported by cement plugs at ends of disposal drifts, within shafts, and possibly at intervals within disposal and/or access drifts. Access drifts and shafts except where sealed may be filled with crushed rock backfill rather than compacted bentonite.

Shotcrete, cement, and backfill materials are not simulated in the current PA.

5.3.2 Geosphere/Natural Barriers

5.3.2.1 Natural Barrier Characteristics

The natural barrier system (NBS) comprises the shale formation hosting the repository, the disturbed rock zone (DRZ) adjacent to the repository, and geologic formations above and below the host formation. For the 24- and 37-PWR shale reference case, the NBS concept is derived from the GFM presented in Section 5.1 the primary stratigraphic units of which are summarized in Table 5-1. The generic stratigraphic column in Figure 5-31 consists of (from the bottom up): a 645 m thickness of undifferentiated shales interrupted by a 45-m thick sandstone aquifer; a 45-m thick limestone with relatively high permeability; a 450-m thickness of sealing shale (the host rock) including a 45 m thickness of a silty shale unit; and a 60-m thick sandstone aquifer at the top of the model domain. Layer thicknesses and material properties loosely correspond to the units described in Section 5.1. The generic stratigraphic column and the rock properties described in the following sections are consistent with those used in previous models of generic shale repositories (see Mariner et al. 2017, Section 4.2).

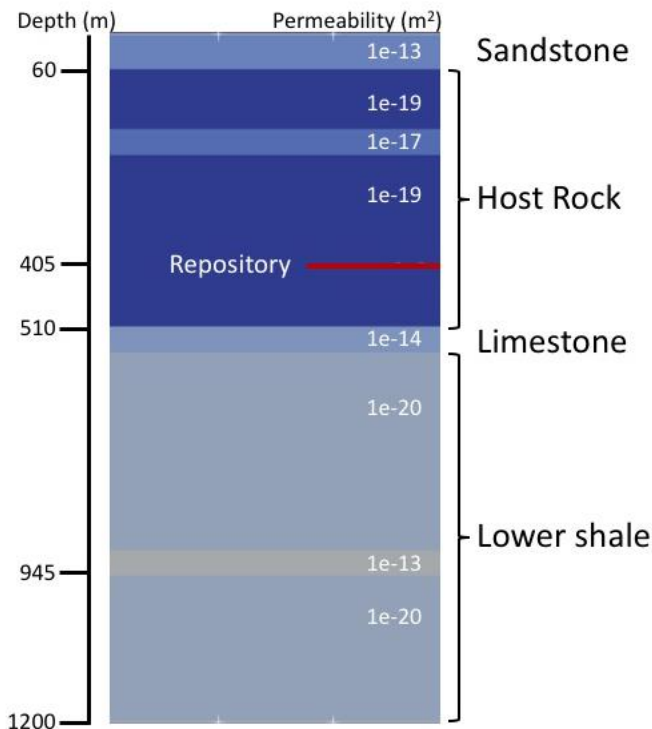


Figure 5-31. Generic stratigraphic column for shale reference case simulations.

5.3.2.2 Shale Host Rock

Consistent with the description of the Pierre Shale in Table 5-1 and the description of the shale host rock in the previous 12-PWR reference case (Mariner et al. 2017, Section 4.2.2), the current reference case assumes that the shale host rock has a permeability of 10^{-19} m², a porosity of 0.2, and a liquid-saturated thermal conductivity of 1.2 W/m/K. A dry thermal conductivity of 0.6 W/m/K is assumed. Tortuosity (τ), a measure of the tortuous path length through a porous medium that contributes to calculation of the effective diffusion coefficient (see Sevougian et al. 2016, Appendix B), is calculated as a function of porosity using the relationship derived for the Opalinus Clay by Van Loon and Mibus (2015): $\tau = \phi^{1.4}$.

5.3.2.3 Disturbed Rock Zone (DRZ)

The DRZ is defined as the portion of the host rock adjacent to the engineered barrier system that experiences durable (but not necessarily permanent) changes due to the presence of the repository (Freeze et al. 2013b). The DRZ is expected to have elevated permeability with respect to the permeability of the host rock matrix for some period of time due to the changes in stress induced by mining. Although fractures in a sealing shale (see Mariner et al. 2017, Section 4.2.2) are likely to close within decades, PA simulations assume elevated permeability in the DRZ for the one-million-year duration of the simulations. It is assumed that the permeability of the DRZ (10^{-18} m²) is 10 times that of the undisturbed host rock, and that differences in other material properties are negligible.

As in the 12-PWR model domain, the thickness of the DRZ surrounding the emplacement drifts is equal to one third the width of the drift, or 1.67 m. The thickness of the DRZ surrounding access

drifts and shafts (which are gridded at a coarser resolution) is equal to the width of the access drift (5 m).

5.3.2.4 Lower Shale

The lower shale is analogous to the undifferentiated Cretaceous and older shales in Table 5-1. A higher-permeability, 45-m thickness of sandstone interrupts it. As indicated in Table 5-1, the stratigraphy of such a thickness is expected to be considerably more complex than that represented here.

As in Mariner et al. (2017), the current reference case assumes the lower shale has experienced greater consolidation and induration than the host rock shale, assigning it a porosity of 0.1 (half that listed in Table 5-1) and a permeability of 10^{-20} m². Thermal properties are identical to those of the host rock shale. Tortuosity is calculated as a function of porosity using the same relationship used for the host rock shale.

5.3.2.5 Lower Sandstone Aquifer

The lower sandstone aquifer (45-m thick) is modeled after the Inyan Kara Group (Table 5-1) which occupies a similar stratigraphic position and has similar hydrologic properties to the Dakota Sandstone, the basis for the lower sandstone aquifer in the 12-PWR reference case.

As in Mariner et al. (2017, Section 4.2.5), the lower sandstone aquifer has a porosity of 0.2, a permeability of 10^{-13} m² and a saturated thermal conductivity of 3.1 W/m/K. Tortuosity is calculated as a function of porosity using the relationship derived by Millington (1959) for spherical particles: $\tau = \phi^{1/3}$.

5.3.2.6 Limestone

The limestone formation (45-m thick) is conceptualized as a fractured unit of relatively higher permeability, similar in nature to the Niobrara Formation (Table 5-1 and Mariner et al. 2017, Section 4.2.6).

As in Mariner et al. (2017), the current reference case assumes that the limestone has a porosity of 0.1 (lower than that indicated in Table 5-1), a permeability of 10^{-14} m² and a saturated thermal conductivity of 2.6 W/m/K. Tortuosity is calculated as a function of porosity using the same relationship used for the host rock shale.

5.3.2.7 Silty Shale

The silty shale unit (45-m thick) within the shale host rock represents some of the vertical heterogeneity that could be encountered in a thick marine shale.

As in Mariner et al. (2017, Section 4.2.7), the reference case assumes properties for the silty shale between those of sandstone and shale, including a porosity of 0.2, a permeability of 10^{-17} m², and a saturated thermal conductivity of 1.4 W/m/K (Forster and Merriam 1997). Tortuosity is calculated as a function of porosity using the same relationship used for the host rock shale.

A 5-m thick DRZ surrounds each shaft in the silty shale. The permeability of the silty shale DRZ is 10^{-16} m².

5.3.2.8 Upper Sandstone Aquifer

The upper sandstone aquifer is the release pathway to the biosphere. The 60-m thickness at the top of the model domain is modeled on the Fox Hills Sandstone, a heterogeneous unit comprised of sandstone, shale, and siltstone (Section 5.1).

Ignoring the likely heterogeneous nature of the upper sandstone aquifer, the reference case assumes properties similar to those of the lower sandstone aquifer, including a porosity of 0.2, a horizontal permeability of 10^{-13} m^2 and a saturated thermal conductivity of 3.1 W/m/K. Tortuosity is calculated as a function of porosity using the relationship derived by Millington (1959) for spherical particles: $\tau = \phi^{1/3}$.

A 5-m thick DRZ surrounds each shaft in the upper sandstone aquifer. The permeability of the sandstone DRZ is 10^{-12} m^2 .

5.3.2.9 Chemical Environment

Assumptions about the chemical environment, including pore fluid chemistry, elemental solubility, and sorption are described in Mariner et al. (2017, Section 4.2.10). Tables of solubility limits and linear distribution coefficients (K_{ds}) appearing in Mariner et al. (2017) are reproduced below (Table 5-8 and Table 5-9).

Table 5-8. Element solubility limits for clay reference case (Clayton et al. 2011, Table 3.3-23).

Element	Solubility Limit (mol/L)
Am	4×10^{-7}
Pu	2×10^{-7}
Np	4×10^{-9}
U	7×10^{-7}
Th	6×10^{-7}
Ra	1×10^{-7}
Cl	Infinitely Soluble
Tc	4×10^{-9}
I	Infinitely Soluble
Cs	Infinitely Soluble

5.3.3 Post-Closure Performance Assessment

5.3.3.1 Conceptual Model

As in the 2017 Shale Reference Case, the conceptual the components of the repository system are the engineered barrier, the natural barrier, and the biosphere in the undisturbed scenario. The characteristics of and processes occurring in key components of each system are summarized in Table 5-10 from Mariner et al. (2017, Table 4-8). The biosphere is not modeled in the 2019 update because its characteristics are site-specific, and calculation of dose is not necessary for analysis of generic repository reference cases. As in previous GDSA reference case simulations, the primary performance metric is maximum radionuclide concentration rather than dose (Mariner et al., 2015; 2016; 2017; Sevougian et al. 2016).

Table 5-9. Linear distribution coefficients (K_d) for clay reference case elements.

Element	Shale K_d^a (mL/g)	Buffer K_d^b (mL/g)	Aquifer K_d^c (mL/g)
Am	50,000	12,000	89.4
Pu	900	1000	447
Np	900	1000	14.1
U	8000	100,000	0.775
Th	8000	3000	2646
Ra	1000	1000	Non-adsorbing
Cl	Non-adsorbing	Non-adsorbing	Non-adsorbing
Tc	1150	114,000	50 ^d
I	Non-adsorbing	Non-adsorbing	Non-adsorbing
Cs	400	380	500 ^d

^a Clayton et al. (2011) Table 3.3-23^b Clayton et al. (2011) Table 3.3-19^c Log-scale average of minimum and maximum values in Clayton et al. (2011) Table 3.1-9^d Mode of triangular distribution in Clayton et al. (2011) Table 3.1-9

Simulations assume (1) a mined repository at 405 m depth; (2) a head gradient of -0.0013 m/m from west to east; and (3) a regional heat flux of 60 mW/m² and a mean annual surface temperature of 10°C . The head gradient is the same as that applied in previous reference case simulations of repositories in shale, crystalline, and salt host rocks (Mariner et al. 2015; 2016; 2017; Sevougian et al. 2016), and consistent with gradients estimated for deep sedimentary basins (e.g., Downey and Dinwiddie, 1988); it is about half that estimated (in Section 5.1) on the basis of dips associated with the Black Hills uplift.

Table 5-10. Conceptual representation of key components in PA.

Region	Component	Key characteristics	Key processes included in PA
Engineered Barrier	Waste Form	Commercial SNF (UO ₂)	Radionuclide decay, instant release fraction, waste form dissolution
	Waste Package	Stainless steel	Degradation and breach
	Bentonite Buffer	Low permeability, high sorption capacity	Radionuclide advection, diffusion, sorption, decay
Natural Barrier	Shale Host Rock	Low permeability, high sorption capacity	Radionuclide advection, diffusion, sorption, decay
	DRZ	Enhanced permeability	Radionuclide advection, diffusion, sorption, decay
	Upper Sandstone Aquifer	High permeability, potable water	Radionuclide advection, diffusion, sorption, decay
Biosphere	Site-specific	Site-specific	Site-specific

Processes accounted for in the conceptual model include waste package degradation, waste form (UO₂) dissolution, equilibrium-controlled radionuclide sorption and precipitation/dissolution, radioactive decay and ingrowth in all phases (aqueous, adsorbed, precipitate), coupled heat and fluid flow, and radionuclide transport via advection and diffusion. Mechanical dispersion is conservatively neglected, because including it would result in earlier arrival of radionuclides at

observation points, but lower peak concentrations than reported here (Mariner et al. 2017, Section 4.4.1).

Two deterministic simulations were run, one using PFLOTRAN's TH mode (single-phase flow plus energy) and the other using GENERAL mode (miscible two-phase flow plus energy).

5.3.3.2 Model Domain and Discretization

The half-symmetry model domain, shown in Figure 5-32, is 2055 m in width (Y), 1200 m in height (Z), and 7215 m in length (X). The domain is long enough to place an observation point 5000 m down-gradient of the repository (X direction). Most of the domain is discretized into cells 15 m on a side; the volume of the repository is discretized into cells 5 m on a side; and emplacement drifts are discretized into cells 1.67 m (5/3 m) on a side. The numerical grid contains 9,888,556 cells, of which approximately 4.6 million are the smaller cells in and around the repository. The grid was generated using Cubit (Blacker et al. 2016). Figure 5-33 shows an XY slice through the repository at its Z -midpoint. See Table 5-5 for more details of the repository layout.

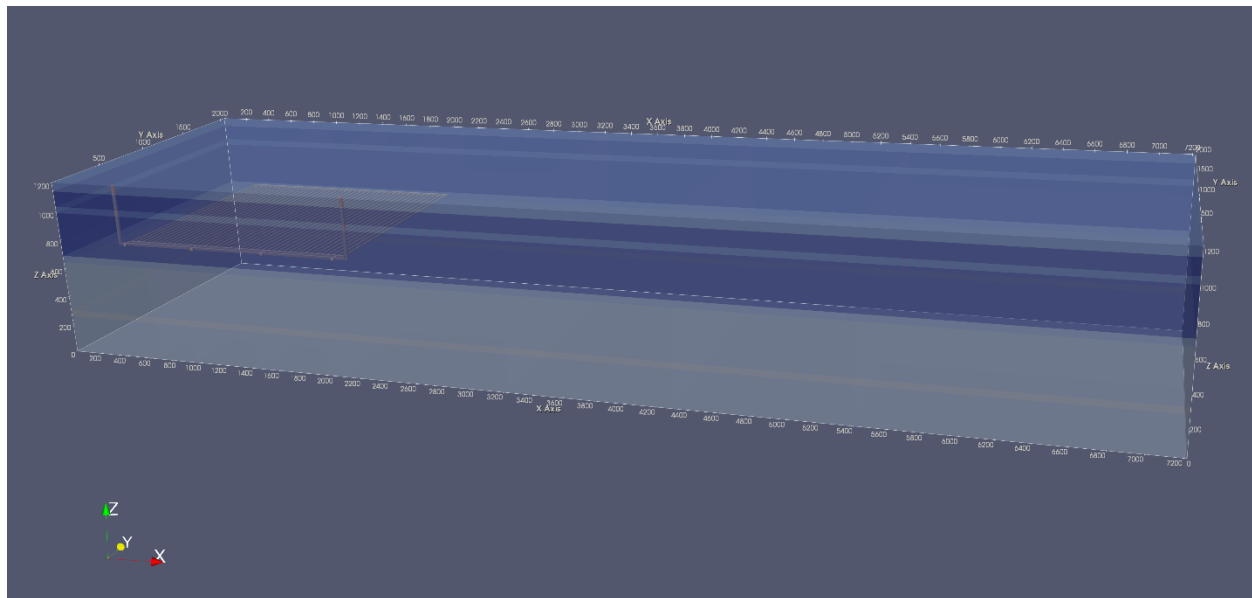


Figure 5-32. Transparent view of the 24- and 37-PWR model domain colored by material. The repository (red) is 500 m from the west (left) face of the domain and 405 m below the top face of the domain. 40-m long hallways connect the disposal panel to the south (front) face of the domain, which is a reflection boundary. Shades of blue correspond to the stratigraphic column in Figure 5-31.

5.3.3.3 Initial Conditions

Initial conditions specified are liquid pressure (or gas pressure and gas saturation in the GENERAL mode simulation), temperature, and radionuclide concentrations. Initial pressures and temperatures throughout the model domain are calculated by applying a liquid flux of 0 m/s and an energy flux of 60 mW/m^2 to the base of the domain and holding temperature (10°C) and pressure (approximately atmospheric) constant at the top of the domain, and allowing the simulation to run to 10^6 years. Pressure at the top of the domain decreases from west (left) to east (right) with a head gradient of -0.0013 (m/m) . This technique results in initial conditions that represent a geothermal temperature gradient and hydrostatic pressure gradient in the vertical direction, and a horizontal pressure gradient that drives flow from west to east. In the GENERAL mode simulation, partially-

saturated initial conditions (gas pressure = 101325 Pa and gas saturation = 0.7) are applied in the disposal drifts, hallways, and shafts. Simulations include the 18 radionuclides listed in Tables 5-6 and 5-7; initial concentrations of all radionuclides in all cells are 10^{-21} mol/L.

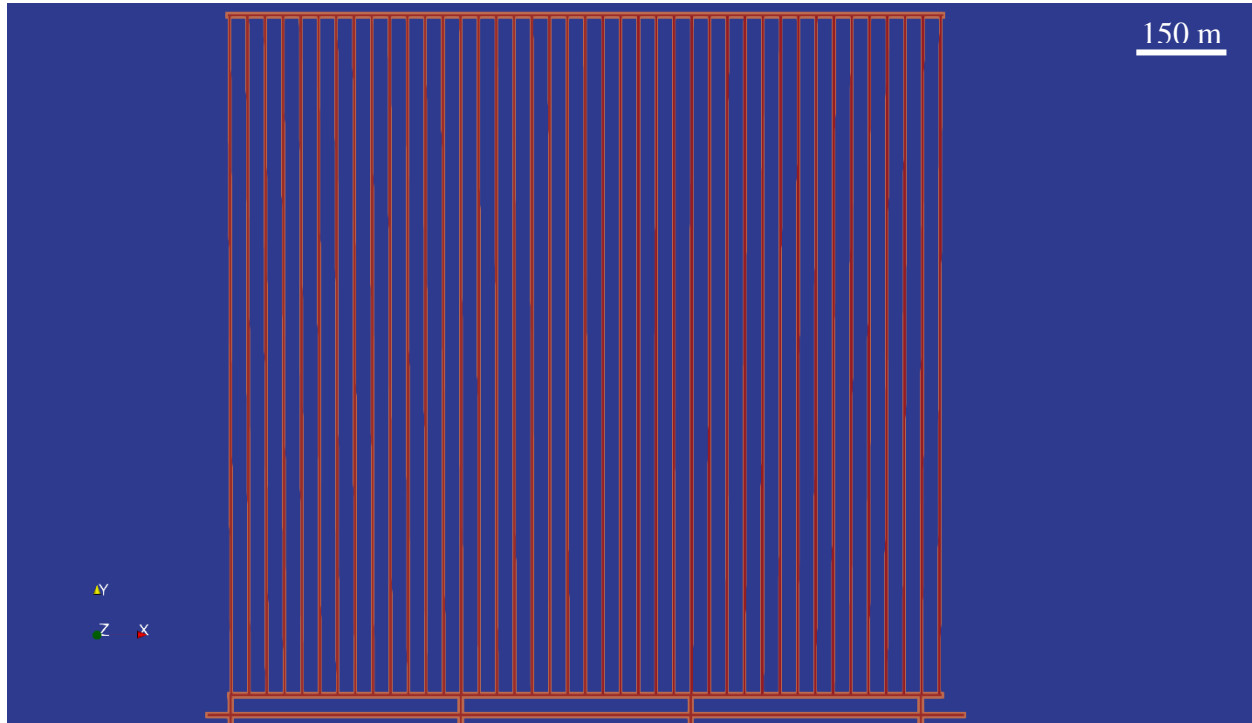


Figure 5-33. XY slice through the repository colored by material: blue, host rock; orange, DRZ; shades of red, buffer and waste packages, which cannot be distinguished from each other at this scale. The base of the figure is the south face of the model domain, which is a reflection boundary. A vertical shaft is gridded at either end of the southern-most hall, which is approximately 1685 m long.

5.3.3.4 *Boundary Conditions*

Boundary conditions must be set for the six faces of the model domain. Fluxes of heat, fluid, and solute are set to zero at the south face of the model domain, creating a reflection boundary and virtually doubling the volume of the model domain. At all other faces, initial pressures and temperatures are held constant. Radionuclide concentrations are held constant at 10^{-21} mol/L at the upstream boundary of the model domain for each radionuclide, and a zero concentration gradient is applied at the outflow boundaries.

5.3.3.5 *Waste Package Heat Sources*

Each waste package is modeled as a transient heat source. The energy (watts per waste package) entering the model domain is updated periodically according to values in a lookup table. At the beginning of the simulation the heat output of a 24-PWR waste package is 3881 W, and that of a 37-PWR waste package is 5817 (Figure 5-29). Between times specified in the lookup table, the energy input is linearly interpolated.

5.3.3.6 Waste Package Breach and Radionuclide Source Term

The waste package degradation model implemented in PFLOTRAN (Mariner et al. 2016, Section 4.3.2.5) calculates normalized remaining canister thickness (or fractional thickness) at each time step as a function of a base canister degradation rate, a canister material constant, and temperature. Waste package breach occurs when this fractional thickness reaches zero. Deterministic simulations assign a base canister degradation rate for each waste package by sampling on a truncated log normal distribution with a mean of $10^{-4.5}/\text{yr}$, a standard deviation of 0.5 (log units) and an upper truncation of -3.5 (log units). Probabilistic simulations sample on the mean degradation rate using a log uniform distribution from $10^{-5.5}/\text{yr}$ to $10^{-4.5}/\text{yr}$. The mean and standard deviation parameter values used in these simulations are placeholders used to approximate the conceptual timeline for waste package failure as presented in Wang et al. (2014, Figure 2-19), where the waste package failure period extends from $10^{-4.3}$ to $10^{-6.5}$ yr, while also including heterogeneity across waste packages.

PFLOTRAN calculates the decayed radionuclide inventory in each waste package region at each time step. From the time of waste package breach, the waste form releases radionuclides in two fractions: instant-release and slow-release. The instant-release fraction is due to the accumulation of certain fission products in void spaces of the waste form and occurs at the time of waste package breach. The shale reference case assumes a non-zero instant-release fraction for ^{135}Cs , ^{129}I , ^{99}Tc , and ^{36}Cl (Table 5-11), and zero for all other radionuclides in the simulations. The slow-release fraction is due to fuel matrix (UO_2) dissolution, which is modeled using a fractional dissolution rate of $10^{-7}/\text{yr}$ starting from the time of waste package breach. This rate is the mode of a log triangular distribution (Table 5-12) appropriate for fuel 3,000 to 10,000 years OoR and strongly reducing conditions (SKB 2006; Ollila 2008); for a complete discussion refer to Sassani et al. (2016, Section 3.2.1). Probabilistic simulations sample on the waste-form dissolution rate over the range $10^{-8}/\text{yr}$ to $10^{-6}/\text{yr}$ but simplify the distribution to log uniform rather than log triangular. This distribution is identical to that used in the most recent generic crystalline repository PA (Mariner et al. 2016).

Table 5-11. Isotope instant release fractions recommended by Sassani et al. (2012) for PWR with 60 GWd/MTHM burn-up.

Isotope	Instant Release Fraction
^{135}Cs	0.1
^{129}I	0.1
^{99}Tc	0.07
^{36}Cl	0.05

Table 5-12. SNF dissolution rates; log triangular distribution from cited SKB (2006) in Sassani et al. (2016, Section 3.2.1)

Parameter	Rate (yr^{-1})	Time to 50% dissolution (yr)	Time to 99% dissolution (yr)
Min	10^{-8}	6.93×10^7	4.61×10^8
Mode	10^{-7}	6.93×10^6	4.61×10^7
Max	10^{-6}	6.93×10^5	4.61×10^6

5.3.3.7 Material Properties

Material properties are discussed in Sections 5.3.1 and 5.3.2; values used in simulations are summarized in Table 5-13.

Table 5-13. Parameter values used in deterministic simulations.

Model Region	Permeability (m ²)	Porosity, ϕ	τ	Effective Diffusion Coefficient ¹ (m ² /s)	Saturated Thermal Conductivity (W/m/K)	Dry Thermal Conductivity (W/m/K)
Upper Sandstone ³	1×10^{-13}	0.20	0.58	1.2×10^{-10}	3.1	n/a
Host Rock Shale ²	1×10^{-19}	0.20	0.11	2.2×10^{-11}	1.2	0.6
Silty Shale ²	1×10^{-17}	0.20	0.11	2.2×10^{-11}	1.4	n/a
Limestone ²	1×10^{-14}	0.10	0.04	4.0×10^{-12}	2.6	n/a
Lower Shale ²	1×10^{-20}	0.10	0.04	4.0×10^{-12}	1.2	n/a
Lower Sandstone ³	1×10^{-13}	0.20	0.58	1.2×10^{-10}	3.1	n/a
24-PWR Buffer ²	1×10^{-20}	0.35	0.23	8.1×10^{-11}	1.5	0.6
37-PWR Buffer ²	1×10^{-20}	0.35	0.23	8.1×10^{-11}	3.0	1.9
Waste Package	1×10^{-16}	0.50	1	5×10^{-10}	16.7	16.7

¹ Effective diffusion coefficient = $D_w \phi \tau s$, where the free water diffusion coefficient (D_w) = 1×10^{-9} m²/s (Li and Gregory 1974) and saturation (s) = 1

² $\tau = \phi^{1.4}$ (Van Loon and Mibus 2015)

³ $\tau = \phi^{1/3}$ (Millington 1959)

5.3.3.8 Deterministic Simulation Results

Results are discussed in terms of concentrations of the long-lived radionuclides ¹²⁹I ($t_{1/2} = 1.57 \times 10^7$ yr), ³⁶Cl ($t_{1/2} = 3.01 \times 10^5$ yr) and ²³⁷Np ($t_{1/2} = 2.14 \times 10^6$ yr). ¹²⁹I and ³⁶Cl are assumed to have unlimited solubility and to be non-adsorbing. ²³⁷Np is solubility-limited and adsorbing. Temperatures and saturations in 24-PWR and 37-PWR disposal drifts and waste package breach times are also presented.

5.3.3.8.1 Near Field Conditions

Simulations in TH mode (single-phase, saturated) and GENERAL mode (two-phase, unsaturated initial conditions) predict peak temperatures less than 190°C at the center of 24-PWR and 37-PWR waste packages (Figure 5-34). In all cases, peak temperatures are reached within the first 30 years of the simulation. In the TH mode simulation, the 24-PWR reaches a maximum temperature of 183°C at 27 yr, and the 37-PWR reaches a maximum temperature of 177°C at 14 yr (Table 5-14). Peak temperatures are a 3 to 6 degrees higher in the GENERAL mode simulation, in which the 24-PWR reaches a peak temperature of 186°C at 3 yr; and the 37-PWR reaches a peak temperature of 183°C at 16 yr. These slight differences in behavior can be ascribed to differences in thermal conductivity. The unsaturated buffer materials in the GENERAL mode simulation have lower thermal conductivity than the saturated buffer materials in the TH mode simulation, resulting in higher peak temperatures, and in the case of the 24-PWR, an earlier peak temperature. Because

the buffer material in the 37-PWR disposal drifts has higher thermal conductivity than in the 24-PWR disposal drift, maximum temperatures are similar between the two, despite the difference in heat load.

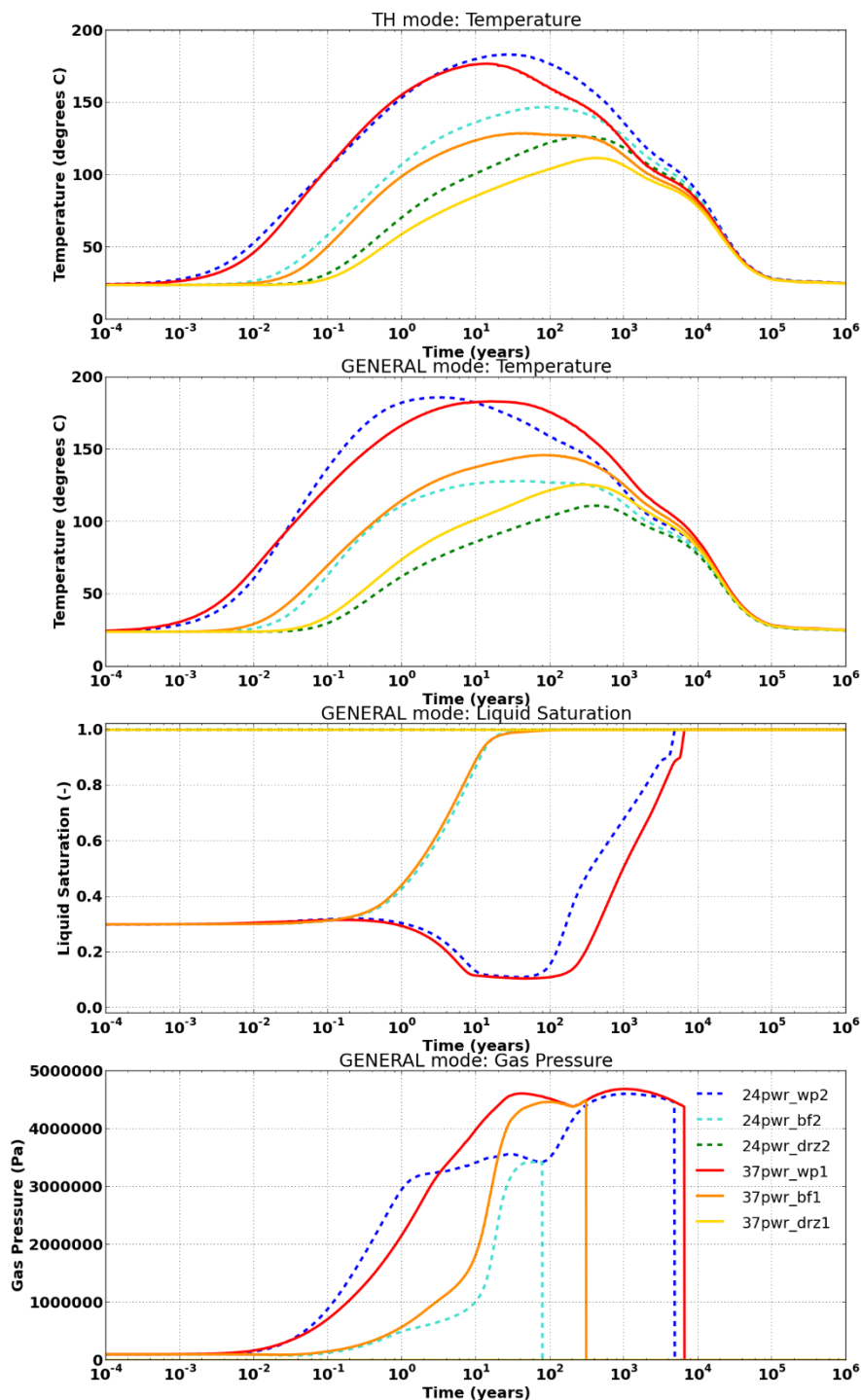


Figure 5-34. In-drift temperature (TH mode) and temperature, liquid saturation, and gas pressure (GENERAL mode) at interior 24-PWR and 37-PWR waste packages. Dashed lines (blue, turquoise and green) are 24-PWR waste package, buffer, and DRZ. Solid lines (red, orange, and yellow) are 37-PWR waste package, buffer, and DRZ. Gas pressure is zero where liquid saturation is one.

Table 5-14. Time to reach maximum waste package temperature.

	Time (y)	Max T (°C)
TH mode, 24-PWR	27	183
TH mode, 37-PWR	14	177
GENERAL mode, 24-PWR	3	186
GENERAL mode, 37-PWR	16	183

In the GENERAL mode simulation, the liquid saturation at the DRZ observation point never drops below 1.0, the buffer adjacent to the 24-PWR waste package reaches a liquid saturation of 1.0 at 78 years, and the buffer adjacent to the 37-PWR waste package reaches a liquid saturation of 1.0 at 308 years. Gas pressures increase from the initial condition of atmospheric pressure (101325 Pa) to a maximum of 4.7 MPa (in the 37-PWR) before complete saturation of the waste package grid cells occurs.

5.3.3.8.2 Waste Package Breach

Figure 5-35 shows the waste package failure histories for PFLOTRAN TH mode versus PFLOTRAN GENERAL model. The differences between the two modes are minor because of the similarity in temperature histories shown in Figure 5-34. [See Mariner et al. (2016, Sec. 3.2.1) for the temperature dependency of the waste package corrosion rate.]

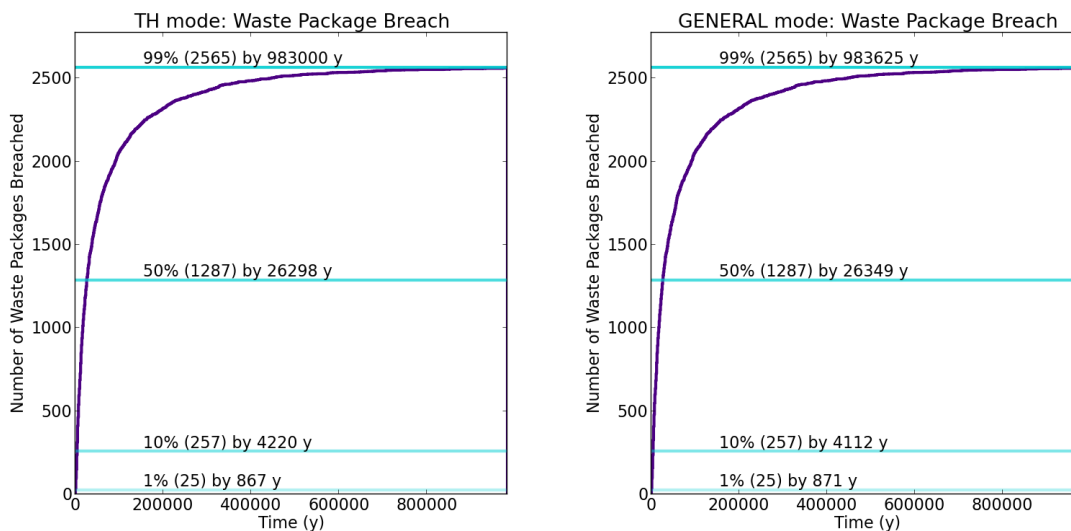


Figure 5-35. Cumulative number of waste packages breached versus time in TH mode (left) and GENERAL mode (right) simulations.

5.3.3.8.3 ^{129}I Transport

^{129}I transport away from the repository is diffusive within the host rock and begins when the earliest waste packages breach. At 1000 years, less than 50 waste packages have breached, and ^{129}I is confined to the immediate vicinity of the breached waste packages (Figure 5-36). At 10,000 years, fewer than 50% of the waste packages have breached, and ^{129}I remains confined to the near field (Figure 5-37). By 100,000 years, ^{129}I has reached the limestone formation, 110 m beneath the

repository, at 10^{-15} M concentrations, but not the upper sandstone aquifer (Figure 5-38). By 1,000,000 years, ^{129}I has reached the upper sandstone aquifer, 340 m above the repository, at 10^{-15} M concentrations, and has advected to the downstream end of the model domain, just over 5 km beyond the edge of the repository (Figure 5-39).

Concentrations of ^{129}I at three observation points in the upper sandstone aquifer were monitored. Observation points are approximately 30, 2500, and 5000 m downgradient of the repository (Figure 5-40). ^{129}I concentration at these three points are plotted as time histories in Figure 5-41 for simulations using both the PFLOTRAN TH mode and the PFLOTRAN GENERAL model. The difference in the solution between these two modes is negligible, as would be expected from examining the tiny difference in waste package failure times in Figure 5-35. This small difference in the waste package failure distribution between TH and GENERAL models is expected because of the similar waste package temperature histories shown in Figure 5-34.

Compared to the GENERAL mode simulation, the TH mode simulation required about 75% less time to solve for flow (1.15 hours compared to 4.48 hours). The reason for this is two-fold. First, TH mode is solving for two state variables, rather than three, making the time required for solution of each timestep in TH mode less than that of GENERAL mode (2.8 sec/timestep versus 5.4 sec/timestep). Second, the GENERAL mode solution requires more timesteps than the TH mode solution at early times to model resaturation of the repository. The GENERAL mode solution required 2994 timesteps in the flow solver, 1326 of which occurred in reaching 1000-year simulation time. The TH mode simulation required 1458 timesteps, 374 of which occurred in reaching 1000-year simulation time. This comparison suggests that an appropriate balance of computational efficiency and mechanistic flow modeling could be obtained by coupling a GENERAL mode problem of limited size and duration to a TH mode problem of larger size and million-year duration. Limiting the size of the GENERAL mode problem domain would decrease the computational cost of each timestep, while limiting the length of the GENERAL mode problem would decrease the total number of timesteps required.

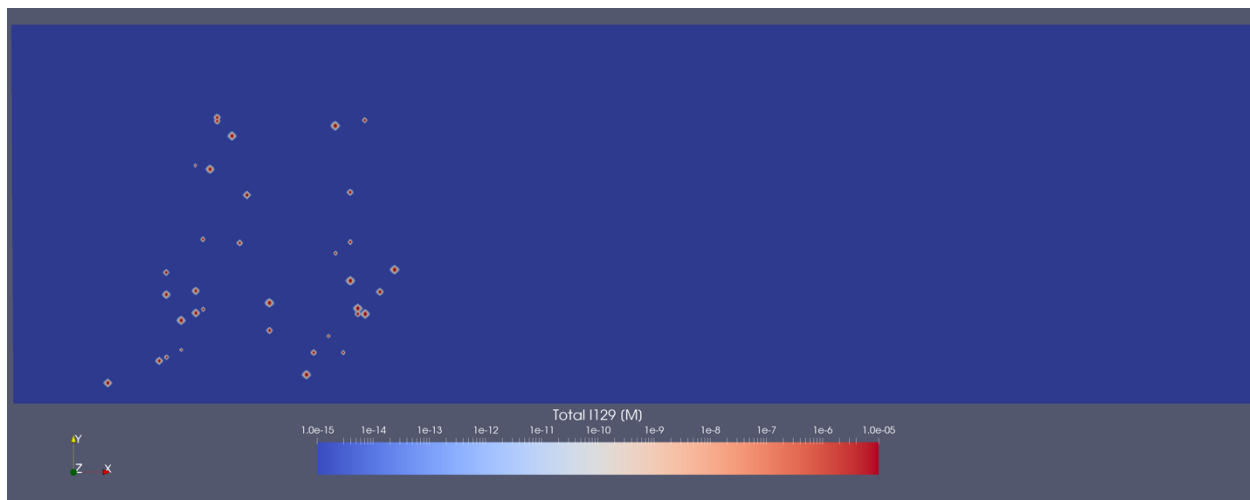


Figure 5-36. ^{129}I concentration at 1000 yr in the GENERAL mode simulation plotted in a horizontal slice through the model domain at the elevation of the repository.

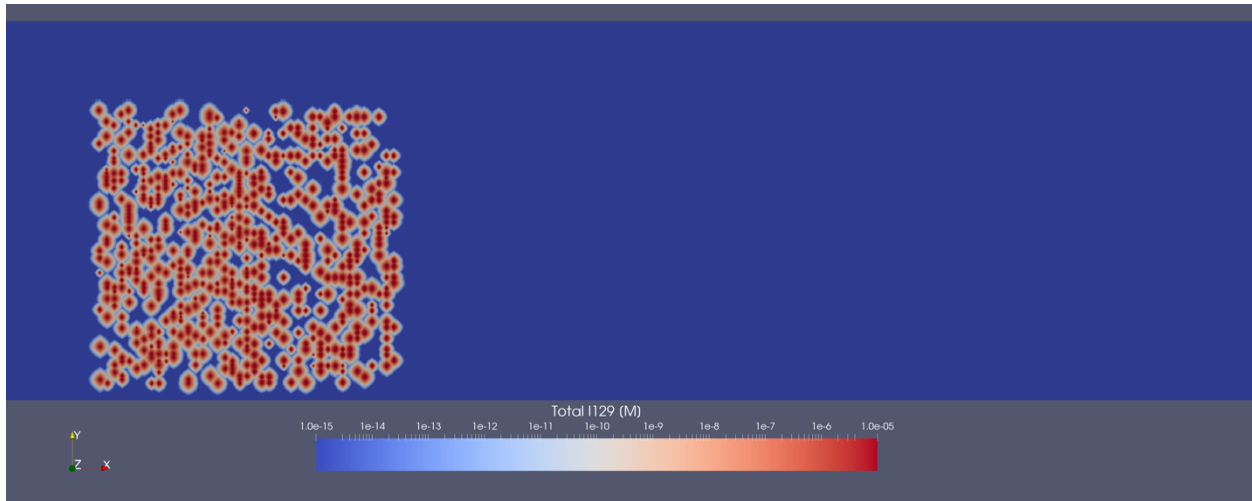


Figure 5-37. ^{129}I concentration at 10,000 yr in the GENERAL mode simulation plotted in a horizontal slice through the model domain at the elevation of the repository.

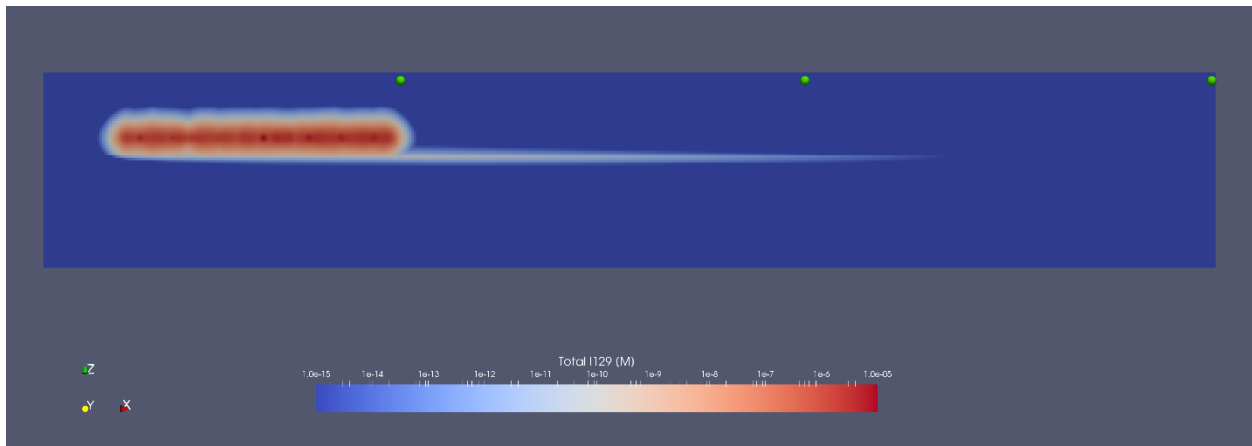


Figure 5-38. ^{129}I concentration at 100,000 yr in the GENERAL mode simulation plotted in a vertical slice through the model domain at the Y-midpoint of the repository.

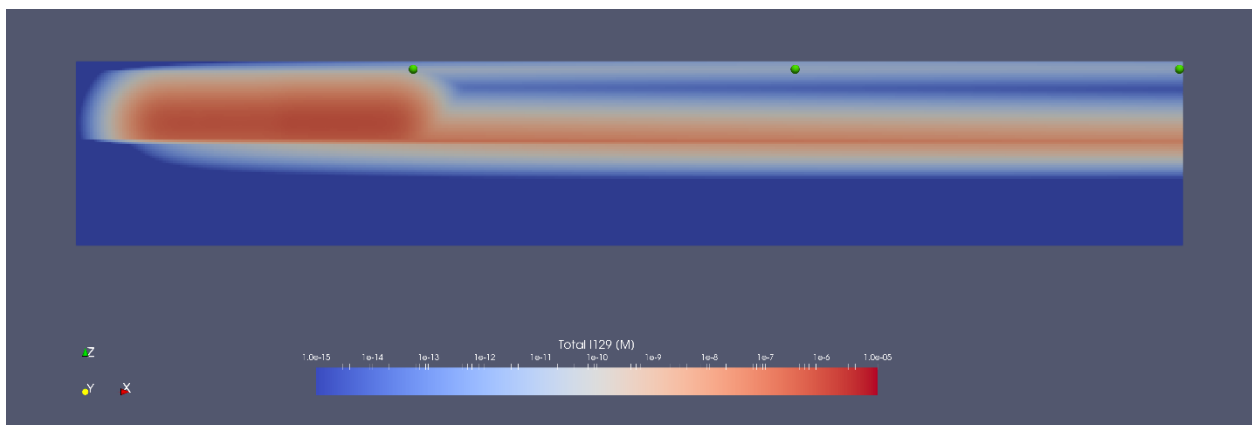


Figure 5-39. ^{129}I concentration at 1,000,000 yr in the GENERAL mode simulation plotted in a vertical slice through the model domain at the Y-midpoint of the repository.

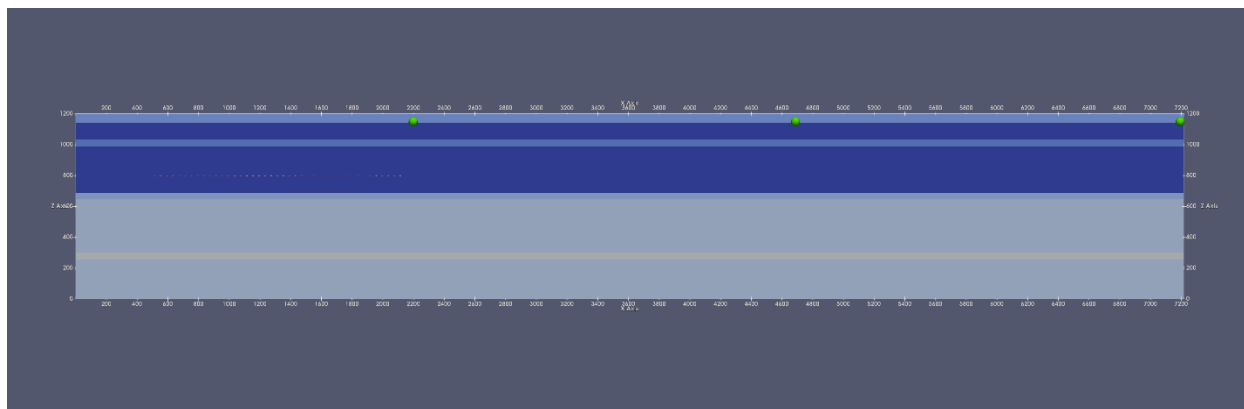


Figure 5-40. Locations of upper sandstone aquifer observation points.

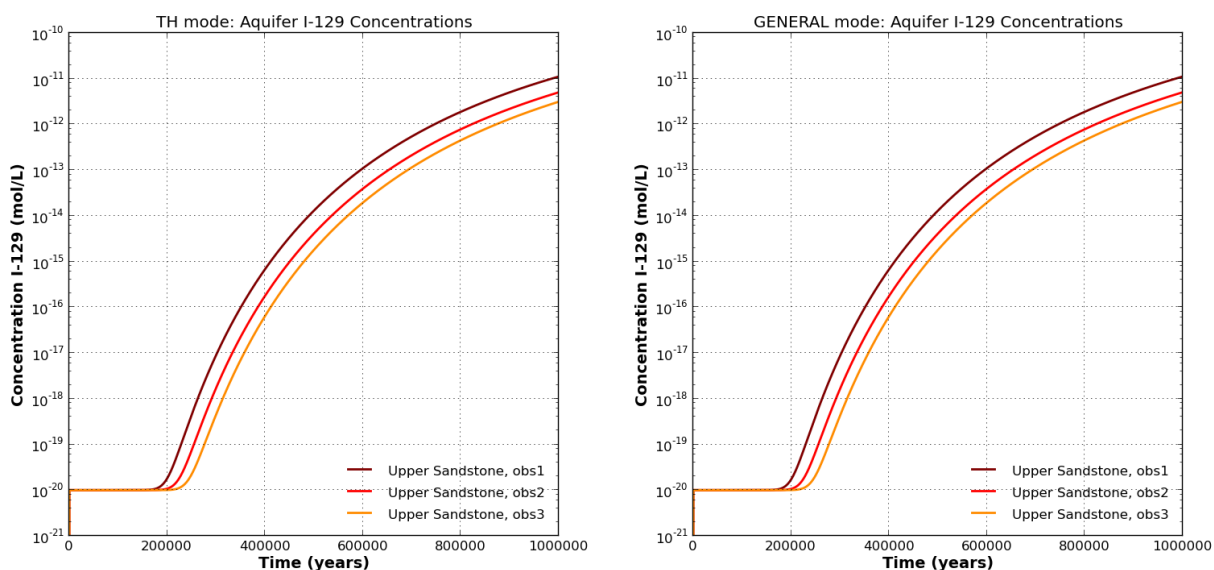


Figure 5-41. ^{129}I concentration versus time at each of the three upper sandstone aquifer observation points in TH mode (left) and GENERAL mode (right) simulations.

5.3.3.8.4 ^{36}Cl Transport

^{36}Cl , which like ^{129}I neither adsorbs nor precipitates, is present in the upper sandstone aquifer at concentrations greater than 10^{-15} M by 1,000,000 y (Figure 5-42). The plume of ^{36}Cl has much lower concentrations than that of ^{129}I because the ^{36}Cl release rate is much lower than that of ^{129}I . The lower release rate is due to a much lower inventory and a faster rate of decay (Tables 5-6 and 5-7), as well as a lower instant release fraction (Table 5-11).

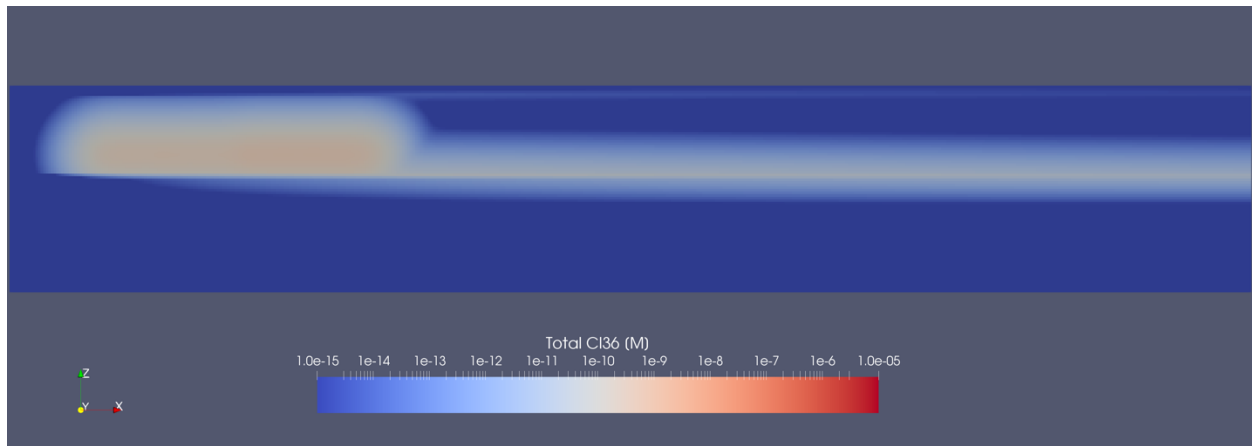


Figure 5-42. ³⁶Cl concentration at 1,000,000 yr in the GENERAL mode simulation plotted in a vertical slice through the model domain at the Y-midpoint of the repository.

5.3.3.8.5 ²³⁷Np Transport

²³⁷Np (and other radionuclide species that adsorb and/or precipitate) remain within the vicinity of the repository throughout the 1,000,000-yr simulation (Figure 5-43).

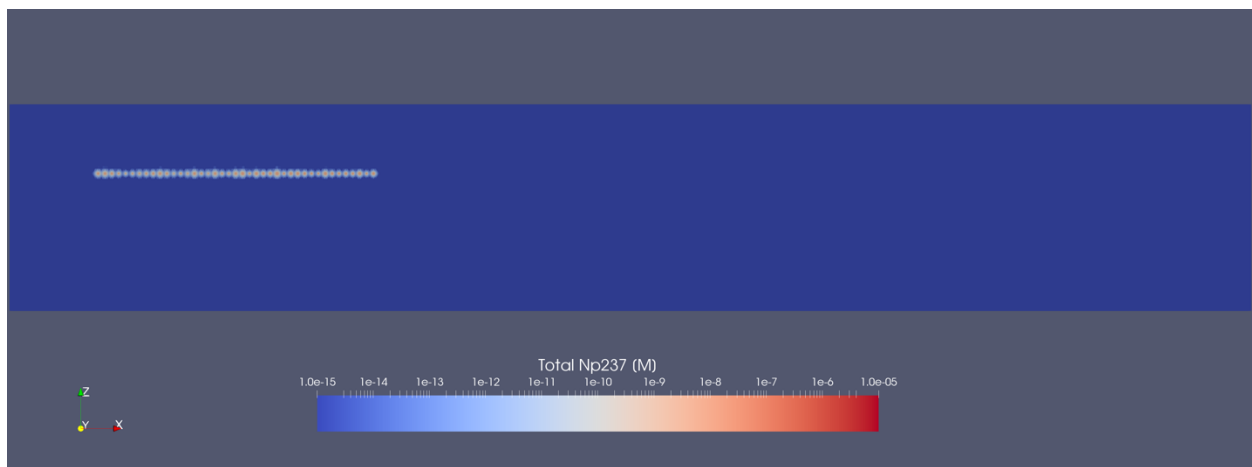


Figure 5-43. ²³⁷Np concentration at 1,000,000 yr in the GENERAL mode simulation plotted in a vertical slice through the model domain at the Y-midpoint of the repository.

6 SUMMARY AND CONCLUSIONS

This report describes specific activities in the second half of FY2019 associated with the Geologic Disposal Safety Assessment (GDSA) Repository Systems Analysis (RSA) work package within the SFWST Campaign. The overall objective of the GDSA RSA work package is to develop generic deep geologic repository concepts and system performance assessment (PA) models in several host-rock environments, and to simulate and analyze these generic repository concepts and models using the *GDSA Framework* toolkit (Mariner et al. 2019), and other tools as needed. The specific objectives in FY2019 are to

- Develop and/or augment generic repository reference cases for liquid-saturated host rock environments, particularly in argillaceous (e.g., typical shale or clay) host rocks; and a host rock environment in the unsaturated zone (UZ), such as alluvial valley fill.
- Ensure that reference cases include repository concepts and layouts for the disposal of DPC-canisterized pressurized water reactor (PWR) assemblies, including 37-PWR and 24-PWR waste packages.
- Perform PA simulations (deterministic and probabilistic) with *GDSA Framework* for the foregoing reference case concepts and models. Analyze and plot the PA simulation results, including uncertainty and sensitivity analyses.

This report describes specific GDSA RSA accomplishments in the second half of FY2019 and builds upon the work reported in M2SF-19SN010304051, *GDSA Repository Systems Analysis Progress Report* (Sevougian et al. 2019b).

Improvements to the numerical solvers in PFLOTRAN, needed for modeling the high heat output from dual purpose canister (DPC) waste packages, particularly during two-phase flow, such as might occur in an unsaturated host-rock environment, are discussed here. Multiphase (liquid and gas) flow and transport capabilities in PFLOTRAN (under the “GENERAL” flow mode) have been augmented to more efficiently simulate physically complex processes that could occur in unsaturated repositories and/or under conditions of extreme waste package heat production (as could be the case with a 37 PWR configuration). The most significant of these improvements involved refactoring of convergence criteria used during each iteration of the Newton-Raphson nonlinear solution search algorithm. Many of these improvements are reported in Sevougian et al. (2019b, Sec. 3.1) and in the recent work described by Mariner et al. (2019, Sec. 2.3.1.5).

Significant progress in interfacing the Sandia VoroCrust meshing software with PFLOTRAN is reported on. VoroCrust is a software tool that generates Voronoi meshes of arbitrary volumes (Abdelkader et al. 2018). PFLOTRAN simulations on Voronoi meshes will be more accurate than typical unstructured meshes because on a Voronoi mesh flux between cell centers is always perpendicular to cell faces, which means there is no mass balance error in the flux approximation. This project will develop the tools within VoroCrust for meshing to highly anisotropic geologic features and to export the resulting meshes in a format suitable for PFLOTRAN. In the past six months, substantial progress has been made. Meshes for five example problems have been created and validated for use in PFLOTRAN simulations.

Further progress on the technical basis and conceptual model for a reference case repository located in unsaturated alluvial sediments, which is an update of the unsaturated zone (UZ) alluvium reference case introduced in Mariner et al. (2018) and further developed in Sevougian et al. (2019b), is discussed here. The primary development of this reference case in FY2019 is related

to the inclusion of DPC waste packages and their representative higher heat output per package, which results in more severe coupled process effects at early times after repository closure. The initial task in simulating the alluvial reference case for the second half of FY2019 is to verify the suitability of the new Newton TR algorithm for simulations of this complex coupled TH model. In all five models benchmarked in this report the new solver gave the same results as the default Newton LS method. The TR method was also much faster. The study of multiple simulation models of one site-scale conceptual model has provided insight as to the level of grid refinement necessary to capture heat and fluid flow in the UZ repository for 24 PWRs 100-year out of the reactor (OoR).

This report also references FY2019 work detailed in Gross et al. (2019) that is intended to interface with the GDSA UZ alluvium reference case. In particular, Gross et al. (2019) describe the development of a new geologic framework model (GFM) for alluvial basins. A GFM must capture the geologic elements that impact the siting and dynamic behavior of a potential repository, including basin geometry, alluvium stratigraphy, lithofacies and geologic structures. The first step, and the focus of Gross et al. (2019), is to establish the geologic elements that define the boundaries of the alluvial sub-basin, such as depth to bedrock, basin-bounding and intra-basin faults, and the geometry of the bed rock on which the alluvial basin-fill sediments were deposited. Eventually, the generic basin-scale GFM (whether in alluvium or some other host rock) will interface with the GDSA repository-scale generic reference case.

An important update to the generic shale reference case (Mariner et al. 2017) is also described. First is an update to the Geologic Framework Model (GFM) for a representative shale environment that describes the geologic and hydrogeologic features represented in the GFM. The methodology used to develop the shale GFM is documented in detail in Sevougian et al. (2019b). In this current deliverable, updates to the features of the shale GFM first shown in Sevougian et al. (2019b) are presented and analytical methods are used to document the relationships between features represented in the GFM. Also updated are features and processes specific to the region of the shale GFM. The shale GFM was developed using RockWorks17® software (Rockware Inc., www.rockware.com) and ArcGIS 10.6 (ESRI, www.esri.com). A series of analyses are conducted using the GIS and GFM software to document the relationships between the reference repository horizon, the host formation, and hydrologic features represented in the GFM. One of the goals in developing the shale GFM is to demonstrate a workflow that uses the features of the GFM to create a mesh for simulation modeling. This is accomplished by exporting the geologic surfaces (formation tops) for input into the meshing software. Generating a simulation mesh from the geologic surfaces generated by Rockworks required a multistep process using python, CUBIT and SCULPT software.

Near-field simulations with a highly discretized grid in the shale reference case, first discussed in Sevougian et al. (2019b), are also presented. The objective of this study is to investigate the near-field thermal-hydrologic-mechanical (THM) behavior in a typical bentonite back-filled shale repository with the goal of representing its effect more accurately and mechanistically in a coarse-scale total system performance assessment model. To model such complex coupled phenomena, such as bentonite swelling and DRZ fracture movement, a combination of empirical and theoretical relationships from full process-model THM simulations are represented as functions of PFLOTRAN TH state variables. Eventually, a surrogate model will be coupled to PFLOTRAN to represent the effect of mechanical stresses on near-field porosity and permeability.

Finally, the site-scale shale-host-rock reference case that models the potential performance of a geologic repository based on direct disposal of DPC waste packages, is simulated and discussed in detail. This represents the FY2019 update to the GDSA Shale Reference Case first described in Section 4 of Mariner et. al (2017). The primary new tasks undertaken in FY2019 for the shale reference case simulations and associated *GDSA Framework* model were

- (1) Inclusion of 24-PWR and 37-PWR DPC waste packages in the reference case simulations.
- (2) An update to the stratigraphic model for a representative shale domain (Perry et al. 2014; Perry and Kelley 2017)—see description of Section 5.1 above.
- (3) An update to the numerical model grids and formation properties to incorporate changes to stratigraphy and repository design needed for DPC waste packages.

Future work in FY2020 will continue to focus on developing the technical bases for representing generic repository concepts in *GDSA Framework* simulations for deep geologic disposal in any of four possible host-rock environments: argillite, crystalline, bedded salt, and unsaturated zone formations. *GDSA Framework* simulations and associated sensitivity analyses for these generic reference case concepts will be conducted, including potential disposal of high-decay-heat waste packages such as those that might contain as-loaded DPCs. R&D will be performed on the appropriateness of nested grids, reduced-order or surrogate models, or coupled models of different geometric scale, with a goal towards optimizing simulation times and simulation results for both the near-field environment and the total system.

7 REFERENCES

- Abdelkader, A., Bajaj, C.L., Ebeida, M.S., Mahmoud, A.H., Mitchell, S.A., Rushdi, A.A., & Owens, J.D. 2018. Sampling Conditions for Conforming Voronoi Meshing by the VoroCrust Algorithm. *LIPICs : Leibniz international proceedings in informatics*, 99, 10.4230/LIPICs.SoCG.2018.1. doi:10.4230/LIPICs.SoCG.2018.1
- Bertog, J, 2010. Stratigraphy of the Lower Pierre Shale (Campanian): Implications for the Tectonic and Eustatic Controls of Facies Distributions. *Journal of Geologic Research*, 2010, 1-15.
- Blacker, T., S.J. Owen, M.L. Staten, R.W. Quador, B. Hanks, B. Clark, R.J. Meyers, C. Ernst, K. Merkley, R. Morris, C. McBride, C. Stimpson, M. Plooster, and S. Showman, 2016. *CUBIT Geometry and Mesh Generation Toolkit 15.2 User Documentation*, SAND2016-1649R, Sandia National Laboratories, Albuquerque, New Mexico.
- Blackwell, D.D., M.C. Richards, Z.S. Frone, J.F. Batir, M.A. Williams, A.A. Ruzo, and R.K. Dingwall, 2011. "SMU Geothermal Laboratory Heat Flow Map of the Conterminous United States, 2011," Supported by Google.org. Available at <http://www.smu.edu/geothermal> Retrieved October 25, 2016.
- Bourg, I.C., 2015. "Sealing Shales versus Brittle Shales: A Sharp Threshold in the Material Properties and Energy Technology Uses of Fine-Grained Sedimentary Rocks." *Environmental Science & Technology Letters*, 2(10), 255-259. doi: 10.1021/acs.estlett.5b00233
- Bredehoeft, J.D., C.E. Neuzil, and P.C.D. Milly, 1983. *Regional Flow in the Dakota Aquifer: A Study of the Role of Confining Layers*. Water-Supply Paper 2237. United States Geologic Survey, Alexandria, Virginia.
- Carter, J.T., A.J. Luptak, J. Gastelum, C. Stockman, and A. Miller, 2013. *Fuel Cycle Potential Waste Inventory for Disposition*. FCRD-USED-2010-000031 Rev 6. Savannah River National Laboratory, Aiken, South Carolina.
- Choi, H. J. and J. Choi (2008). "Double-layered buffer to enhance the thermal performance in a high-level radioactive waste disposal system," *Nuclear Engineering and Design*, **238**(10):2815-2820.
- Clayton, D., G. Freeze, T. Hadgu, E. Hardin, J. Lee, J. Prouty, R. Rogers, W.M. Nutt, J. Birkholzer, H.H. Liu, L. Zheng, and S. Chu 2011. *Generic Disposal System Modeling – Fiscal Year 2011 Progress Report*. FCRD-USED-2011-000184, SAND2011-5828P. U.S. Department of Energy, Office of Nuclear Energy, Used Fuel Disposition Campaign, Washington, DC.
- Conn, A. R., N. I. M. Gould, and P. L. Toint 2000. *Trust-Region Methods*, MOS-SIAM Ser. Optim. 1, SIAM, Philadelphia 2000.
- Croff, A.G. 1983. "ORIGEN2: A Versatile Computer Code for Calculating the Nuclide Compositions and Characteristics of Nuclear Materials," *Nuclear Technology*, 62(3), 335-352. doi: dx.doi.org/10.13182/NT83-1.
- DOE (U.S. Department of Energy) 2007. *Fall 2006 Assessment of Matheson Wetlands Hydrogeology and Ground Water Chemistry*, DOE-EM/GJ1441-2007, DOE Office of Environmental Management, Grand Junction, CO, March 2007, Doc. No. X0200300.
- DOE (U.S. Department of Energy) 2010. *Program and Project Management for the Acquisition of Capital Assets*, DOE O 413.3B, 11-29-2010, U.S. Department of Energy, Washington, D.C. 20585, available at <https://www.directives.doe.gov/directives-documents/400-series/0413.3-BOrder-b>
- DOE (U.S. Department of Energy) 2012. *Used Fuel Disposition Campaign Disposal Research and Development Roadmap*. FCR&D-USED-2011-000065, REV 1, U.S. DOE Office of Nuclear Energy, Used Fuel Disposition, Washington, D.C., September 2012.

- Downey, J.S. and G.A. Dinwiddie, 1988. *The Regional Aquifer System Underlying the Northern Great Plains in Parts of Montana, North Dakota, South Dakota, and Wyoming - Summary*. Professional Paper 1402-A. United States Geologic Survey, Washington, DC.
- Driscoll, D.G., Carter, J.M., Williamson, J.E., and Putnam, L.D., 2002. Hydrology of the Black Hills area, South Dakota: U.S. Geologic Survey Water-Resources Investigations Report 02-4094, 150 p.
- Fahrenbach, M.D., Steece, F.V., Sawyer, J.F., McCormick, K.A., McGillivray, G.L., Schulz, L.D., and Redden, J.A., 2007, South Dakota Stratigraphic Correlation Chart: Oil and Gas Investigation 3, South Dakota Geologic Survey.
- Forster, A. and D. Merriam, 1997. "Heat Flow in the Cretaceous of Northwestern Kansas and Implications for Regional Hydrology." *Current Research in Earth Sciences*, 1997(Bulletin 240, part 1.).
- Freeze, G., P. Gardner, P. Vaughn, S.D. Sevougian, P. Mariner, V. Mousseau and G. Hammond, 2013a. *Enhancements to Generic Disposal System Modeling Capabilities*. FCRD-UFD-2014-000062. SAND2013-10532P. Sandia National Laboratories, Albuquerque, New Mexico.
- Freeze, G., M. Voegelé, P. Vaughn, J. Prouty, W.M. Nutt, E. Hardin and S.D. Sevougian, 2013b. *Generic Deep Geologic Disposal Safety Case*. FCRD-UFD-2012-000146 Rev. 1, SAND2013-0974P, August 2013, Sandia National Laboratories, Albuquerque, New Mexico.
- Gonzales, S. and K.S. Johnson, 1985. Shales and Other Argillaceous Strata in the United States. ORNL/Sub/84-64794/1. Oak Ridge National Laboratory, Oak Ridge, Tennessee.
- Greene, E.A., 1993. Hydraulic Properties of the Madison Aquifer System in the Western Rapid City Area, South Dakota. *U.S. Geologic Survey Water-Resources Investigations Report 93-4008*, 65 p.
- Greene, S.R., Medford, J.S. and S.A. Macy, 2013. Storage and Transport Cask Data for Used Commercial Nuclear Fuel – 2013 U.S. Edition. ATI-TR-13047. Knoxville, Tennessee: Advanced Technology Insights, LLC; Oak Ridge, Tennessee: EnergX.
- Gross, M., G. Bussod, C.W. Gable, R. Kelley, A. Lavadie-Bulnes, D. Milazzo, E. Miller, T.A. Miller, R. Roback, P.H. Stauffer, E. Swanson, and F. Perry 2019. *Progress Report on the Development of a Geologic Framework Model Capability to Support GDSA*, LA-UR-19-27943, Los Alamos National Laboratory, Los Alamos, NM, August 8, 2019.
- Hammond, G.E., Lichtner, P.C. and R.T. Mills 2014. "Evaluating the performance of parallel subsurface simulators: An illustrative example with PFLOTRAN." *Water Resources Research*, 50(1), 208-228. doi: 10.1002/2012wr013483
- Hansen, F.D., Hardin, E.L., Rechard, R.P., Freeze, G.A., Sassani, D.C., Brady, P.V. Stone, C.M., Martinez, M.J., Holland, J.F., Dewers, T., Gaither, K.N., Sobolik, S.R. and R. T. Cygan 2010. *Shale Disposal of U.S. High-Level Radioactive Waste*, SAND2010-2843. Sandia National Laboratories, Albuquerque, New Mexico.
- Hardin, E. and E. Kalinina 2016. Cost Estimation Inputs for Spent Nuclear Fuel Geologic Disposal Concepts. SAND2016-0235. Sandia National Laboratories, Albuquerque, New Mexico.
- Hardin, E., Clayton, D., Howard, R., Scaglione, J.M., Pierce, E., Banerjee, K., Voegelé, M.D., Greenberg, H., Wen, J., Buscheck, T.A., Carter, J.T., Severynse, T., and W.M. Nutt 2013. Preliminary Report on Dual-Purpose Canister Disposal Alternatives (FY13), August 2013, FCRD-UFD-2013-000171 Rev. 0.
- IAEA (International Atomic Energy Agency) 2012. *The Safety Case and Safety Assessment for the Disposal of Radioactive Waste*, Specific Safety Guide, IAEA Safety Standards Series No. SSG-23, International Atomic Energy Agency, Vienna, 2012.
- Jackson, J. A. (1997). *Glossary of Geology*. Alexandria, VA, American Geologic Institute.

- Jobmann, M. and G. Buntebarth 2009. "Influence of graphite and quartz addition on the thermo-physical properties of bentonite for sealing heat-generating radioactive waste." *Applied Clay Science*, 44(3-4), 206-210. doi: 10.1016/j.clay.2009.01.016
- Johnson, L., Ferry, C., Poinssot, C. and P. Lovera 2005. "Spent Fuel Radionuclide Source-Term Model for Assessing Spent Fuel Performance in Geologic Disposal. Part 1: Assessment of the Instant Release Fraction," *Journal of Nuclear Materials*, 346, pp. 56-65
- Jove-Colon, C. F., P. F. Weck, D. C. Sassani, L. Zheng, J. Rutqvist, C. I. Steefel, K. Kim, S. Nakagawa, J. Houseworth, J. Birkholzer, F. A. Caporuscio, M. Cheshire, M. S. Rearick, M. K. McCarney, M. Zavarin, A. Benedicto-Cordoba, A. B. Kersting, M. Sutton, J. L. Jerden, K. E. Frey, J. M. Copple and W. L. Ebert 2014. *Evaluation of Used Fuel Disposition in Clay-Bearing Rock*, FCRD-UFD-2014-000056, SAND2014-18303 R. Sandia National Laboratories, Albuquerque, New Mexico.
- Korn, A.S. and Pagnac, D.C., 2017. Anatomically Linked Occurrence of Concretionary Preservation of Mosasaurs from the Pierre Shale of South Dakota. *Palaios*, 32, 330-336.
- Li, Y.H. and S. Gregory 1974. "Diffusion of ions in sea-water and in deep-sea sediments," *Geochimica et Cosmochimica Acta*, **38**(5):703-714.
- Liu, J. F., Y. Song, F. Skoczylas and J. Liu (2016). "Gas migration through water-saturated bentonite-sand mixtures, CO_x argillite, and their interfaces," *Canadian Geotechnical Journal*, **53**(1):60-71.
- Lobmeyer, D., 1985. Freshwater Heads and Ground-Water Temperatures in Aquifers of the Northern Great Plains in parts of Montana, North Dakota, South Dakota, and Wyoming. U.S. Geologic Survey Professional Paper 1402-D. 18 p.
- Mariner, P.E., Gardner, W.P., Hammond, G.E., Sevougian, S.D. and E.R. Stein 2015. *Application of Generic Disposal System Models*. SAND2015-10037R; FCRD-UFD-2015-000126. Sandia National Laboratories, Albuquerque, New Mexico.
- Mariner, P.E., Stein, E.R., Frederick, J.M., S. D. Sevougian, G. E. Hammond, and D. G. Fascitelli 2016. *Advances in Geologic Disposal System Modeling and Application to Crystalline Rock*, FCRD-UFD-2016-000440, SAND2016-96107R. Sandia National Laboratories, Albuquerque, NM, September 22, 2016.
- Mariner, P. E., E. R. Stein, Frederick, J.M., Sevougian, S.D. and G. E. Hammond 2017. *Advances in Geologic Disposal System Modeling and Shale Reference Cases*, SFWD-SFWST-2017-000044 SAND2017-10304 R, Sandia National Laboratories, Albuquerque, New Mexico.
- Mariner, P.E., Stein, E.R., Sevougian, S.D., Cunningham, L.J., Frederick, J.M., Hammond, G.E., Lowry, T.S., Jordan, S. and E. Basurto 2018. *Advances in Geologic Disposal Safety Assessment and an Unsaturated Alluvium Reference Case*, SFWD-SFWST-2018-000509, SAND2018-11858R, 130 p.
- Mariner, P. E., Connolly, L.A., Cunningham, L.J., Debusschere, B.J., Dobson, D.C., Frederick, J.M., Hammond, G.E., Jordan, S.H., LaForce, T.C., Nole, M.A., Park, H.D., Perry, F.V., Rogers, R.D., Seidl, D.T., Sevougian, S.D., Stein, E.R., Swift, P.N., Swiler, L.P., Vo. J., and M.G. Wallace 2019. *Progress in Deep Geologic Safety Assessment in the U.S. since 2010*, M2SF-19SN010304041, U.S. Department of Energy, Spent Fuel and Waste Science and Technology Campaign, Office of Spent Fuel and Waste Disposition, Washington, DC, September 16, 2019.
- Martin, J.E., Sawyer, J.F., Fahrenbach, M.D., Tomhave, D.W. and L.D. Schulz 2004, Geologic Map of South Dakota: South Dakota Geologic Survey. GIS data downloaded from <https://mrdata.usgs.gov/geology/state/state.php?state=SD>
- Martin, J.E., Bertog, J.L., and Parris, D.C., 2007. Revised lithostratigraphy of the lower Pierre Shale Group (Campanian) of central South Dakota, including newly designated members. *The Geologic Society of America Special Paper*, 427, 9-21.

- Matteo et al. 2019. *Evaluation of Engineered Barrier System Mid-Year Status Report*, M2SF-19SN010308042, U.S. Department of Energy, Spent Fuel and Waste Science and Technology Campaign, Office of Spent Fuel and Waste Disposition, Washington, DC, June 30, 2019.
- McCormick, K.A. 2010. Elevation Contour Map of the Precambrian Surface of South Dakota. South Dakota Geologic Survey. Available online at <http://www.sdgs.usd.edu/publications/index.html>.
- Millington, R. J. (1959). "Gas Diffusion in Porous Media," *Science*, **130**(3367):100-102.
- Mitchell, J. K., & Soga, K. (2005). *Fundamentals of soil behavior* (Vol. 3). Hoboken, NJ: John Wiley & Sons.
- Neuzil, C.E. 1993. Low fluid pressure within the Pierre Shale: A transient response to erosion, *Water Resources Research*, 29 (7), 2007–2020.
- Neuzil, C. E., 2015. Interpreting fluid pressure anomalies in shallow intraplate argillaceous formations, *Geophysical Research Letters*, 42, 4801–4808.
- Nichols, T.C., Donley, S.C., Jones-Cecil, M., and Swolfs, H.S., 1994. Faults and structure in the Pierre Shale, central South Dakota. Geologic Society of America Special Paper 287, 211-235.
- Ollila, K. (2008). Dissolution of unirradiated UO₂ and UO₂ doped with ²³³U in low- and high-ionic strength NaCl under anoxic and reducing conditions. Working Report 2008-50. Posiva Oy, Eurajoki, Finland.
- Owen, SJ, Ernst, CD, and Stimpson, CJ 2019a. "Sculpt Version 15.4: Automatic Parallel Hexahedral Mesh Generation", SAND2019-6412, Sandia National Laboratories, Albuquerque, New Mexico.
- Owen, SJ, Ernst, CD, Brown, JA, Lim, H, Long, KN, Foulk III JW, Moore NW, Battaile, C, and Rodgers, T 2019b. "Mesh generation for Microstructures", SAND2019-8967, Sandia National Laboratories, Albuquerque, New Mexico.
- Perry, F.V., R.E. Kelley, P.F. Dobson and J.E. Houseworth 2014. *Regional Geology: A GIS Database for Alternative Host Rocks and Potential Siting Guidelines*. LA-UR-14-20368, FCRD-UFD-2014-000068. Los Alamos National Laboratory, Los Alamos, New Mexico.
- Perry, F.V. and R.E. Kelley 2017. *Regional Geologic Evaluations for Disposal of HLW and SNF: The Pierre Shale of the Northern Great Plains*. SFWD-SFWST-2017-000119. U.S. Department of Energy, Spent Fuel and Waste Technology. Los Alamos Unlimited Release LA-UR-17-27829. 31 p.
- Price, L.L., Alsaed, A.A., Brady, P.V., Gross, M.B., Hardin, E.L., Nole, M., Prouty, J.L., Banerjee, K., and G.G. Davidson 2019, *Postclosure Criticality Consequence Analysis – Scoping Phase*, M3SF-19SN010305061, U.S. Department of Energy, Office of Spent Fuel and Waste Disposition, Washington, DC, January 22, 2019.
- Rechard, R. P., B. Goldstein, L.H. Brush, J.A. Blink, M. Sutton, and F.V. Perry (2011). Basis for Identification of Disposal Option for Research and Development for Spent Nuclear Fuel and High-Level Waste. FCRD-USED-2011-000071. SAND2011-3781P, Sandia National Laboratories, Albuquerque, New Mexico.
- Rutqvist, J., Y. Ijiri, and H. Yamamoto (2011). "Implementation of the Barcelona Basic Model into TOUGH-FLAC for simulations of the geomechanical behavior of unsaturated soils," *Computers & Geosciences*, **37**(6): 751-762.
- Rutqvist, J., L. Zheng, F. Chen, H.-H. Liu, and J. Birkholzer (2014), Modeling of Coupled Thermo-Hydro-Mechanical Processes with Links to Geochemistry Associated with Bentonite-Backfilled Repository Tunnels in Clay Formations, *Rock Mechanics and Rock Engineering*, 47(1): 167-186.
- Sassani, D.C., Jové Colón, C.F., Weck, P., Jerden, J.L., Frey, K.E., Cruse, T., Ebert, W.L., Buck, E.C., Wittman, R.S., Skomurski, F.N., Cantrell, K.J., McNamara, B.K. and C.Z. Soderquist 2012. Integration of

EBS Models with Generic Disposal System Models (FCRD-UFD-2012-000277), U.S. Department of Energy: Washington DC.

Sassani, D.C., Jang, J.-H., Mariner, P., Price, L., Rechard, R.P., Rigali, M., Rogers, R., Stein, E.R., Walkow, W. and P.F. Weck 2016. *The On-line Waste Library (OWL): Usage and Inventory Status Report*. SAND2016-9485 R; FCRD-UFD-2016-000080. Sandia National Laboratories, Albuquerque, New Mexico.

Schultz, L.G., Tourtelot, H.A., Gill, J.R., and Boergnen, J.G., 1980. Composition and Properties of the Pierre Shale and Equivalent Rocks, Northern Great Planes Region. Geologic Survey Professional Paper, 1064-B, 114 p.

Sevougian, S. D. and R. J. MacKinnon 2017. "Technology Readiness Assessment Process Adapted to Geologic Disposal of HLW/SNF," in *Proceedings of the International High-Level Radioactive Waste Management (IHLRWM 2017) Conference*, April 9 – 13, 2017, Charlotte, NC, SAND2017-0179C.

Sevougian, S.D., Freeze, G.A., Gross, M.B., Lee, J., Leigh, C.D., Mariner, P., MacKinnon, R.J. and P. Vaughn 2012. *TSPA Model Development and Sensitivity Analysis of Processes Affecting Performance of a Salt Repository for Disposal of Heat-Generating Nuclear Waste*. FCRD-UFD-2012-000320 Rev. 0, U.S. Department of Energy, Office of Used Nuclear Fuel Disposition, Washington, DC.

Sevougian, S.D., Freeze, G.A., Vaughn, P., Mariner, P. and W.P. Gardner 2013. *Update to the Salt R&D Reference Case*. FCRD-UFD-2013-000368, SAND2013-8255P. Sandia National Laboratories, Albuquerque, New Mexico.

Sevougian, S.D., Freeze, G.A., Gardner, W.P., Hammond, G.E. and P. Mariner 2014. *Performance Assessment Modeling and Sensitivity Analyses of Generic Disposal System Concepts*. FCRD-UFD-2014-000320, SAND2014-17658. Sandia National Laboratories, Albuquerque, New Mexico, September 12, 2014.

Sevougian, S.D., Stein, E.R., Gross, M.B., Hammond, G.E., Frederick, J.M. and P.E. Mariner 2016. *Status of Progress Made Toward Safety Analysis and Technical Site Evaluations for DOE Managed HLW and SNF*, SAND2016-11232R; FCRD-UFD-2016-000082, Rev. 1. Sandia National Laboratories, Albuquerque, New Mexico.

Sevougian, S. D., G. E. Hammond, P. E. Mariner, E. R. Stein, J. M. Frederick, and R. J. MacKinnon 2018. "GDSA Framework: High-Performance Safety Assessment Software to Support the Safety Case." in *Proceedings of the IGSC Safety Case Symposium 2018*, Rotterdam, The Netherlands, October 10-11, 2018, SAND2018-9975C, Sandia National Laboratories. Albuquerque, NM.

Sevougian, S. D., Mariner, P. E., Connolly, L. A., MacKinnon, R. J., Rogers, R. D., Dobson, D. C. and J. L. Prouty 2019a. *DOE SFWST Campaign R&D Roadmap Update, Rev. 1*, SAND2019-9033R, Sandia National Laboratories, Albuquerque, New Mexico, July 22, 2019.

Sevougian, S. D., E. R. Stein, T. LaForce, F. V. Perry, T. S. Lowry, L. J. Cunningham, M. Nole, C. B. Haukwa, K. W. Chang and P. E. Mariner 2019b. *GDSA Repository Systems Analysis Progress Report*. SAND2019-5189R. Sandia National Laboratories, Albuquerque, New Mexico, April 30, 2019.

Shelton, S.M. 1934. "Thermal conductivity of some irons and steels over the temperature range 100 to 500 C," *Bureau of Standards Journal of Research*, 12(4/6), 441-450.

Shurr, G.W. 1977. The Pierre Shale, Northern Great Plains: A Potential Isolation Medium for Radioactive Waste. Open-File Report 77-776. *United States Geologic Survey*, Reston, Virginia.

SKB (2006). Data report for the safety assessment SR-Can. SKB TR-06-25. Svensk Kärnbränslehantering AB, Stockholm, Sweden.

Sosnowski, M., J. Kryzwanski, and R. Gnatowska 2017. "Polyhedral meshing as an innovative approach to computational domain discretization of a cyclone in a fluidized bed CLC unit," E3S Web of Conferences, **14**, 01027 (2017), *Energy and Fuels 2016*, DOI: 10.1051/e3sconf/20171401027.

van Loon, L.R. and J. Mibus 2015. "A modified version of Archie's law to estimate effective diffusion coefficients of radionuclides in argillaceous rocks and its application in safety analysis studies." *Applied Geochemistry*, **59**, 85-94. doi: 10.1016/j.apgeochem.2015.04.002

Vaughn, P., Sevougian, S.D., Hardin, E.L., Mariner, P. and M.B. Gross 2013. "Reference Case for Generic Disposal of HLW and SNF in Salt," in *Proceedings of the 2013 International High-Level Radioactive Waste Management Conference*, Albuquerque, NM, April 28 – May 2, 2013, American Nuclear Society, La Grange Park, Illinois. (www.ans.org)

Vis, G.-J. and J.M. Verweij, 2014. Geologic and geohydrological characterization of the Boom Clay and its overburden. OPERA-PU-TNO411. The Netherlands. 86 p. www.covra.nl

Wang, H.F. 2000. *Theory of Linear Poroelasticity with Applications to Geomechanics and Hydrogeology*, Princeton University Press.

Wang, Y., E. Matteo, J. Rutqvist, J. Davis, L. Zheng, J. Houseworth, J. Birkholzer, T. Dittrich, C. W. Gable, S. Karra, N. Makedonska, S. Chu, D. Harp, S. L. Painter, P. Reimus, F. V. Perry, P. Zhao, J. B. Begg, M. Zavarin, S. J. Tumey, Z. R. Dai, A. B. Kersting, J. Jerden, K. E. Frey, J. M. Copple and W. Ebert (2014). *Used Fuel Disposal in Crystalline Rocks: Status and FY14 Progress*, FCRD-UFD-2014-000060, SAND2014-17992R. Sandia National Laboratories, Albuquerque, New Mexico.

Wang, Y., T. Hadgu, E. Matteo, J. N. Kruichak, M. M. Mills, R. Tinnacher, J. Davis, H. S. Viswanathan, S. Chu, T. Dittrich, F. Hyman, S. Karra, N. Makedonska, P. Reimus, M. Zavarin, P. Zhao, C. Joseph, J. B. Begg, Z. Dai, A. B. Kersting, J. Jerden, J. M. Copple, T. Cruse and W. Ebert (2015). *Used Fuel Disposal in Crystalline Rocks: FY15 Progress Report*. FCRD-UFD-2015-000125. Sandia National Laboratories, Albuquerque, New Mexico.

Wang, Y. and J.H. Lee 2010. *Generic Disposal System Environment Modeling - Fiscal Year 2010 Progress Report*. SAND2010-8202P. Sandia National Laboratories, Albuquerque, New Mexico.

Weast, R. C. and M. J. Astle, Eds. (1981). *CRC Handbook of Chemistry and Physics*. Boca Raton, Florida, CRC Press, Inc.

Zyvoloski, G. A., B. A. Robinson, Z. V. Dash, S. Kelkar, H. S. Viswanathan, R. J. Pawar, P. H. Stauffer, T. A. Miller, and S. Chu 2012. *Software Users Manual (UM) for the FEHM Application Version 3.1 – 3.X*. Los Alamos National Laboratory, Los Alamos, NM.

Zoback, M.D. 2007. *Reservoir Geomechanics*, Cambridge University Press.